

The lead-up to the Sturtian Snowball Earth: Neoproterozoic chemostratigraphy time-calibrated by the Tambien Group of Ethiopia

Yuem Park¹, Nicholas L. Swanson-Hysell¹, Scott A. MacLennan², Adam C. Maloof², Mulubrhan Gebreslassie^{3,4}, Marissa M. Tremblay^{1,5}, Blair Schoene², Mulugeta Alene³, Eliel S. C. Anttila^{1,6}, Tadele Tesema³, Bereket Haileab⁷

¹ Department of Earth and Planetary Science, University of California, Berkeley, CA, USA

² Department of Geosciences, Princeton University, Princeton, NJ, USA

³ School of Earth Sciences, Addis Ababa University, Addis Ababa, Ethiopia

⁴ Current affiliation: Department of Applied Geology, Adama Science and Technology University, Adama, Ethiopia

⁵ Current affiliation: Scottish Universities Environmental Research Centre, East Kilbride, Scotland, UK

⁶ Current affiliation: Department of Earth and Planetary Science, Harvard University, Cambridge, MA, USA

⁷ Department of Geology, Carleton College, Northfield, MN, USA

This article is in preparation for submission to GSA Bulletin.

¹ ABSTRACT

² The Tonian-Cryogenian Tambien Group of northern Ethiopia is a mixed carbonate-siliciclastic
³ sequence that culminates in glacial deposits associated with the first of the Cryogenian glaciations
⁴ - the Sturtian ‘Snowball Earth.’ Tambien Group deposition occurred atop arc volcanics and
⁵ volcaniclastics of the Tsaliit Group. The presence of intercalated tuffs suitable for high-precision
⁶ U-Pb geochronology within the Tambien Group enable temporal constraints on stratigraphic data

7 sets of the interval leading into the Sturtian Glaciation. New U-Pb dates demonstrate that the
8 transition between the Tsaliet and Tambien groups occurred at ca. 820 Ma in western exposures
9 and ca. 795 Ma in eastern exposures, which is consistent with deposition in an evolving back-arc
10 basin. Recently discovered exposures of Sturtian glacial deposits and underlying Tambien Group
11 strata in the Samre Fold-Thrust Belt comprise the most complete carbonate stratigraphy leading
12 into the glaciation reported to date from anywhere in the world. New $\delta^{13}\text{C}$ and $^{87}\text{Sr}/^{86}\text{Sr}$ data
13 and U-Pb ID-TIMS ages from the Tambien Group are used in conjunction with previously
14 published isotopic and geochronologic data to construct time-calibrated composite Tonian carbon
15 and strontium isotope curves. Tambien Group $\delta^{13}\text{C}$ data and U-Pb ages reveal that the youngest
16 recognized pre-Sturtian sharp negative $\delta^{13}\text{C}$ excursion (the Islay Anomaly) precedes the Sturtian
17 Glaciation by \sim 18 Myr, is synchronous in at least two separate basins, and is followed by a
18 prolonged interval of positive $\delta^{13}\text{C}$ values. The composite Tonian $^{87}\text{Sr}/^{86}\text{Sr}$ curve shows that,
19 following an extended interval of low and relatively invariant values, inferred seawater $^{87}\text{Sr}/^{86}\text{Sr}$
20 rose ca. 880–770 Ma, and then decreased to the ca. 717 Ma initiation of the Sturtian Glaciation.
21 These data, when combined with a simple global weathering model and an analysis of
22 paleogeography and the timing and paleolatitude of large igneous province eruptions and arc
23 accretion events, suggest that the $^{87}\text{Sr}/^{86}\text{Sr}$ increase was influenced by increased subaerial
24 weathering of radiogenic lithologies as Rodinia rifted apart at low latitudes, and that the
25 following prolonged $^{87}\text{Sr}/^{86}\text{Sr}$ decrease is consistent with enhanced subaerial weathering of arcs
26 accreting in the tropics over tens of millions of years, lowering pCO₂ and contributing to the
27 initiation of the Sturtian Glaciation.

28 **Keywords:** Neoproterozoic; chemostratigraphy; carbon isotope; strontium isotope;
29 geochronology; Sturtian Snowball Earth

30 INTRODUCTION

31 Life and climate evolved dramatically during the Tonian period (1000-717 Ma). Sedimentary
32 rocks from this period record the diversification of eukaryotic life (e.g. Knoll et al., 2006;
33 Butterfield, 2015), large-scale fluctuations of the carbon cycle as recorded by $\delta^{13}\text{C}$ of shallow
34 marine carbonates (e.g. Halverson et al., 2005), and major changes to paleogeography (e.g. Li
35 et al., 2008, 2013) during the lead-up to severe Cryogenian glaciations. Understanding global
36 change leading up to these glaciations is critical for interpreting the boundary conditions that
37 allowed these extreme environmental conditions to occur, especially since no ice sheets are known
38 to have existed for \sim 1.5 Gyr between the ca. 2.2 Ga Makganyene Glaciation (Evans et al., 1997)
39 and the ca. 717 Ma start of the Cryogenian glaciations.

40 The Tonian-Cryogenian Tambien Group of the Tigray region of northern Ethiopia is a mixed
41 carbonate-siliciclastic sequence deposited in an arc-proximal basin that culminates in glacial
42 deposits associated with the first of the Cryogenian glaciations - the Sturtian ‘Snowball Earth’
43 (Beyth et al., 2003; Miller et al., 2003; Swanson-Hysell et al., 2015; MacLennan et al., 2018). The
44 presence of intercalated tuffs suitable for U-Pb geochronology leading into the glaciation makes
45 these sedimentary rocks a target for temporally constraining stratigraphic and isotopic data sets of
46 the interval preceding, and leading into, the Sturtian Glaciation. For example, large-scale carbon
47 isotopic change ca. 810-790 Ma (the Bitter Springs Stage) was inferred to be globally synchronous
48 on the basis of high precision U-Pb dates from western exposures of lower Tambien Group rocks
49 in Ethiopia (Swanson-Hysell et al., 2015) in conjunction with U-Pb dates from Fifteenmile Group
50 rocks in Canada (Macdonald et al., 2010). Swanson-Hysell et al. (2015) also developed a
51 lithostratigraphic framework for the Tambien Group that built on the prior work of Beyth (1972),
52 Hailu (1975), and Garland (1980), and proposed that upper Tambien Group formations only had
53 been documented in the core of the Negash Syncline at that time. However, a lack of
54 geochronology from these strata limited the potential to test this proposed framework and develop
55 time-calibrated stratigraphic records. Subsequent fieldwork led to the discovery of abundant,

56 previously unstudied exposures of upper Tambien Group stratigraphy, including Sturtian glacial
57 deposits of the Negash Formation, in the Samre Fold-Thrust Belt (Fig. 1). These exposures
58 provide the opportunity to produce lithostratigraphic, geochronologic, and chemostratigraphic
59 data from the interval immediately preceding the Sturtian Glaciation. Our initial work presented
60 geochronologic and $\delta^{13}\text{C}$ data from these Samre Fold-Thrust Belt exposures that provided
61 evidence for the global synchronicity of both a large-scale carbon isotopic excursion ca. 735 Ma
62 (the Islay Anomaly) and the initiation of the Sturtian Glaciation (MacLennan et al., 2018).

63 This study presents new lithostratigraphic and chemostratigraphic data, and additional U-Pb
64 dates, from the lower Tambien Group in the Mai Kenetal Syncline and the upper Tambien Group
65 in the Negash Syncline and the newly mapped Samre Fold-Thrust Belt. With these data, we
66 construct the most complete and temporally well-constrained pre-Sturtian chemostratigraphic
67 composite record to date, which we use to assess the nature of pre-glacial carbon isotope
68 anomalies and the evolution of global weathering fluxes leading into the Sturtian Glaciation.

69 GEOLOGICAL SETTING

70 The Arabian-Nubian Shield is a large region of Neoproterozoic juvenile crust with an area of
71 $\sim 2.7 \times 10^6 \text{ km}^2$ that makes up the northern portion of the East African Orogen (Fig. 1; Johnson,
72 2014). Its construction began with arc and back-arc volcanism generating juvenile crust starting
73 at ca. $858 \pm 7 \text{ Ma}$ (U-Pb date on zircon from a gneiss of oceanic arc affinity; Küster et al., 2008)
74 and continuing through the Tonian into the Cryogenian until final terrane accretion in the
75 Ediacaran at ca. 620 Ma (closure of basin constrained by U-Pb dates on detrital zircons and felsic
76 magmatism intruding ophiolites; Cox et al., 2012; Johnson, 2014; Cox et al., 2018). The
77 paleogeographic setting in which arc volcanism began is poorly constrained, although it has been
78 proposed that the ocean basin in which this volcanism occurred (known as the Mozambique
79 Ocean) formed as the result of rifting between the Indian, Saharan, and Congo-Tanzanian cratons
80 (Johnson et al., 2011). However, it is well constrained that this juvenile crust amalgamated as

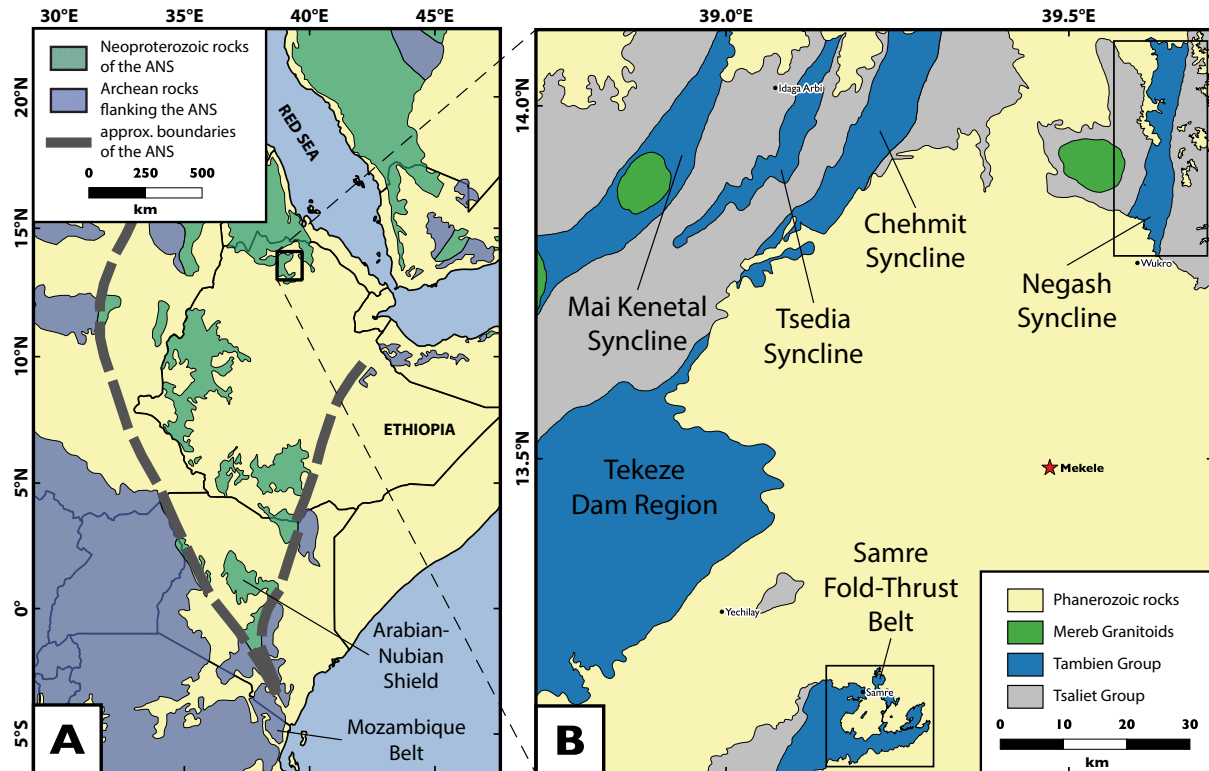


Figure 1. (A) Overview map of exposures of the Arabian-Nubian Shield (ANS) and adjacent Archean rocks (simplified from Johnson, 2014). (B) Overview map of Tambien Group exposures in northern Ethiopia. Inset boxes show the locations of detailed geological maps of the Negash Syncline and Samre Fold-Thrust Belt (Fig. 2), where glacigenic sedimentary rocks of the Negash Formation have been identified.

81 East Gondwana (Indian craton) and West Gondwana (Saharan and Congo-Tanzanian cratons)
 82 collided in the Ediacaran resulting in the East African Orogeny (Stern, 1994; Fritz et al., 2013).
 83 The East African Orogeny spanned over 6000 km from the Middle East to Madagascar (Collins
 84 and Windley, 2002; Johnson, 2014). In general, metamorphic grade in the Arabian-Nubian Shield
 85 increases from sub-greenschist and greenschist facies in the north to granulite facies in the south,
 86 where the Arabian-Nubian Shield transitions into higher grade metamorphic rocks of continental
 87 affinity known as the Mozambique Belt (Fig. 1; Johnson et al., 2011). This overall northward
 88 decrease in metamorphic grade allows for the preservation of primary sedimentary structures and

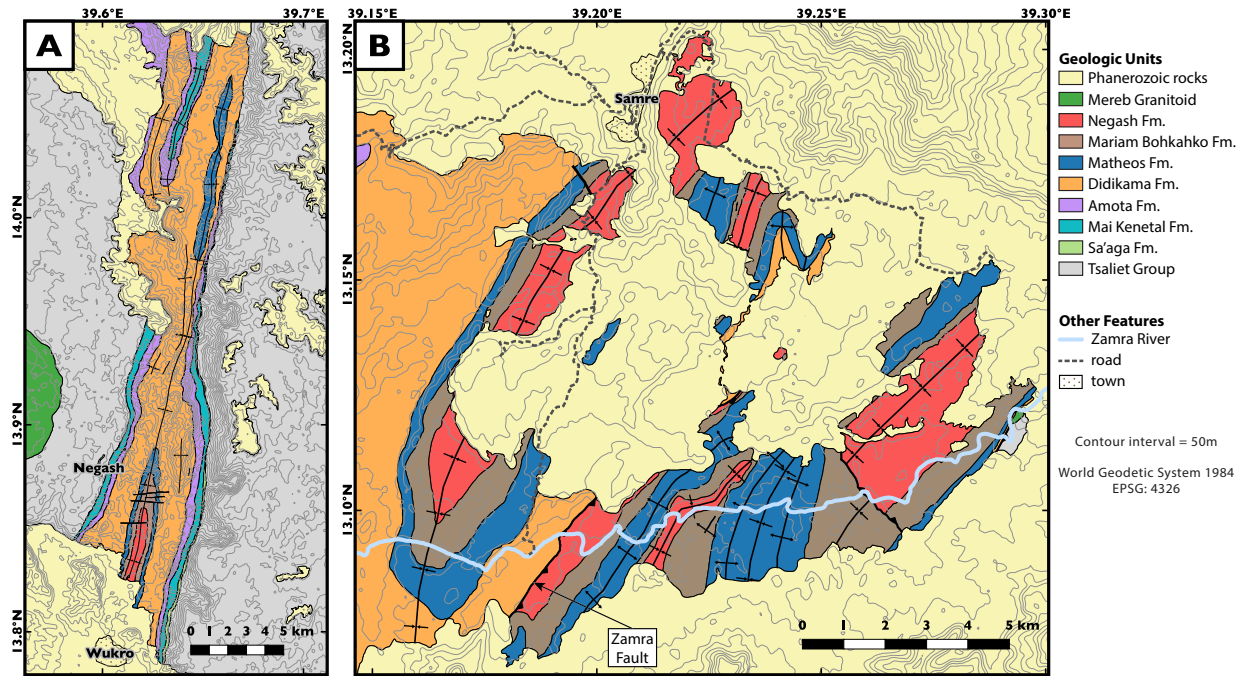


Figure 2. Geologic maps of the upper Tambien Group corresponding to inset boxes in Figure 1. (A) Negash Syncline geologic map synthesized from Beyth et al. (2003) and new mapping. (B) Samre Fold-Thrust Belt geologic map based on new mapping. There are notable differences in lithostratigraphy across the major NE-striking thrust fault, which we refer to as the Zamra Fault (see ‘Lithostratigraphy’).

geochemical signals in the Arabian-Nubian Shield. As a result, sedimentary rocks in this area are a viable target for reconstructing surface processes and environments at the time of deposition.

The Tambien Group (Fig. 1) is a Tonian-Cryogenian (ca. 820-700 Ma) sequence of carbonate and siliciclastic sedimentary rocks that culminates in a diamictite that has been interpreted to correlate with the ca. 717-660 Ma Sturtian Glaciation (Beyth et al., 2003; Alene et al., 2006; Miller et al., 2009; Swanson-Hysell et al., 2015; MacLennan et al., 2018). This sequence was deposited on top of the Tsaliel Group, which consists of volcanic and volcaniclastic lithologies correlated with 854±3 Ma Eritrean volcanics (Pb-Pb evaporation date; Teklay, 1997) that are associated with Arabian-Nubian Shield island arc volcanism. A maximum depositional age near the top of the Tsaliel Group (within 75 m of the Tsaliel-Tambien Group contact) of

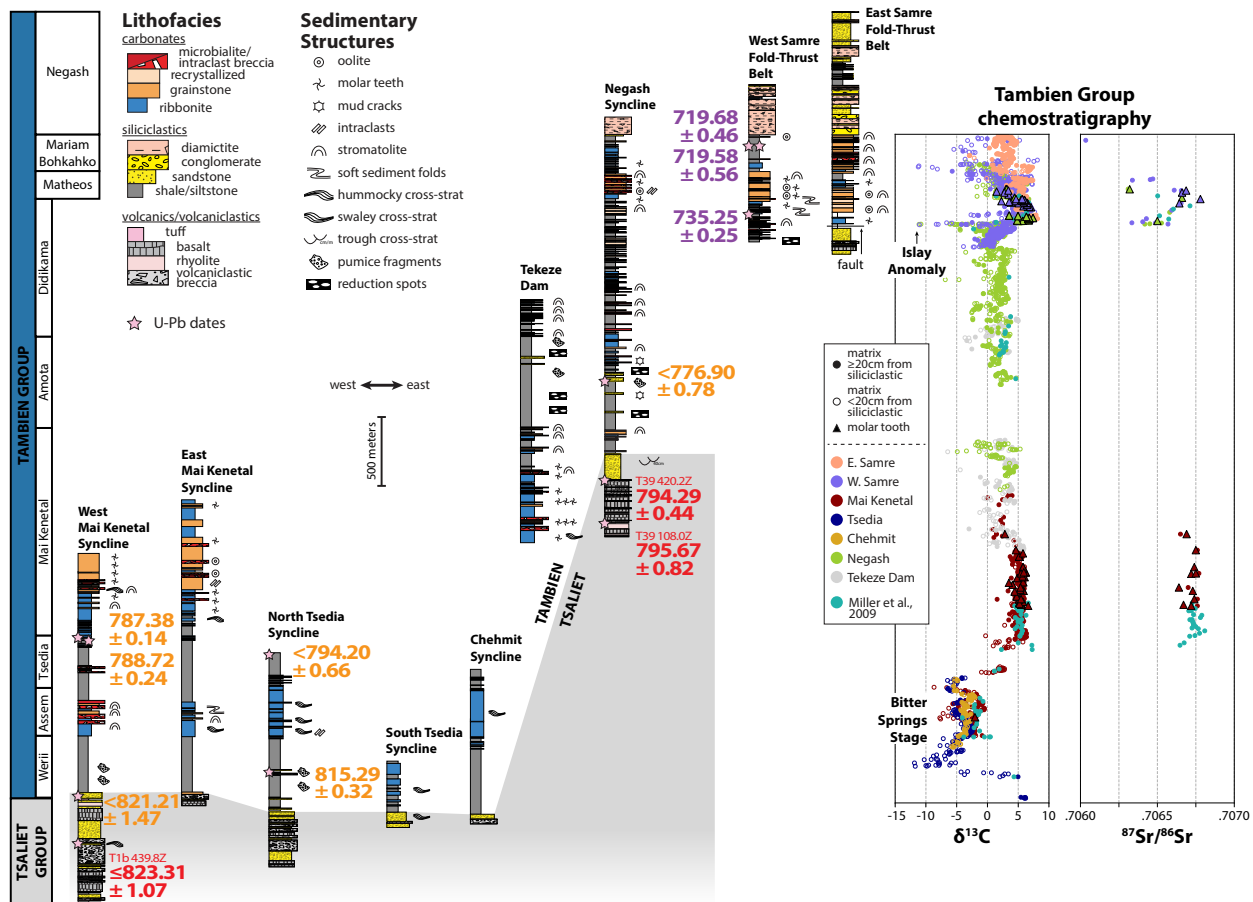


Figure 3. Representative simplified stratigraphy and $\delta^{13}\text{C}$ and ${}^{87}\text{Sr}/{}^{86}\text{Sr}$ chemostratigraphy of the Tambien Group. For the $\delta^{13}\text{C}$ chemostratigraphy, open circles denote samples that are <20 cm from the closest siliciclastic unit (see ‘Diagenetic Considerations’). Data from the Tsedia Syncline resolve the onset of the Bitter Springs Stage in Ethiopia, and data from the Samre Fold-Thrust Belt and the Negash Syncline resolve the recovery from the nadir of the Islay Anomaly (detailed in Fig. 8). U-Pb ID-TIMS dates are in units of Ma with uncertainties corresponding to the analytical uncertainty, which can be used for comparison between these dates since they were developed using the same tracer. Orange dates are from Swanson-Hysell et al. (2015), purple dates are from MacLennan et al. (2018), and red dates are from this study. These dates show that the transition from the volcanism of the Tsaliel Group to the sedimentation of the Tambien Group occurred significantly later in the Negash Syncline than in exposures further to the west.

99 821.2±1.5 Ma, and an eruptive age near the base of the Tambien Group (~150 m above the
100 Tsaliel-Tambien Group contact) of 815.29±0.32 Ma (Swanson-Hysell et al., 2015) constrains the

age of the Tsaliet to Tambien Group transition in the west (Fig. 3). U-Pb ID-TIMS dates of 719.58 ± 0.56 and 719.68 ± 0.46 Ma from tuffs ~80 m below the Negash Formation glacial deposits provide the best available age of those deposits and are consistent with a ca. 717 Ma onset of glaciation in the basin (Fig. 3; MacLennan et al., 2018). The strata subsequently were folded into a series of NNE-SSW oriented synclines (Fig. 1B) during the East African Orogeny (Stern, 1994), with maximum metamorphic temperatures estimated to have reached $<250^{\circ}\text{C}$ based on chlorite thermometry (Alene, 1998). Synchronous with and following this deformation was the emplacement of granitoid plutons, known as the Mereb Granitoids, into the Tambien Group (Fig. 1) with U-Pb dates of ca. 610 Ma (Miller et al., 2003; Avigad et al., 2007).

110 METHODS

111 Field Methods

112 Tambien Group rocks near the town of Samre previously were mapped as ‘undifferentiated
113 Neoproterozoic sedimentary rocks’ (Arkin et al., 1971), and no Neoproterozoic diamictite from the
114 region was reported in the literature, with the notable exception of a brief mention in Bussert
115 (2010). Our geologic mapping of this area has revealed extensive exposures of upper Tambien
116 Group strata including large areas of diamictite within a series of folds and thrust faults (Fig. 2).
117 We refer to this area as the Samre Fold-Thrust Belt, and differentiate units within it based on the
118 stratigraphic framework developed in the Negash Syncline (Swanson-Hysell et al., 2015) since the
119 lithostratigraphy of the strata correlates well between the two areas (Fig. 3). This stratigraphic
120 framework is contrary to an older framework proposed in Alene et al. (2006) and Miller et al.
121 (2009), which correlates the Didikama Formation in the Negash Syncline with the Assem
122 Formation in the synclines further to the west. Stratigraphic sections with good exposure were
123 identified and measured using a Jacob’s staff in both the Negash Syncline and the Samre
124 Fold-Thrust Belt. During the measurement of these sections, carbonate samples with minimal

125 visible alteration were collected for geochemical analysis.

126 **Geochemical Analyses**

127 Carbonate samples were cut perpendicular to bedding to expose a fresh surface before
 128 micro-drilling. Visibly altered zones of the fresh surface, such as those affected by veining and
 129 fractures, were avoided. The subsequent analyses described here were performed on aliquots of
 130 these micro-drilled powders.

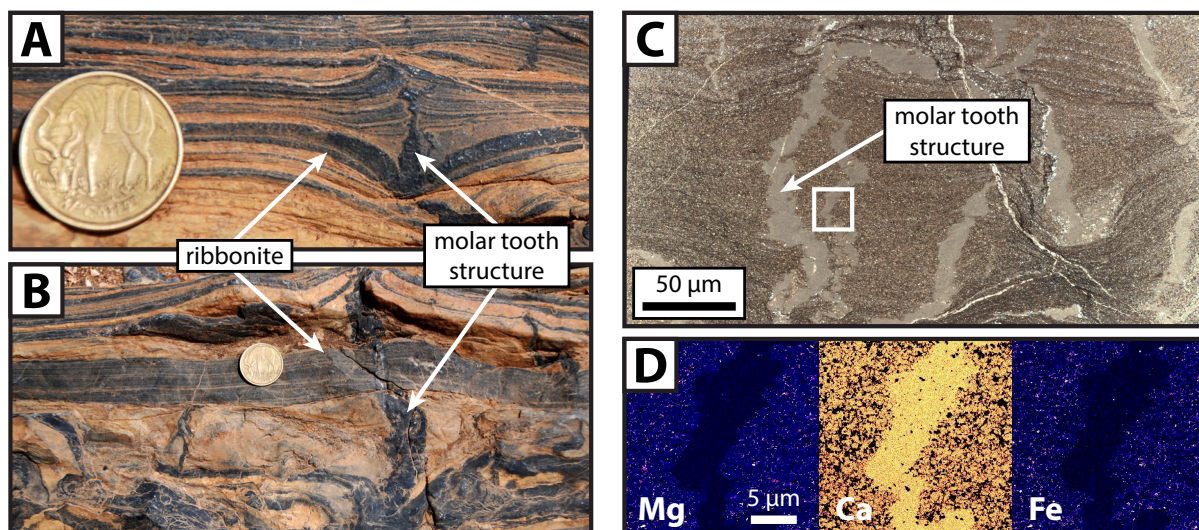


Figure 4. Molar tooth structures from the Tambien Group. (A) and (B) Photographs of molar tooth structures from the Mai Kenetal Formation, showing differential compaction of carbonate ribbonite around the structures. The 10 cent of Ethiopian birr coin used for scale has a diameter of 23 mm. (C) Photomicrograph of molar tooth structures within ribbonite of the Mariam Bohkahko Formation from the Negash Syncline taken using cross-polarized light. Thinning/thickening of sedimentary layers shows differential compaction of sediment around the structures. Inset box shows field of analysis for D. (D) Wavelength-dispersive x-ray spectroscopy elemental maps of a molar tooth structure, with warmer colours indicating higher concentration. The maps show the high purity of the microspar calcite in the molar tooth structures relative to the surrounding micrite matrix. Low Mg and high Ca suggests undolomitized calcite, and low Fe suggests a lack of a clay component or Fe-rich carbonate.

131 Previous work has determined that molar tooth structures typically consist of high purity

132 microspar calcite relative to the surrounding micrite host (Smith, 1968; Fairchild et al., 1997;
133 Pratt, 1998). These structures appear as subvertical dual-tapered carbonate-cement-filled cracks
134 that are generally <1 cm wide, and historically were interpreted to create a pattern on bedding
135 planes that resembles the upper surface of elephant molar teeth (Fig. 4; Bauerman, 1884; Daly,
136 1912). The differential compaction of sediment around molar tooth structures, which typically are
137 crumpled perpendicular to bedding planes, requires that molar tooth structures formed prior to
138 or during compaction and dewatering of the sediment. Hypotheses of molar tooth structure crack
139 formation are varied and include proposals that they formed as subaqueous shrinkage cracks
140 (Smith, 1968), through the expansion of gas from organic decay (Pollock et al., 2006), through
141 wave-induced cracking due to heaving of sediment (Bishop and Sumner, 2006), or through
142 microbial conversion of smectite to illite coupled with wave loading (Hodgskiss et al., 2018).
143 Regardless of the mode of crack formation, precipitation of calcite cement within the cracks
144 requires significant throughput of seawater through the cracks prior to or during dewatering and
145 lithification of the host carbonate mud.

146 Molar tooth structures occur in a number of formations in the Tambien Group (Fig. 3), often
147 in ribbonite (thinly bedded wavy- to parallel-laminated fine-grained limestone) that can exhibit
148 swaley cross-stratification. Petrographic work on molar tooth structure samples from the
149 Tambien Group show that these structures consist of high purity calcite microspar, whereas the
150 surrounding micrite can have a clay component (Fig. 4). Furthermore, in samples where the
151 surrounding micrite is partially dolomitized, molar tooth structures are not (Fig. 4), suggesting
152 that the structures are more resistant to dolomitization. Therefore, wherever possible, molar
153 tooth structure microspar calcite was targeted for geochemical analysis along with the host bulk
154 carbonate matrix.

155 **$\delta^{13}\text{C}$ and $\delta^{18}\text{O}$**

156 Carbonate powders were weighed out to 1 mg and heated to 110°C to remove any residual water.
157 Samples then were reacted with 250 μL of H_3PO_4 at 75°C. The resulting CO_2 gas was extracted
158 using a GasBench II auto-sampler and analyzed on a SerCon Callisto continuous-flow isotope
159 ratio mass spectrometry (CF-IRMS) system at Princeton University to obtain $\delta^{13}\text{C}$ and $\delta^{18}\text{O}$
160 values. Powders of NBS-19 ($\delta^{13}\text{C} = 1.95\text{\textperthousand}$ and $\delta^{18}\text{O} = -2.20\text{\textperthousand}$) and an internally calibrated
161 standard ($\delta^{13}\text{C} = -1.48 \pm 0.1\text{\textperthousand}$ and $\delta^{18}\text{O} = -8.54 \pm 0.1\text{\textperthousand}$) also were analyzed once every 10
162 samples to calibrate the sample measurements. Typical measured precision was $\sigma = 0.1\text{\textperthousand}$ for
163 $\delta^{13}\text{C}$ and $\sigma = 0.2\text{\textperthousand}$ for $\delta^{18}\text{O}$.

164 **Elemental Analysis**

165 Carbonate powders were weighed out to 10 mg and then reacted with 10.0 mL of pH = 4.9
166 buffered acetic acid solution (3 mL of glacial acetic acid and 3 mL of ammonium hydroxide for
167 every 497 mL of water) for 4-5 hours in a 25°C sonicator. Samples then were centrifuged, and
168 0.8 mL of the solution was extracted and mixed with 7.2 mL of 2% HNO_3 . These diluted samples
169 were simultaneously analyzed for Al, Ca, Fe, Mg, Mn, K, Na, and Sr on a Perkin Elmer 5300 DV
170 inductively coupled plasma optical emission spectrometer (ICP-OES) in the College of Natural
171 Resources at UC Berkeley. Raw measurements were transformed into concentrations using 6
172 internal standards of known concentration with 2% HNO_3 matrix (diluted from a commercial
173 standard of known concentration). Standard concentrations bracketed the concentrations
174 observed in samples. When the known concentrations were plotted against measured intensity,
175 linear fits through these 6 standards produced $R^2 > 0.98$ for Al and K, $R^2 > 0.999$ for Ca, Mg, and
176 Na, and $R^2 > 0.9999$ for Fe, Mn, and Sr.

¹⁷⁷ **⁸⁷Sr/⁸⁶Sr**

¹⁷⁸ Carbonate powders were weighed out to ~30 mg and washed 3 times in a 1.0 mL 1:1
¹⁷⁹ methanol:water solution to encourage the suspension of clays (McArthur et al., 2006). The
¹⁸⁰ samples then were reacted in an ultrasonic bath 3 times with 1.0 mL of 0.2 M ammonium acetate
¹⁸¹ to remove loosely bound Sr cations and rinsed in an ultrasonic bath 3 times with ultrapure water
¹⁸² to remove residual ammonium and clay. These cleaned samples were reacted with 1.0 mL of
¹⁸³ 0.5 M acetic acid, and any insoluble residue was removed via a centrifuge. The sample solutions
¹⁸⁴ then were dried down using heating lamps in a nitrogen atmosphere and then reacted with 250 μ L
¹⁸⁵ of 6 M HNO₃. Sr was isolated via standard column chemistry techniques using 100-150 μ m
¹⁸⁶ Sr-spec resin, dried down again with 3 drops of 15 M HNO₃, and then loaded onto single rhenium
¹⁸⁷ filaments in H₃PO₄ with a TaCl₅ activator. Strontium isotopes were measured on a
¹⁸⁸ ThermoFisher Triton thermal ionization mass spectrometer (TIMS) at the Center for Isotope
¹⁸⁹ Geochemistry at UC Berkeley using a static multicollection routine. Mass discrimination was
¹⁹⁰ corrected to ⁸⁶Sr/⁸⁸Sr = 0.11940. A minor correction ratio of <1.00003 also was applied to the
¹⁹¹ raw data to match the ⁸⁷Sr/⁸⁶Sr of blanks with NBS-987 (⁸⁷Sr/⁸⁶Sr = 0.710245), which was
¹⁹² analyzed alongside the samples.

¹⁹³ **U-Pb Geochronology**

¹⁹⁴ Zircons were extracted from rock samples at Princeton University by crushing using a jaw crusher
¹⁹⁵ and disc mill followed by magnetic and gravimetric separation. The zircon separates were
¹⁹⁶ annealed in quartz crucibles at 900°C for 48 to 60 hours. Individual zircons were photographed
¹⁹⁷ and transferred to microcapsules, after which 100 μ g of 29 M HF and 15 μ g of 30% HNO₃ were
¹⁹⁸ added. The microcapsules were put into a Parr bomb and placed in an oven at 195°C for 12 hours
¹⁹⁹ to chemically abrade the zircons, preferentially targeting metamict and damaged parts of the
²⁰⁰ zircon that have undergone Pb loss. After chemical abrasion, the zircon grains were rinsed in ten
²⁰¹ steps of alternating distilled 6 N HCl, 30% HNO₃ and MQ water. Distilled HF and HNO₃ were

202 again added, as well as the EARTHTIME ET535 tracer solution (Condon et al., 2015; McLean
203 et al., 2015), before total dissolution at 210°C for 48 hours. After total dissolution, the solutions
204 were dried down and converted to chlorides. U and Pb separation was performed using ion
205 exchange resin (Eichrom 200-400 mesh chloride form).

206 The U and Pb cut was dried down with a microdrop of dilute H₃PO₄. The dried U-Pb fraction
207 was redissolved in a silica gel emitter, and deposited onto outgassed zone-refined Re filaments. U
208 and Pb isotopic measurements were made using an IsotopX PhoeniX-62 TIMS at Princeton
209 University. Pb analyses were performed in peak hopping mode on a Daly photomultiplier ion
210 counting detector. U measurements were made either on the Daly photomultiplier in peak
211 hopping mode or as a static measurement on the Faraday cups connected to 10¹² ohm resistor
212 boards depending on the signal intensity. U was measured as an oxide. The Pb and U deadtime
213 characteristics of the Daly photomultiplier were monitored by running NBS982 and CRM U500
214 on a weekly basis. The NBS982 runs also were used to quantify Pb mass-dependent fractionation.
215 Unless stated otherwise, all U-Pb uncertainties reported in this manuscript are the internal
216 (analytical) uncertainties in the absence of all external or systematic errors, with these additional
217 uncertainties reported in Table 1.

218 LITHOSTRATIGRAPHY

219 From oldest to youngest, nine formations within the Tambien Group have been differentiated: the
220 Werii, Assem, Tsedia, Mai Kenetal, Amota, Didikama, Matheos, Mariam Bohkahko, and Negash
221 formations (Figs. 2 and 3; Swanson-Hysell et al., 2015). In the Negash Syncline, the Negash
222 Formation is limited in aerial extent to ~3 km² and is more penetratively foliated than most of
223 the Tambien Group since it is only exposed in the southern-most core of the syncline (Fig. 2).
224 Our team's mapping now has differentiated extensive exposures of the Negash Formation, along
225 with further exposures of the underlying strata, in the Samre Fold-Thrust Belt (Figs. 1 and 2).

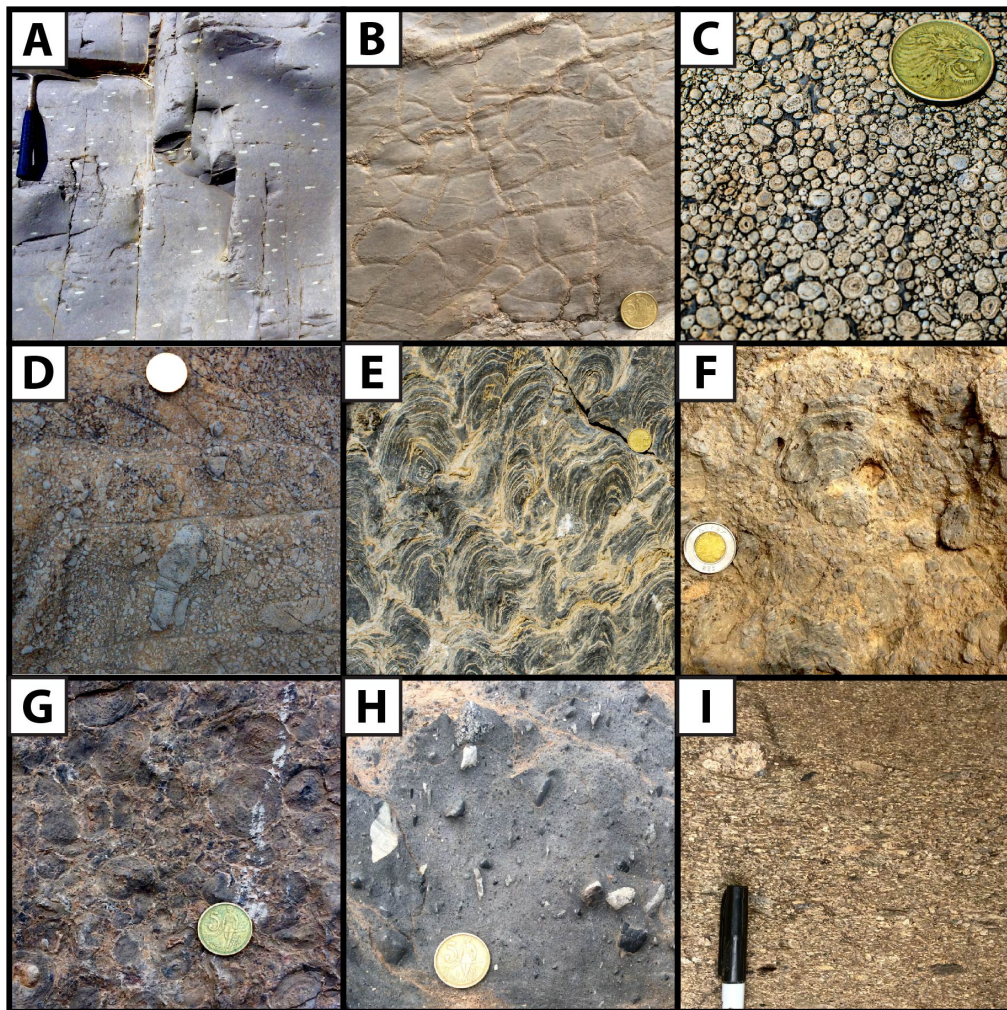


Figure 5. Photos of key lithofacies of the Tambien Group. **(A)** Reduction spots within the Amota Formation in the Negash Syncline. **(B)** Mud cracks within the Amota Formation in the Negash Syncline. **(C)** Oolite within the Matheos Formation in the Samre Fold-Thrust Belt. **(D)** Limestone intraclast breccia within the Matheos Formation in the Samre Fold-Thrust Belt. **(E)** Stromatolites at the base of the Mariam Bohkahko Formation in the western Samre Fold-Thrust Belt. **(F)** Carbonate breccia containing stromatolites from the Mariam Bohkahko Formation in the eastern Samre Fold-Thrust Belt. **(G)** Oncolite from near the top of the Mariam Bohkahko Formation in the Samre Fold-Thrust Belt. **(H)** Diamictite of the Negash Formation in the Samre Fold-Thrust Belt. **(I)** Lithic arkose coarse sandstone with sparse pebbles of the Negash Formation in the Samre Fold-Thrust Belt. The hammer used for scale in A has a length of 33 cm. The 5 cent of Ethiopian birr coin used for scale in B, C, D, E, G and H has a diameter of 20 mm. The 1 Ethiopian birr coin used for scale in F has a diameter of 27 mm. The pen used for scale in I has a width of 1 cm.

Table 1. Summary of CA-ID-TIMS $^{206}\text{Pb}/^{238}\text{U}$ dates from the Tsaliet and Tambien groups.

Sample	Description and Formation/Group	Latitude	$^{206}\text{Pb}/^{238}\text{U}$	Date (Ma)	Type	Reference
T1-12.3	volcaniclastic unit upper Tsaliet Grp.	14.044°N 38.955°E	<821.21 ±1.47	maximum depositional age from youngest concordant single crystal		Swanson-Hysell et al., 2015
TS22	tuff Werii Fm.	14.0382°N 39.1079°E	815.29 ±0.32/0.46/0.99	eruptive age from weighted mean (MSWD=0.52, n=5)		Swanson-Hysell et al., 2015
TS23	siltstone Tsedia Fm.	14.0379°N 39.1298°E	<794.20 ±0.66	maximum depositional age from youngest concordant single crystal		Swanson-Hysell et al., 2015
T2	tuff upper Tsedia Fm.	14.0437°N 38.9733°E	788.72 ±0.24/0.40/0.94	eruptive age from weighted mean (MSWD=1.2, n=6)		Swanson-Hysell et al., 2015
T1-1202	tuff upper Tsedia Fm.	14.0482°N 38.9757°E	787.38 ±0.14/0.35/0.91	eruptive age from weighted mean (MSWD=1.8, n=7)		Swanson-Hysell et al., 2015
T22-453	volcaniclastic unit Amota Fm.	13.8436°N 39.6397°E	<776.90 ±0.78	maximum depositional age from youngest concordant single crystal		Swanson-Hysell et al., 2015
T46-102.2Z	tuff lower Matheos Fm.	13.1588°N 39.2512°E	735.35 ±0.25/0.39/0.88	eruptive age from weighted mean (MSWD=0.36, n=5)		MacLennan et al., 2018
SAM-ET-04	tuff upper Mariam Bohkahko Fm.	13.1398°N 39.1763°E	719.68 ±0.46/0.54/0.94	eruptive age from weighted mean (MSWD=1.3, n=8)		MacLennan et al., 2018
SAM-ET-03	tuff upper Mariam Bohkahko Fm.	13.1398°N 39.1761°E	719.58 ±0.56/0.64/1.0	eruptive age from weighted mean (MSWD=0.54, n=3)		MacLennan et al., 2018
T1b-439.8Z	lava flow Tsaliet Grp.	14.0445°N 38.9522°E	<823.31 ±1.07	maximum eruptive age from youngest concordant single crystal	this study	
T39-108.0Z	ignimbrite Tsaliet Grp.	13.8488°N 39.6523°E	795.67 ±0.82/0.89/1.2	eruptive age from weighted mean (MSWD=0.084, n=3)	this study	
T39-420.2Z	tuff Sa'aga Fm. of the Tsaliet Grp.	13.8509°N 39.6499°E	794.29 ±0.44/0.51/0.99	eruptive age from weighted mean (MSWD=0.21, n=5)	this study	

Notes:

2σ uncertainties are reported in the format $\pm X/Y/Z$, where X is the internal (analytical) uncertainty in the absence of all external or systematic errors, Y is the uncertainty incorporating the U-Pb tracer calibration error, and Z is the uncertainty including X and Y, as well as the uranium decay constant uncertainty; MSWD = mean square of weighted deviates; n = number of zircon analyses included in the calculated date.

226 Western Exposures

227 In broad terms, mapping of the Tambien Group to date has revealed that older formations are
228 exposed in the western synclines and younger formations are exposed in the eastern synclines,
229 with the Tekeze Dam Region in the southwest exposing stratigraphy that links the two areas
230 (Swanson-Hysell et al., 2015). We define western Neoproterozoic exposures as the Mai Kenetal
231 Syncline, Tsedia Syncline, Chehmit Syncline, and Tekeze Dam Region (Fig. 1).
232 Lithostratigraphic correlation between these four areas is relatively straightforward, although
233 there is notable lateral variability (Fig. 3).

234 Tsaliet Group

235 The Tsaliet Group is comprised of basaltic to intermediate lava flows, volcaniclastic breccias, and
236 ignimbrites (Fig. 3). The lava flows can have vesiculated flow tops and are sometimes porphyritic
237 with tabular plagioclase phenocrysts. The volcaniclastic breccias have clasts as large as boulders
238 and dominate portions of the group where there are few flows. The presence of flows and the
239 ubiquity of large volcanic clasts in the breccias suggest that deposition of the Tsaliet Group
240 would have happened on or immediately adjacent to an arc.

241 A maximum depositional age of 821.21 ± 1.47 Ma (youngest concordant U-Pb date) from a
242 volcaniclastic unit in the Mai Kenetal Syncline within 75 m of the top of the Tsaliet Group
243 (Swanson-Hysell et al., 2015) has been the best available constraint on the start of Tambien
244 Group deposition. In this study, we report a U-Pb date of 823.31 ± 1.07 Ma from the youngest
245 concordant grain analyzed within a lava flow ~250 m below the top of the Tsaliet Group of the
246 western limb of the Mai Kenetal Syncline (Figs. 3 and 6; Table 1), constraining the flow to be
247 this age or younger.

248 Werii Formation

249 The Werii Formation is a ~400-500 m thick sequence of siltstones and very fine sandstones
250 exposed in the Mai Kenetal, Chehmit, and Tsedia synclines, except in the southwestern Tsedia
251 Syncline where previously unreported limestone ribbonite horizons are interbedded within
252 siltstones (Fig. 3). The transition from the Tsaliet Group to the Werii Formation appears
253 conformable where observed with decreasing volcaniclastics up stratigraphy. An eruptive age from
254 a tuff within 150 m of the bottom of the Werii Formation in the Tsedia Syncline of
255 815.29 ± 0.32 Ma (Swanson-Hysell et al., 2015) is consistent with this interpretation of
256 conformable deposition when compared to the age constraints within the upper Tsaliet Group.

257 The strata contains large (up to 50 cm) hyper-vesiculated scoria bombs in the proximity of the
258 tuff that yields the 815.29 ± 0.32 Ma age. The presence of these bombs indicates that arc
259 volcanism remained nearby and active during the deposition of the Werii Formation, but was
260 more distal than during the deposition of flows and volcaniclastic breccias of the Tsaliet Group.

261 Assem Formation

262 The carbonate-dominated Assem Formation is ~200-300 m thick and is exposed in the Mai
263 Kenetal, Chehmit, and Tsedia synclines (Fig. 3). There is significant west-east lateral facies
264 variability in the Assem Formation. In the Mai Kenetal Syncline, ribbonite dominates at the base
265 of the formation, and transitions upwards into microbialaminite, stromatolite, and intraclast
266 breccia horizons. This sequence of lithofacies suggests shallowing through the deposition of the
267 Assem Formation such that the upper part of the formation was deposited in a high energy
268 environment within the photic zone. To the east, in the Tsedia and Chehmit synclines, the
269 formation is dominated by ribbonite with swaley cross-stratification likely developed by the
270 combined flow of storm waves. This west-east variability suggests transportation of carbonate
271 mud from a shallow-water microbial carbonate factory in the west out to greater depths to the

272 east.

273 **Tsedia Formation**

274 The Tsedia Formation is ~500 m thick and characterized by siltstones interbedded with
275 centimeter-scale carbonates. The formation is exposed in the Mai Kenetal, Chehmit, and Tsedia
276 synclines, and has transitional contacts with the underlying and overlying carbonate-dominated
277 units (the Assem and Mai Kenetal formations, respectively; Fig. 3). The full thickness of the
278 Tsedia Formation only is known to be exposed within the Mai Kenetal Syncline, as the formation
279 is the highest level of the stratigraphy exposed in the other places it has been mapped (Tsedia
280 and Chehmit synclines). However, exposure of the Tsedia Formation is poor throughout the Mai
281 Kenetal Syncline, with the best exposures as it transitions into the overlying Mai Kenetal
282 Formation.

283 U-Pb dates from tuffs within the Tsedia Formation constrain its age: from the Tsedia Syncline
284 there is a maximum depositional age constraint of 794.20 ± 0.66 Ma near the base of the
285 formation, and from the Mai Kenetal Syncline there are eruptive ages of 788.72 ± 0.24 and
286 787.38 ± 0.14 Ma near the top of the formation (Swanson-Hysell et al., 2015). These latter two
287 eruptive dates are from tuffs ~25 m below the base of the Mai Kenetal Formation.

288 **Mai Kenetal Formation**

289 The Mai Kenetal Formation is ~1400 m thick and dominated by carbonate lithofacies. In the
290 western exposures, the formation is exposed in the Mai Kenetal Syncline and Tekeze Dam Region
291 (Fig. 3). The lower part of the formation consists of ribbonite carbonate with abundant
292 hummocky and swaley cross-stratification occasionally interbedded with siltstones, suggesting
293 deposition at intermediate depths that commonly experienced combined waves and currents.
294 These strata transition into a series of shallowing-upward parasequences defined by siltstone,
295 ribbonite, grainstone, and intraclast breccia. Well-developed molar tooth structures (Figs. 4 and

296 5) are abundant throughout the formation. This formation represents the youngest rocks of the
297 Tambien Group known to be exposed in the Mai Kenetal Syncline.

298 **Amota Formation**

299 The Amota Formation is a ~500 m thick siliciclastic unit exposed in the Tekeze Dam Region and
300 the Negash Syncline of the eastern exposures (Fig. 3). Reduction spots (flattened green ellipsoids
301 ~1-3 cm long) frequently contrast against the purple of the siltstones within this formation (Fig.
302 5). In some cases, the reduction spots are cored with recrystallized minerals, including chlorite,
303 that may have originated as pumice that sank into the depositional environment of the siltstone.
304 In the Tekeze Dam Region, the formation is comprised of relatively homogenous purple siltstones
305 with rare sandstone interbeds.

306 **Didikama Formation**

307 Like the Amota Formation, the only documented exposure of the Didikama Formation in the
308 western exposures is in the Tekeze Dam Region (Fig. 3). The formation represents the highest
309 exposed stratigraphy of the Tambien Group currently recognized in the western exposures.
310 Carbonates within the formation are extensively dolomitized and recrystallized resulting in pale
311 brown carbonate beds interbedded with siltstones. Primary features within the carbonates of the
312 formation can be obscured by the recrystallization associated with dolomitization, but in places
313 primary ribbonites and grainstones can be identified. Stromatolites also are found in the
314 formation at the top of shallowing-upward parasequences comprised of ribbonites, grainstones,
315 and siltstones. Taken together, these lithofacies are indicative of deposition in a generally
316 shallow-water environment.

317 Eastern Exposures

318 For the purposes of this discussion, we define eastern Neoproterozoic exposures as the Negash
319 Syncline and the Samre Fold-Thrust Belt (Figs. 1 and 2). The broad similarity of the
320 stratigraphy between these two regions (a present day lateral distance of ~100 km) may indicate
321 that the Tambien basin was elongate along the present day NNE-SSW direction.

322 The Werii, Assem, Tsedia, Mai Kenetal, Amota, and Didikima formations in the western
323 exposures can be stratigraphically linked to the Mai Kenetal, Amota, Didikama, Matheos,
324 Mariam Bohkahko, and Negash formations in the eastern exposures by Mai Kenetal, Amota, and
325 Didikama formation stratigraphy exposed in the Tekeze Dam Region (Fig. 3; Swanson-Hysell
326 et al., 2015).

327 Within the Samre Fold-Thrust Belt, there are notable differences in the lithofacies of the
328 Mariam Bohkahko and Negash formations across the major NE-striking thrust fault in the
329 mapped area (the Zamra Fault), with the exposure of these formations west of the fault having
330 greater broad-scale similarity with the formations in the Negash Syncline (Figs. 2, 3, and 7).

331 Tsaliet Group

332 Similar to the exposures in the west, the Tsaliet Group in the eastern exposures in the proximity
333 of the Tambien Group is comprised of basaltic to intermediate lava flows, volcaniclastic breccias,
334 and ignimbrites. However, its contact with the Tambien Group in the eastern exposures is
335 different from that in the west. Where this contact is exposed in the Negash Syncline, the top
336 ~150 m of the Tsaliet Group is comprised of immature sandstone dominated by basaltic lithic
337 clasts (the Sa'aga Formation; Fig. 3). The Sa'aga Formation sandstone contains large dune-scale
338 cross-beds with faint pinstripe laminations and amplitudes of up to 2 m, suggesting an aeolian
339 depositional environment. This lithofacies indicates subaerial deposition on weathering arc
340 volcanics as the basin transitioned from Tsaliet Group volcanics into Tambien Group marine

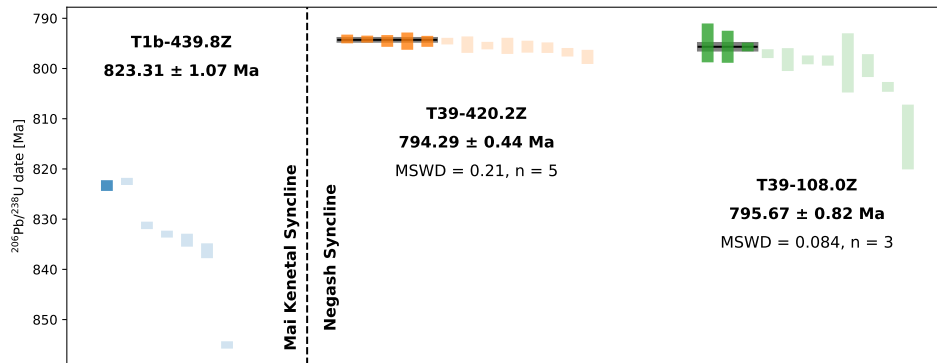


Figure 6. U-Pb ID-TIMS analyses for individual zircon grains. T1b-439.8Z is from the Tsaliyet Group in the Mai Kenetal Syncline, and T39-420.2Z and T39-108.0Z are from the Tsaliyet Group in the Negash Syncline (Fig. 3). Colored bars represent the 2σ uncertainty for the $^{206}\text{Pb}/^{238}\text{U}$ date of each zircon. Darker colored bars represent zircons included in the calculation of the weighted mean. Reversely discordant zircons are not shown. The black line and grey box represent the calculated weighted mean and 2σ uncertainty respectively. MSWD = mean square of weighted deviates; n = number of zircon analyses included in the calculated date. Concordia diagrams, data tables, and sample photos are included in the data repository.

341 sediments. We present eruptive ages of 794.29 ± 0.44 Ma from a 30 cm rhyolitic tuff near the base
 342 of the immature sandstone, and 795.67 ± 0.82 Ma from an ignimbrite \sim 300 m below the rhyolitic
 343 tuff within the volcanic succession (Figs. 3 and 6; Table 1). These ages are \sim 25 Myr younger
 344 than the contact between the Tsaliyet and Tambien groups in the western exposures (Fig. 3).
 345 Previous correlation schemes of the Tambien Group have interpreted the Didikama Formation in
 346 the Negash Syncline to correlate with the Assem limestone in the west and the Matheos limestone
 347 in the Negash Syncline to correlate with the Mai Kenetal limestone in the west (Alene et al.,
 348 2006; Miller et al., 2009). These dates indicate that Tambien Group deposition was not occurring
 349 in the east at the time of deposition of the Werii and Assem formations in the west, and that the
 350 Didikama Formation does not correlate to the Assem Formation. Rather, the Tsaliyet-Tambien
 351 contact is significantly diachronous across the region, with local volcanism continuing to generate
 352 the lava flows of the Tsaliyet Group in the east while Tambien Group sediment deposition had
 353 already begun in the west. Sedimentation across the region was ongoing by ca. 793 Ma.

354 In the Samre Fold-Thrust Belt, the Tsaliyet Group only has been mapped in a small area at the

355 eastern limit of Neoproterozoic exposure in this locality (Fig. 2). In that area, basaltic to
356 intermediate lava flows are overlain by immature sandstone, similar to what is observed at the top
357 of the Tsaliet Group in the Negash Syncline. However, the immature sandstone in the Samre
358 Fold-Thrust Belt lacks cross-stratification and pinstripe laminations - instead, it is largely
359 massive, with parallel laminations only being observed in a few outcrops. Furthermore, in the
360 Samre area, the contact between the Tsaliet Group and the overlying Tambien Group only has
361 been mapped where the two are in fault contact.

362 Mai Kenetal Formation

363 In the Negash Syncline, the base of the Tambien Group is comprised of siltstones interbedded
364 with dolomitized carbonates (Fig. 3). Rare cm-scale horizons of calcite pseudomorphs after
365 gypsum can be found within the siltstones. We tentatively correlate this sequence of lithofacies
366 with the Mai Kenetal Formation in the western exposures based on two observations. First, these
367 sediments underlie lithofacies that are suggestive of the Amota Formation in the western
368 exposures. Second, as discussed above, deposition of the Mai Kenetal Formation began ca.
369 787 Ma in the western exposures. This age is younger, but similar, to the age of 794.29 ± 0.44 Ma
370 developed from the base of the immature sandstone in the Tsaliet Group of the Negash Syncline.

371 However, there are significant differences between what we are considering the Mai Kenetal
372 Formation in the east relative to the formation in the west. The carbonates of the formation are
373 more extensively dolomitized and the overall ratio of carbonate to siliciclastics is much lower in
374 the Negash Syncline. Molar tooth structures and ooids that are abundant in the formation within
375 the western exposures are not present in the formation within the Negash Syncline. Furthermore,
376 the lithofacies with calcite pseudomorphs after gypsum in the Negash exposures is not found in
377 the western exposures. These differences likely are associated with deposition of the Mai Kenetal
378 Formation at Negash occurring more proximal to the arc than in the western exposures, which
379 could have led to periodic restriction and evaporite mineral precipitation at Negash but not

380 further west.

381 **Amota Formation**

382 The Amota Formation is exposed in the Negash Syncline in the eastern exposures, and is similar
383 to that in the western exposures (Fig. 3). Relatively homogenous purple siltstones with green
384 reduction spots dominate the formation, with less frequent sandstone interbeds. Deposition of the
385 Amota Formation in the Negash Syncline occurred in shallow waters: coarse sandstones and
386 pebble to cobble conglomerates are relatively abundant, very fine sandstones and siltstones often
387 are ripple cross-stratified, and there are horizons of mud cracks (Fig. 5). These lithofacies indicate
388 that the Amota Formation was deposited in shallower waters in the eastern exposures relative to
389 the west, where mud cracks and lithologies coarser than fine sandstone have not been observed.

390 **Didikama Formation**

391 At present, the Didikama Formation is the lowest Tambien Group formation unambiguously
392 identified in the Samre Fold-Thrust Belt. Preliminary reconnaissance mapping identified
393 lithofacies that may be correlative with the Amota Formation in the westernmost portion of the
394 currently mapped Samre Fold-Thrust Belt area (Fig. 2). However, further work is required to
395 substantiate this correlation.

396 The Didikama Formation exposures in the east are similar to those in the west. Pale brown
397 dolomitized and recrystallized carbonate beds are interbedded with siltstones, and primary
398 sedimentary structures often are obscured by the dolomitization. Stromatolites are found near
399 both the top and bottom of the formation. An interval of black shale was observed at two
400 locations near the top of the formation on the eastern limb of the Negash Syncline.

401 The full thickness of the Didikama Formation only has been documented in the Negash
402 Syncline. However, parasitic folds (~10-100 m in scale) within the larger Negash Syncline

403 structure are concentrated within the Didikama Formation, making it difficult to accurately
404 estimate the true stratigraphic thickness of the formation. Nevertheless, our mapping and
405 stratigraphic measurements suggest that the formation is ~1200 m thick (Fig. 3).

406 **Matheos Formation**

407 The Matheos Formation is dominated by limestone and has a thickness ~150-350 m in the
408 Negash Syncline and the Samre Fold-Thrust Belt (Figs. 3 and 7). In both localities, the blue-grey
409 limestones of the formation form topographic ridges that are readily identified both in the field
410 and from satellite imagery. In contrast to the Didikama Formation, primary textures are
411 well-preserved.

412 In the Negash Syncline and west of the Zamra Fault in the Samre Fold-Thrust Belt, the
413 formation begins with grey ribbonite limestone with horizons of molar tooth structures and
414 transitions into grainstone with abundant oolite, intraclast breccia, and molar tooth structures
415 (Fig. 5). These lithofacies indicate that, in these areas, the formation represents a shallowing
416 upwards sequence with deposition occurring in an energetic shallow-water environment. East of
417 the fault, although the formation begins with the same grey ribbonite limestone with horizons of
418 molar tooth structures that is seen in the other areas, oolite and stromatolitic carbonates are the
419 dominant lithofacies (Fig. 7). Deposition of the Matheos Formation to the east of the Zamra
420 Fault also occurred in a shallow-water environment, but one dominated by stromatolites.

421 **Mariam Bohkahko Formation**

422 The Mariam Bohkahko Formation is exposed in the Negash Syncline and the Samre Fold-Thrust
423 Belt (Fig. 3). The beginning of the formation is marked by the end of the distinctive blue-grey
424 limestone facies of the Matheos Formation.

425 In the Negash Syncline and west of the Zamra Fault in the Samre Fold-Thrust Belt, the base

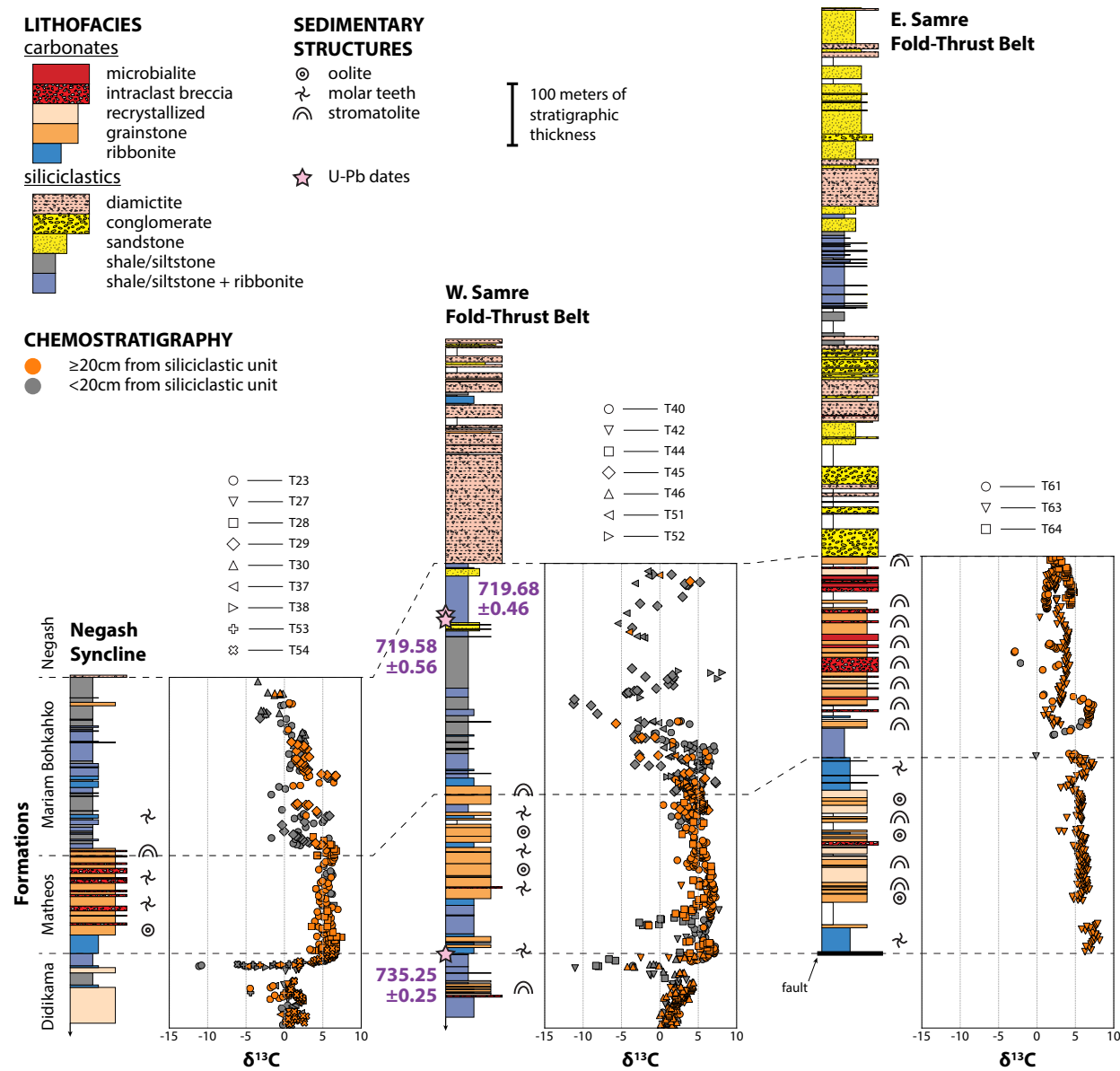


Figure 7. Lithostratigraphy and $\delta^{13}\text{C}$ chemostratigraphy of upper Tambien Group exposures in the Negash Syncline and Samre Fold-Thrust Belt (west and east of the Zamra Fault). The stratigraphic sections are a representative composite of individually measured sections in each locality with the data within the $\delta^{13}\text{C}$ composite keyed out to each individual section. $\delta^{13}\text{C}$ data are colored based on their stratigraphic distance from the closest siliciclastic unit (see ‘Diagenetic Considerations’). U-Pb dates are in units of Ma, and are from MacLennan et al. (2018).

426 of the Mariam Bohkahko Formation consistently is marked by partially dolomitized stromatolitic
427 carbonate (Figs. 5 and 7). These stromatolites are followed by mixed siliciclastic-carbonate
428 sedimentary rocks that are dominated by siltstone. The carbonate beds that are interbedded with
429 the siltstones often are boudined and dolomitized, likely due to their proximity to the core of the
430 large-scale synclines. There are slightly coarser-grained siliciclastics (up to very fine sandstone)
431 present toward the top of the formation, and some horizons are cross-stratified. In some areas,
432 climbing ripples, oolitic grainstones, and oncrites are observed within ~30 m of the top of the
433 Mariam Bohkahko Formation before the contact with the overlying Negash Formation (described
434 below), with carbonate grainstone beds within 1 m of the contact. Overall, these lithofacies
435 suggest deposition in a shallow-water environment, with sedimentation generally keeping pace
436 with subsidence.

437 East of the Zamra Fault, the base of the Mariam Bohkahko Formation consists of siltstones
438 with interbedded ribbonites (Fig. 7). The rest of the formation in this area is comprised almost
439 entirely of partially dolomitized carbonates, including stromatolites, oncrites, oolitic grainstone,
440 ribbonite, and intraclast breccia. Siliciclastics in the Mariam Bohkahko Formation east of the
441 major thrust fault are rare, and limited to siltstones in one or two intervals (based on different
442 sections) toward the bottom or middle of the formation. Toward the top of the formation, the
443 stratigraphy is comprised entirely of intact stromatolites, intraclast breccia with clasts of
444 stromatolites, and minor microbialaminite (Figs. 5 and 7). Again, overall, these lithofacies
445 suggest deposition in a shallow-water environment.

446 These differences in the stratigraphy of the Mariam Bohkahko Formation across the Zamra
447 Fault indicate different sediment sources and/or depositional environments and potentially
448 significant offset across the fault. To the east, the dominance of carbonate facies (including
449 stromatolites, oncrites, oolites, and microbialaminite) in the Mariam Bohkahko Formation
450 suggest deposition in a shallow-water tropical carbonate factory within the photic zone that lacks
451 significant siliciclastic sediment input. To the west, the dominance of siltstones with only minor

452 carbonate interbeds suggests higher siliciclastic sediment input into that portion of the basin.

453 Carbonate interbeds to the west likely represent redeposition of the carbonate sediment being

454 generated in the shallow-water carbonate factory to the east.

455 Negash Formation

456 The Negash Formation is exposed in the Negash Syncline and the Samre Fold-Thrust Belt (Fig.

457 3). In the Negash Syncline and west of the Zamra Fault in the Samre Fold-Thrust Belt, the

458 formation dominantly is comprised of massive diamictite with a silt matrix (Figs. 5 and 7). Clast

459 sizes within the diamictite are variable between pebble and boulder. Clast density also is variable,

460 with clast-poor versus clast-rich horizons. Clasts within the diamictite include carbonate

461 lithologies, some of which retain primary textures allowing them to be identified as ribbonites,

462 grainstone, and oolitic grainstone. Although not uniquely diagnostic, the facies as well as the

463 carbon isotope composition of these carbonate clasts (see ‘Diagenetic Considerations’) are

464 consistent with the interpretation that they were derived from the Tambien Group and point to

465 an intra-basinal source. In addition to carbonate clasts, clasts of sandstone, quartz, rhyolite,

466 meta-basalt, volcaniclastic breccia, aplite, and granite are present. Detrital zircon geochronology

467 (U-Pb SHRIMP) conducted on matrix combined with clasts of the Negash Formation collected in

468 the Negash Syncline revealed dates dominantly between 850 and 750 Ma with a minor population

469 between 1050 and 950 Ma (Avigad et al., 2007). Many of these lithologies, as well as the 850 to

470 750 Ma zircons, could have been sourced from rocks associated with the Arabian-Nubian arcs,

471 some of which had collided and amalgamated by that time (Johnson, 2014). However, the 1050 to

472 950 Ma zircons, as well as the granitoid clasts, are likely of extra-basinal origin, which is

473 consistent with the interpretation that the diamictite is glaciogenic. A minor portion of the Negash

474 Formation in these areas is comprised of facies that are distinct from the massive diamictite with

475 silt matrix, including: diamictite with a coarse sand matrix, pebble to cobble conglomerates with

476 carbonate and/or metavolcanic clasts, limestone ribbonite, lithic arkose fine to coarse sandstones

477 (likely sourced from the proximal arc) with rare pebbles/cobbles, and clast-free sandstone and
478 siltstone (Fig. 7).

479 The Negash Formation frequently is foliated in the core of the Negash Syncline, but also in
480 some outcrops in the Samre Fold-Thrust Belt. This foliation can make it difficult to confidently
481 identify glacigenic sedimentary textures, such as deformation of layers associated with dropstones,
482 and to liberate clasts for the observation of striations. Nevertheless, MacLennan et al. (2018) and
483 Miller et al. (2003) identified grooves on cobbles that were interpreted as striations of glacial
484 origin.

485 East of the Zamra Fault, the Negash Formation is significantly more variable than that west of
486 the fault and in the Negash Syncline, with a smaller proportion of the stratigraphy comprised of
487 massive diamictite (Fig. 7). The base of the formation in this area can either be massive
488 diamictite, or a clast-supported breccia composed of carbonate clasts within a dolomitized
489 carbonate matrix that have facies that are identical to those found in the underlying Mariam
490 Bohkahko (stromatolite and stromatolite breccia) and Matheos (oolite) formations (Fig. 5). This
491 carbonate breccia is overlain by cm-scale fining upward sequences of very fine to fine sandstone.
492 These sequences transition into massive diamictite interbedded with medium to coarse sandstones
493 and the carbonate breccia described previously, followed by an interval of siltstones interbedded
494 with cm-scale carbonate ribbonites and occasionally horizons of cm-scale coarse poorly sorted
495 sandstones that consist of limestone and lithic fragments. The ribbonites from within this interval
496 are likely the fine-grained products of redeposition of eroded underlying Tambien Group
497 carbonates, given that carbonate precipitation is expected to be thermodynamically inhibited in
498 the cold waters of a global glaciation. Glacigenic lithofacies above and below this interval are
499 almost identical, and the cm-scale carbonate beds are distinct from the thick Sturtian cap
500 carbonate sequences observed in other localities (Kennedy et al., 1998; Hoffman et al., 2011). To
501 date, no tuffs have been observed in the Negash Formation, preventing the development of direct
502 geochronological constraints on the formation. The stratigraphically highest observed exposures

503 of the Negash Formation in this eastern Samre Fold-Thrust Belt consist of intervals of massive
504 diamictite with a fine to coarse sand matrix and lithic arkose fine to coarse sandstones with rare
505 pebbles/cobbles. Similar to the Mariam Bohkahko Formation, this difference in the stratigraphy
506 of the Negash Formation across the Zamra Fault could be explained by significant
507 post-depositional offset across the fault, juxtaposing two locales with different depositional
508 environments and/or sediment sources that were once further apart.

509 Basin Development

510 Deposition in a back-arc basin is consistent with the geologic context of the Tambien Group.
511 Other sedimentary sequences overlying ca. 850-800 Ma volcanics in western Eritrea and northern
512 Ethiopia have been interpreted as being deposited in back-arc basins on the basis of the
513 trace-element composition of the volcanics and field relationships between the sedimentary
514 sequences and adjacent oceanic-arc rocks (Tadesse et al., 1999; Teklay et al., 2003; Teklay, 2006).
515 Mapping within the Arabian-Nubian Shield of Ethiopia, Sudan, and Eritrea has identified several
516 ophiolites within roughly north-south trending suture zones (Berhe, 1990). U-Pb crystallization
517 ages from Arabian-Nubian Shield volcanic and plutonic rocks are dominantly Tonian to
518 Cryogenian in age (Johnson, 2014), Sm-Nd isotopes indicate derivation from juvenile mantle
519 sources, and Nd model ages are dominantly Tonian to Cryogenian (Johnson, 2014). Together,
520 these data support a model wherein the Arabian-Nubian Shield formed through the
521 amalgamation of multiple arcs and associated arc-related basins.

522 The Tsaliet Group underlying the Tambien Group consists of volcanic flows and volcaniclastic
523 sediments that likely were deposited on the margins of a volcanic arc. The transition from
524 volcanic and volcaniclastic lithologies to the mixed siliciclastic-carbonate sediments of the
525 Tambien Group could be associated with slab rollback that caused the arc to migrate away from
526 the initial site of eruption and volcaniclastic deposition, resulting in extensional fault-driven
527 accommodation space followed by thermal-isostatic subsidence. The ages of 795.67 ± 0.82 and

528 794.29±0.44 Ma from within and above the lava flows of the Tsaliel Group in the Negash
529 Syncline of the eastern exposures are considerably younger than the eruptive age of
530 815.29±0.32 Ma from a tuff within siltstones in the basal Tambien Group in the Tsedia Syncline
531 of the western exposures (Swanson-Hysell et al., 2015), which indicates that local volcanism
532 continued to generate lava flows in the Negash Syncline while Tambien Group deposition already
533 had begun in the western exposures. This diachronous timing of the transition from volcanism to
534 sedimentation from west to east supports a back-arc basin setting, with the locus of volcanism
535 (recorded as the lava flows in the Tsaliel Group) migrating eastward in present day coordinates.
536 Slab rollback as a process causing arc migration and accommodating back-arc basin development
537 has been well-documented in the the more recent geologic record (e.g. Uyeda and Kanamori,
538 1979; Kastens et al., 1988; Schellart et al., 2006). Furthermore, the broad similarity of the
539 stratigraphy between the Negash Syncline and the Samre Fold-Thrust Belt (a present day lateral
540 distance of ~100 km, which has likely changed little since the time of deposition since the axis of
541 compression during the East African Orogeny was oriented approximately perpendicular to the
542 axis that spans these two locations; Stern, 1994) suggests that the Tambien basin was elongate
543 along the present day NNE-SSW direction. This geometry is consistent with structural inversion
544 of a back-arc basin from an extensional to a compressional regime, since the major structural
545 features (synclines, anticlines, and thrust faults) also have NNE-SSW orientations. Tuffs near the
546 base of the Tambien Group also have pumice fiamme and are associated with cobble to
547 boulder-sized scoria bombs indicating proximity to an active arc (Swanson-Hysell et al., 2015). In
548 contrast, tuffs higher in the group are more consistent with having formed through air-fall ash
549 sourced from active arcs further from the basin. Lithofacies of the upper Tsaliel Group and Mai
550 Kenetal and Amota formations also suggest shallower deposition in the eastern exposures relative
551 to the lithofacies of these formations in the west (see ‘Lithostratigraphy’), which again supports
552 eastward migration of volcanism and associated transgression in this basin. We note, however,
553 that the presence of facies indicating deposition above wave base throughout the Tambien Group
554 indicates that deposition of the siliciclastic and carbonate sediments overall kept pace with

555 subsidence. The lifespan of Tambien Group deposition (>100 Myr) also is similar to that of other
556 identified back-arc basins in the geologic record (Woodcock, 2004).

557 TAMBIEN GROUP CHEMOSTRATIGRAPHY

558 Stratigraphic sections across the Tambien Group are correlated to one another by aligning both
559 the characteristic lithofacies of the formations and the $\delta^{13}\text{C}$ curve to create a composite Tambien
560 Group $\delta^{13}\text{C}$ and $^{87}\text{Sr}/^{86}\text{Sr}$ chemostratigraphic record (Fig. 3). All geochemical data and the
561 Python code used to assess the degree of alteration of each sample and develop the composite
562 Tambien Group chemostratigraphy are included in the data repository. $\delta^{13}\text{C}$ and $^{87}\text{Sr}/^{86}\text{Sr}$ data
563 developed by Miller et al. (2009) also are incorporated into our Tambien Group composite. Given
564 that the data from Miller et al. (2009) were collected from surface transects rather than measured
565 stratigraphic sections, integration into our chemostratigraphic data set was made based on: A)
566 correlation of sampling localities (shown on maps in Miller et al., 2009) to our geological maps; B)
567 correlation of sample height and formation (shown approximately in fence diagrams in Miller
568 et al., 2009) to our measured sections; and C) correlation of $\delta^{13}\text{C}$ values.

569 Chemostratigraphic Results

570 Paired $\delta^{13}\text{C}$ data and $^{206}\text{Pb}/^{238}\text{U}$ dates from the lower Tambien Group have lead to the
571 interpretation that the negative $\delta^{13}\text{C}$ values within the Assem Formation correlate with the ca.
572 810-790 Ma Bitter Springs Stage (Swanson-Hysell et al., 2015). However, samples that resolved
573 the onset of the stage (i.e. the descent from $\sim 5\text{\textperthousand}$ to $\sim -4\text{\textperthousand}$) had not been identified, due to a
574 lack of carbonate horizons in the lower Tambien Group. New $\delta^{13}\text{C}$ data from carbonates within
575 the lower Werii Formation in the southwestern Tsedia Syncline begin at values of $\sim 5\text{\textperthousand}$ and fall
576 sharply to $<-5\text{\textperthousand}$, with values of $\sim -5\text{\textperthousand}$ for the rest of the Werii Formation, similar to those in the
577 overlying Assem Formation (Fig. 3). We interpret these $\delta^{13}\text{C}$ data to reflect the onset of the

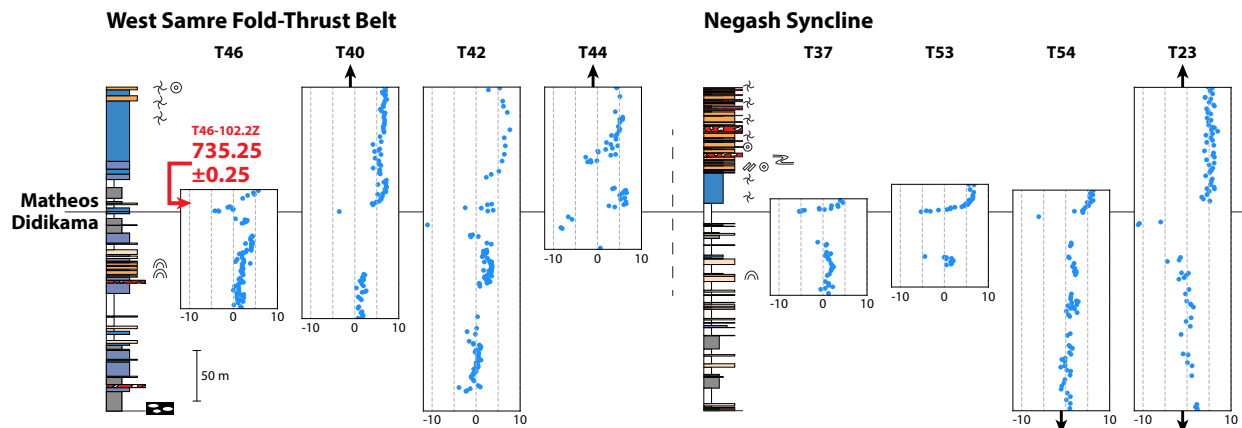


Figure 8. Summary lithostratigraphy and $\delta^{13}\text{C}$ data from sections that capture the Islay Anomaly from the Samre Fold-Thrust Belt and Negash Syncline. The symbology for the lithofacies and sedimentary structures is the same as that used in Figure 3. Black arrows indicate that lithostratigraphic and $\delta^{13}\text{C}$ data continues upwards/downwards for that section, but is not shown.

578 Bitter Springs Stage, which further supports the hypothesis that the stage represents a rapid
 579 onset/recovery, but sustained duration, global perturbation to the carbon cycle (Maloof et al.,
 580 2006; Swanson-Hysell et al., 2015). After the recovery from the Bitter Springs Stage, $\delta^{13}\text{C}$ values
 581 are sustained at $\sim 5\text{\textperthousand}$, before the stratigraphy transitions from the carbonate-dominated Mai
 582 Kenetal Formation to the mixed carbonate-siliciclastic Amota and Didikama formations. $\delta^{13}\text{C}$
 583 values from carbonates within these mixed carbonate-siliciclastic formations are more scattered
 584 than in carbonate-dominated formations. Nevertheless, the majority of the data through the
 585 Amota and Didikama formations lie between 0 and 5\textperthousand , and no major excursions are observed.
 586 Near the contact between the Didikama and Matheos formations, a large $\delta^{13}\text{C}$ excursion to
 587 $\sim -12\text{\textperthousand}$ is observed that we interpret to be the Islay Anomaly (Swanson-Hysell et al., 2015;
 588 MacLennan et al., 2018). This $\delta^{13}\text{C}$ excursion now is reproduced in eight sections across the basin
 589 (Fig. 8). Following the Islay Anomaly, $\delta^{13}\text{C}$ values are steady at $\sim 5\text{\textperthousand}$, before the stratigraphy
 590 transitions from the Matheos Formation to the Mariam Bohkahko Formation, which has more
 591 variable $\delta^{13}\text{C}$ values. However, we attribute the majority of this scatter within the Mariam
 592 Bohkahko Formation to alteration processes that drive $\delta^{13}\text{C}$ to more negative values (see

593 ‘Diagenetic Considerations’), and thus we interpret the primary $\delta^{13}\text{C}$ values to be broadly
594 declining from $\sim 5\text{\textperthousand}$ to $\sim 2\text{\textperthousand}$ in the interval between the Islay Anomaly and the onset of the
595 Sturtian Glaciation (Fig. 7).

596 $^{87}\text{Sr}/^{86}\text{Sr}$ data that we interpret to be primary (see ‘Diagenetic Considerations’) have
597 relatively stable values of ~ 0.7067 in the Mai Kenetal Formation (Fig. 3). These data are
598 followed by a large gap before values of ~ 0.7063 at the base of the Matheos Formation (Fig. 3).
599 Through the Matheos Formation, $^{87}\text{Sr}/^{86}\text{Sr}$ rises to ~ 0.7067 , before declining to ~ 0.7063 in the
600 middle of the Mariam Bohkahko Formation. One sample within 25 m of the contact between the
601 Mariam Bohkahko and Negash formations is interpreted to retain primary $^{87}\text{Sr}/^{86}\text{Sr} = \sim 0.70603$.
602 However, this sample ($[\text{Sr}] = 1408 \text{ ppm}$ and $\text{Mn/Sr} = 0.34$) barely passes our filtering thresholds
603 used to assess alteration. Although the $^{87}\text{Sr}/^{86}\text{Sr}$ of this sample seems to lie on the projected
604 trajectory of declining $^{87}\text{Sr}/^{86}\text{Sr}$ in the upper Mariam Bohkahko Formation (Fig. 3), more data
605 from the time interval immediately preceding the onset of the Sturtian Glaciation is required to
606 test whether our interpretation of the primary nature of the $^{87}\text{Sr}/^{86}\text{Sr}$ of this sample is robust.

607 Diagenetic Considerations

608 Filtering Samples Adjacent to Siliciclastic Units

609 Some of the proposed mechanisms for cooling and the initiation of the Sturtian Snowball Earth
610 have invoked connections between global glaciation and a negative $\delta^{13}\text{C}$ excursion leading into the
611 glaciation. Therefore, constraining the carbon isotopic composition of marine dissolved inorganic
612 carbon during the lead-up to the Sturtian Snowball Earth is particularly important for testing
613 these hypotheses.

614 There is substantial variability (up to $\sim 10\text{\textperthousand}$) in the carbon isotopic composition of
615 stratigraphically equivalent Mariam Bohkahko Formation carbonates immediately preceding the
616 glacial deposits of the Negash Formation (Fig. 7). This variability is most pronounced in the

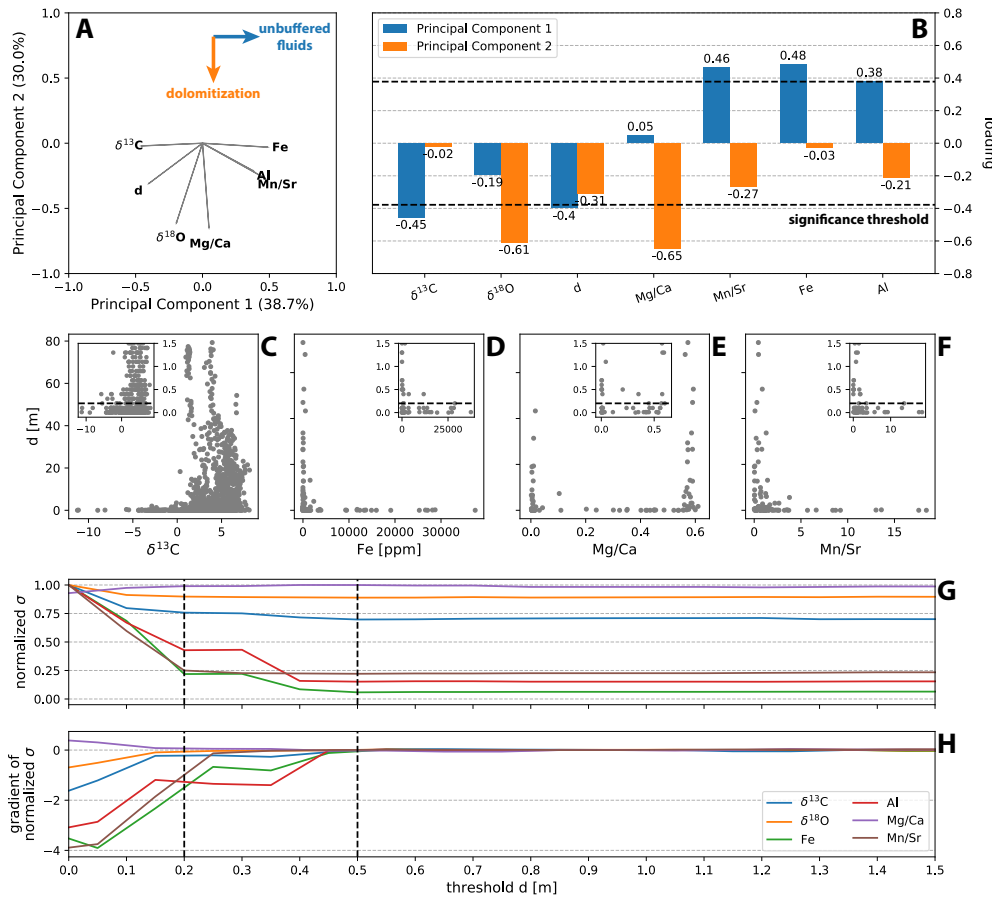


Figure 9. (A) Loadings plot from a principal components analysis (PCA) on all samples above the Islay Anomaly with element concentration data. The analysis reveals two main alteration pathways, associated with the first two principal components. $\delta^{13}\text{C}$ and d (the proximity of each carbonate sample to the closest siliciclastic unit) are anti-correlated with the first alteration pathway, which we interpret to be via ‘unbuffered (with respect to carbonate) fluids.’ (B) Histogram of loadings/eigenvalues on the first two principal components. The significance threshold is defined as $\sqrt{\frac{1}{\text{number of variables}}}$. (C-F) Scatter plots of samples above the Islay Anomaly. Inset plots have the same x-axes as their parent plots, but have y-axes zoomed in to d 0–1.5 m. The dashed line in the inset plots shows the selected d threshold of 0.2 m (see text). The variance for $\delta^{13}\text{C}$, Fe, Al, and Mn/Sr increase considerably at low d . (G) Standard deviation (σ) of the remaining data as samples below a given d (x-axis) are removed, normalized to the σ when no samples are removed (i.e. all the data). The dashed line at $d = 0.2$ m denotes where σ for $\delta^{13}\text{C}$ falls to background levels, and the dashed line at $d = 0.5$ m denotes where σ for Fe, Al, and Mn/Sr fall to background levels. (H) The corresponding gradient of G.

617 Negash Syncline and west of the Zamra Fault in the Samre Fold-Thrust Belt, where the Mariam
618 Bohkahko Formation stratigraphy is comprised of mixed siliciclastic-carbonate sedimentary rocks
619 that are dominated by siltstone (Fig. 7). In contrast, $\delta^{13}\text{C}$ variability is minimal east of the
620 Zamra Fault, where the lithofacies of the formation are dominated by carbonate, and where there
621 is a steady extended decrease from $\delta^{13}\text{C}$ values of 5 to 2‰ (Fig. 7). Given that siliciclastics do
622 not provide a carbonate buffer against altering fluids, it might be expected that carbonate
623 samples collected closer to siliciclastic horizons are less likely to preserve primary $\delta^{13}\text{C}$ and other
624 geochemical signals leading to the higher variability in $\delta^{13}\text{C}$ values observed in the siltstone-rich
625 sections.

626 To assess whether the proximity of each carbonate sample to the closest siliciclastic unit (d) is
627 a reasonable predictor of $\delta^{13}\text{C}$ alteration, we perform a principal components analysis (PCA) on
628 the samples for which we developed elemental concentration (Al, Fe, Mn, Sr, Mg, Ca) as well as
629 isotope ($\delta^{13}\text{C}$ and $\delta^{18}\text{O}$) data. A PCA simplifies the complexity in a high-dimensional dataset by
630 geometrically projecting the dataset onto principal components (or eigenvectors), each of which
631 are a linear combination of the original variables in the data set. The first principal component
632 accounts for as much of the variability in the data as possible, and each following component
633 accounts for as much of the remaining variability as possible. Ultimately, the goal of a PCA is to
634 reduce the dimensionality of the dataset by accounting for the maximum portion of variance
635 present in the dataset using as few principal components as possible. While the lithology of
636 covered intervals without exposure is not known, for determining d we make the conservative
637 assumption that covered units are recessive, fine-grained siliciclastic units. We also exclude
638 samples below and within the Islay Anomaly, so that we could eliminate the complication of
639 potentially primary fluctuations in the $\delta^{13}\text{C}$ chemostratigraphy increasing the variance in the
640 data. Element concentration data and d are log-transformed to transform these variables into
641 near-normal distributions, then all variables are centered and standardized.

642 As shown in Figure 9A and B, we interpret that the PCA reveals two main alteration pathways

643 corresponding to the first two principal components, which together explain 68.7% of the variance
644 in the dataset (see data repository for a discussion on the selection of these two components).
645 The first pathway (principal component 1) shows high positive loadings on Fe, Al, and Mn/Sr,
646 consistent with alteration via a fluid that has had significant interaction with siliciclastic units
647 prior to interacting with the carbonate samples. The second pathway (principal component 2)
648 shows high negative loadings on Mg/Ca, which is consistent with alteration via dolomitization.
649 Mg/Ca is positively correlated with $\delta^{18}\text{O}$, which suggests that dolomitization occurred early
650 during the diagenetic history of the carbonates, locking in high $\delta^{18}\text{O}$ values that were later less
651 susceptible to overprinting via warm and/or meteoric low $\delta^{18}\text{O}$ fluids due to the lower reactivity
652 of dolomites relative to limestones. Most importantly, however, the PCA reveals that $\delta^{13}\text{C}$ and d
653 are anti-correlated with the first of these alteration pathways - in other words, high Fe, Al, and
654 Mn/Sr often are associated with low $\delta^{13}\text{C}$ and small stratigraphic distance from a siliciclastic unit
655 (low d) in our carbonate samples. This result suggests that many of the low $\delta^{13}\text{C}$ values in this
656 portion of the stratigraphy where $\delta^{13}\text{C}$ values are scattered are likely a result of alteration via
657 fluids that are unbuffered with respect to carbonate (which we term ‘unbuffered fluids’) that
658 likely have interacted with low $\delta^{13}\text{C}$ organic matter during transit through siliciclastic units.
659 Whether this alteration via unbuffered fluids occurred soon or much after deposition is not
660 constrained by the PCA. At greater distances from the nearest siliciclastic unit (higher d), fluids
661 would have transited through carbonates prior to interaction with a sampled horizon, and these
662 carbonate-buffered fluids would not significantly change $\delta^{13}\text{C}$, Fe, Al, and Mn/Sr.

663 The results of the PCA are corroborated by the scatter plots shown in Figure 9C-F – at the
664 lowest distances from the closest siliciclastic unit (d), the variation in $\delta^{13}\text{C}$, Fe, Al, and Mn/Sr
665 jumps dramatically. On the other hand, Mg/Ca is bimodally distributed except at low d where
666 intermediate Mg/Ca values are observed. This result suggests that the unbuffered fluids
667 associated with this alteration pathway can cause partial dolomitization, but are not responsible
668 for the vast majority of the dolomitization in the Tambien Group.

669 To constrain the degree to which these unbuffered fluids have penetrated into the carbonate
670 horizons in the Tambien Group and potentially altered primary $\delta^{13}\text{C}$, we compute the standard
671 deviation of each of the geochemical variables as samples below a given d are removed (Fig. 9G
672 and H). The variability in $\delta^{13}\text{C}$ falls to background values at ~ 0.2 m, and for Fe, Al, and Mn/Sr
673 between ~ 0.2 and 0.5 m. These results suggest that the characteristic length scale of alteration of
674 Tambien Group carbonates by unbuffered fluids is ~ 0.5 m, with alteration of $\delta^{13}\text{C}$ being most
675 significant up to ~ 0.2 m. This difference in overprinting length scales of $\delta^{13}\text{C}$ vs. Fe, Al, and
676 Mn/Sr can be explained by the ability of carbonates to buffer against changes in C more
677 effectively than trace elements.

678 The results of filtering out samples below various values of d on the $\delta^{13}\text{C}$ composite
679 chemostratigraphy of the Tambien Group are shown in the data repository. As suggested by the
680 analysis of the standard deviations above (Fig. 9G and H), most large inconsistencies in $\delta^{13}\text{C}$ at
681 any given composite stratigraphic height are removed using the $d = 0.2$ m threshold, and
682 increasing the threshold beyond that value, in general, simply removes all data in intervals of the
683 composite chemostratigraphy where carbonate horizons are relatively thin.

684 Notably, data that resolve the Islay Anomaly as well as the descent into and recovery out of
685 the Bitter Springs Stage (but not the prolonged interval of negative values that define the Bitter
686 Springs Stage) are partially removed under the $d = 0.2$ m threshold (Fig. 3), and completely
687 removed by $d = 0.5$ m (see data repository). Furthermore, the Islay Anomaly coincides with a
688 major facies transition from siliciclastic dominated strata to carbonate dominated strata that
689 defines the Didikama-Matheos formation boundary (Fig. 8). The difference in permeability
690 associated with this facies boundary may have created a significant conduit for fluid flow at this
691 stratigraphic horizon, driving $\delta^{13}\text{C}$ to more negative values than elsewhere in the Tambien Group.
692 Together, these two observations could support an interpretation that the sharp negative $\delta^{13}\text{C}$
693 excursion at the Didikama-Matheos formation boundary does not record the Islay Anomaly and is
694 instead a product of secondary alteration. It is important to note, however, that several samples

695 within the Islay Anomaly that record $\delta^{13}\text{C}$ as low as $-5\text{\textperthousand}$, significantly below the $>0\text{\textperthousand}$ values
696 before and after the excursion, are not culled on the basis of the $d = 0.2 \text{ m}$ threshold.
697 Furthermore, it is important to consider the limitations of this $\delta^{13}\text{C}$ filter based on d . First, the
698 filter is likely not useful at d significantly beyond the characteristic length scale of alteration of
699 Tambien Group carbonates by unbuffered fluids (i.e. $\sim 0.2 \text{ m}$ for carbon) - selecting a d threshold
700 significantly above this value would arbitrarily remove $\delta^{13}\text{C}$ data that have not been altered by
701 these fluids. Second, heterogeneity in the distance to which these unbuffered fluids penetrated
702 into Tambien Group carbonates is expected. However, this method does not account for such
703 spatial heterogeneity, and so samples that fall below the threshold d may or may not have been
704 altered by the unbuffered fluids. Indeed, we find that some samples that we have high confidence
705 are recording primary $\delta^{13}\text{C}$ based on the consistency in $\delta^{13}\text{C}$ values of samples within and
706 between measured sections (e.g. samples with $\delta^{13}\text{C} \sim 5\text{\textperthousand}$ in the Mai Kenetal Formation; Fig. 3)
707 are removed using this approach. On the other hand, we can have relatively high confidence that
708 the $\delta^{13}\text{C}$ values of samples above the threshold d have not been altered by unbuffered fluids.
709 Third, this method takes the conservative approach and assumes that intervals of no outcrop
710 within measured sections are siliciclastic units. Since siliciclastic units (especially fissile siltstones,
711 which dominate the siliciclastic portions of Tambien Group stratigraphy) often are less resilient to
712 weathering than carbonates, the probability that this assumption holds is high within some
713 sections. Nevertheless, the possibility remains that some of these covered intervals are actually
714 carbonates that have been buried by colluvium.

715 There are several other observations that argue for the primary nature of the Islay Anomaly in
716 the Tambien Group. First, high precision age constraints from zircons in tuffs demonstrate that
717 this $\delta^{13}\text{C}$ excursion occurs at the same time as negative $\delta^{13}\text{C}$ values interpreted as the Islay
718 Anomaly observed in other basins around the world (Fig. 12, and ‘ $\delta^{13}\text{C}$ Excursions’). Second, the
719 Islay Anomaly is consistently reproduced across the $>100 \text{ km}$ distance between the Samre
720 Fold-Thrust Belt and Negash Syncline (Fig. 8), and wherever samples were collected across the
721 Didikama-Matheos formation boundary, a sharp $\delta^{13}\text{C}$ excursion has been observed. Third,

722 although the driver for the Islay Anomaly is poorly constrained, it is likely that a perturbation to
723 the carbon cycle of that magnitude would be associated with major environmental change and an
724 associated change in lithofacies. Fourth, the samples that record low $\delta^{13}\text{C}$ values in the Islay
725 Anomaly generally exhibit lower Fe, Al, and Mn/Sr than samples with low $\delta^{13}\text{C}$ above the Islay
726 Anomaly, suggesting that low $\delta^{13}\text{C}$ Islay Anomaly samples have been less altered by the
727 unbuffered fluids than low $\delta^{13}\text{C}$ post-Islay Anomaly samples (see data repository).

728 Given the balance of evidence for and against the primary nature of the Islay Anomaly, and
729 given the inherent limitations of the $\delta^{13}\text{C}$ filter based on d , we interpret the excursion to be a
730 primary feature of the record. If these carbonates have been altered by unbuffered fluids, the
731 effect may have been to ‘deepen’ the excursion, rather than creating it from an otherwise stable
732 $\delta^{13}\text{C}$ chemostratigraphy. We find that the primary utility of the filter as described here is to
733 assess which $\delta^{13}\text{C}$ values are primary in intervals of the stratigraphy where time-equivalent
734 carbonates produce inconsistent results (e.g. in the Mariam Bohkahko Formation). Nevertheless,
735 we acknowledge the possibility that the sharp negative $\delta^{13}\text{C}$ excursion at the Didikama-Matheos
736 formation boundary is instead a product of secondary alteration.

737 Isotope Conglomerate Test

738 We perform an isotope conglomerate test on carbonate clasts within the diamictite of the Negash
739 Formation of both the Negash Syncline ($n = 17$) and the Samre Fold-Thrust Belt ($n = 61$) (Fig.
740 10). In such a test, carbonate clasts are sampled to test whether carbon and oxygen isotopes
741 within the clasts were reset to similar $\delta^{13}\text{C}$ and $\delta^{18}\text{O}$ values through either meteoric or burial
742 diagenesis (Husson et al., 2012, 2015). If the clasts show substantial variability in their isotopic
743 composition, we infer that their isotopic values were acquired prior to deposition in the clastic
744 unit and were not fully reset through burial diagenesis.

745 The isotope conglomerate test in the Negash Syncline reveals a $\sim 7\text{\textperthousand}$ range in $\delta^{13}\text{C}$ values,
746 and in the Samre Fold-Thrust Belt there is a slightly greater range of $\sim 10\text{\textperthousand}$. These values are

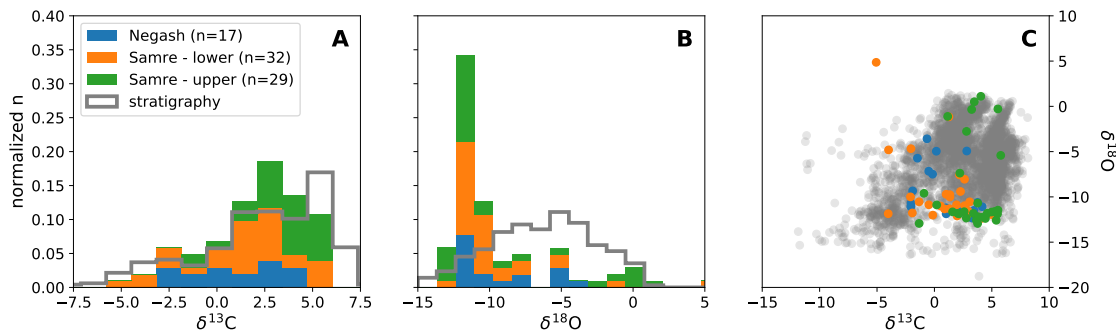


Figure 10. (A) and (B) Histograms of $\delta^{13}\text{C}$ and $\delta^{18}\text{O}$ values of carbonate clasts within the diamictite of the Negash Formation from the Negash Syncline and Samre Fold-Thrust Belt. Clasts from the Negash Syncline ($n = 17$) were sampled from a single horizon. Clasts from the Samre Fold-Thrust Belt ($n = 61$) were sampled from two horizons (lower and upper) ~ 100 m stratigraphically apart. (C) Cross plot of $\delta^{13}\text{C}$ vs $\delta^{18}\text{O}$ values of the carbonate clasts. In all panels, grey data represent all carbonate samples taken from below the diamictite in the Tambien Group (i.e. from the *in situ* stratigraphy).

747 consistent with the carbonate clasts being sourced from the underlying stratigraphy (Fig. 10).
 748 However, the $\delta^{18}\text{O}$ values of the clasts in both areas cluster at $\sim 12\text{\textperthousand}$, which may indicate that
 749 the $\delta^{18}\text{O}$ values of the clasts, unlike the $\delta^{13}\text{C}$ values, largely were reset after the deposition of the
 750 Negash Formation. However, the $\delta^{13}\text{C}$ and $\delta^{18}\text{O}$ of the clasts do not appear to be correlated,
 751 which supports the interpretation that the clasts preserve near primary $\delta^{13}\text{C}$ even for clasts where
 752 the $\delta^{18}\text{O}$ was altered. This indication of preferential preservation of primary $\delta^{13}\text{C}$ over $\delta^{18}\text{O}$ is
 753 consistent with carbon being more rock-buffered against altering fluids than oxygen.

754 Sr Isotopes

755 Relative to C isotopes, Sr isotopes in carbonates are more vulnerable to secondary alteration (e.g.
 756 Banner and Hanson, 1990). Trace element geochemistry can be used to assess the degree of such
 757 alteration. Mn/Sr values are a commonly-used indicator of alteration, since interaction with
 758 secondary fluids tend to increase [Mn] and decrease [Sr] (Brand and Veizer, 1980; Banner and
 759 Hanson, 1990; Jacobsen and Kaufman, 1999). Furthermore, low [Sr] makes $^{87}\text{Sr}/^{86}\text{Sr}$ more
 760 susceptible to overprinting since less exchange is required to alter the original strontium isotopic

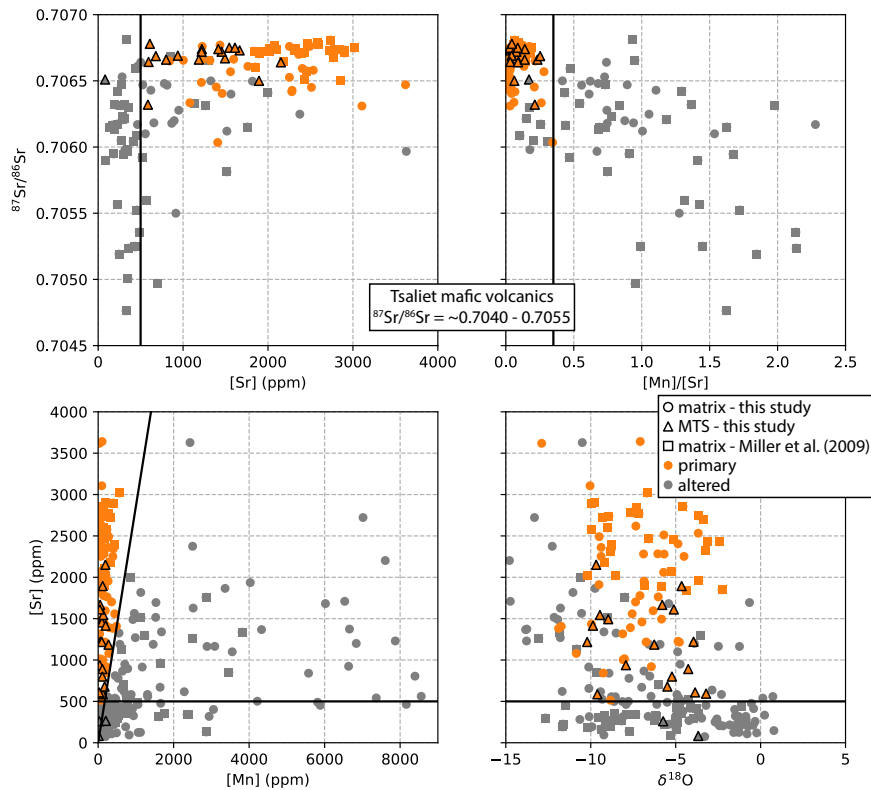


Figure 11. Cross plots of [Sr] and Mn/Sr against $^{87}\text{Sr}/^{86}\text{Sr}$, and [Mn] and $\delta^{18}\text{O}$ against [Sr] for data presented in this study and Miller et al. (2009). Black lines illustrate the thresholds used to interpret primary versus altered $^{87}\text{Sr}/^{86}\text{Sr}$ ($[\text{Sr}] > 500 \text{ ppm}$ and $\text{Mn/Sr} < 0.35$). MTS = molar tooth structure.

ratio (Brand and Veizer, 1980; Veizer, 1989; Banner and Hanson, 1990). As in other studies (e.g. Halverson et al., 2007a), we apply a filter based on minimum [Sr] and maximum Mn/Sr in order to exclude $^{87}\text{Sr}/^{86}\text{Sr}$ values from samples that are more likely to be altered. To select appropriate [Sr] and Mn/Sr thresholds for our samples, we exploited the presence of molar tooth structures in the Tambien Group, since these structures consist of high purity calcite and are more likely to record primary geochemical signals relative to the surrounding micrite due to a lack of Rb-containing clay and more limited recrystallization (Fig. 4). Given that all molar tooth structure samples cluster at $\text{Mn/Sr} < 0.35$, and all molar tooth structure samples except one have $[\text{Sr}] > 500 \text{ ppm}$, these values are used as filtering thresholds to generate a record that is more likely to be reflective of primary $^{87}\text{Sr}/^{86}\text{Sr}$ (Fig. 11). We find that the $\delta^{13}\text{C}$ and $^{87}\text{Sr}/^{86}\text{Sr}$ values from

771 molar tooth structures are similar to that of immediately adjacent micrite that pass the elemental
772 thresholds (see data repository). This similarity suggests that micritic samples from the Tambien
773 Group (provided that they pass the elemental thresholds set above) also are capable of preserving
774 primary geochemical signals, and supports their use alongside calcite from molar tooth structures
775 in reconstructing Tonian marine $^{87}\text{Sr}/^{86}\text{Sr}$.

776 Fluid-rock geochemical models generally predict that overprinting results in a sharp increase in
777 $^{87}\text{Sr}/^{86}\text{Sr}$ below a threshold [Sr] (Banner and Hanson, 1990; Jacobsen and Kaufman, 1999). These
778 models assume that the altering fluid has high $^{87}\text{Sr}/^{86}\text{Sr}$ resulting from interaction with
779 radiogenic rocks with high $^{87}\text{Sr}/^{86}\text{Sr}$ prior to interacting with the carbonates. However, as
780 suggested by Miller et al. (2009), the altering fluids that are responsible for overprinting in the
781 Tambien Group plausibly had significant interaction with juvenile arc volcanics and
782 volcaniclastics with low $^{87}\text{Sr}/^{86}\text{Sr}$ before interacting with the carbonates, since the Tambien
783 Group was deposited atop of the arc volcanics and volcaniclastics of the Tsaliet Group. Two
784 samples of mafic volcanics of the Tsaliet Group in the proximity of the Tsedia Syncline have
785 $^{87}\text{Sr}/^{86}\text{Sr}$ values of 0.704047 and 0.705406, which confirms these expected low values. As a result,
786 we do not expect to see a sharp increase in $^{87}\text{Sr}/^{86}\text{Sr}$ below the threshold [Sr]. Instead, we expect
787 to see a decrease in $^{87}\text{Sr}/^{86}\text{Sr}$ at low [Sr] due to the altering fluid containing Sr sourced from
788 juvenile arc material. This latter relationship is observed in the data (Fig. 11). Note that the
789 majority of the low [Sr] and high Mn/Sr samples that have low (and excluded) $^{87}\text{Sr}/^{86}\text{Sr}$ values
790 come from Miller et al. (2009); many of the data developed in this study are from samples that
791 were screened for [Sr] and Mn/Sr prior to $^{87}\text{Sr}/^{86}\text{Sr}$ analysis.

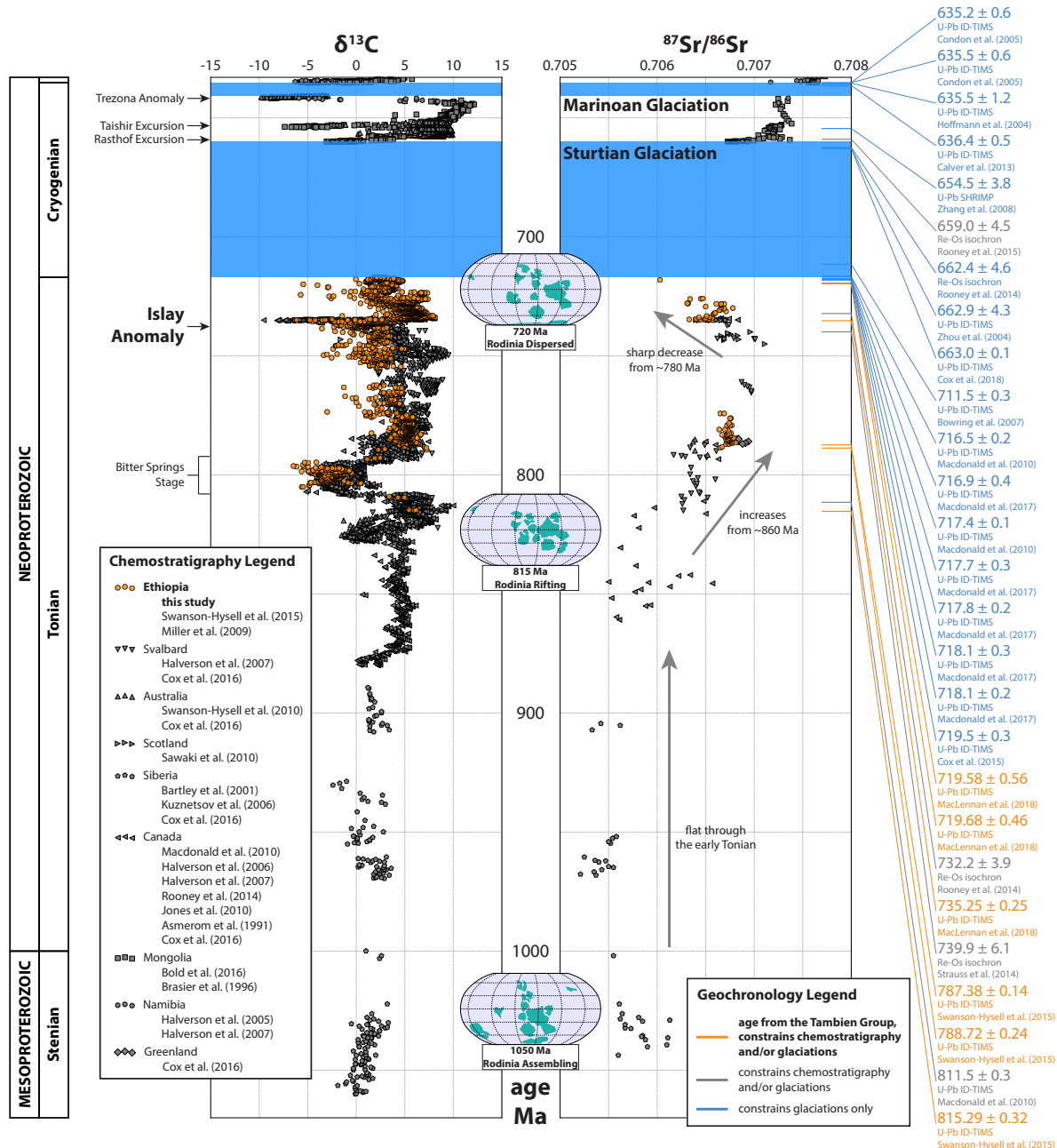


Figure 12. Tonian-Cryogenian $\delta^{13}\text{C}$ and $^{87}\text{Sr}/^{86}\text{Sr}$ chemostratigraphic composite. Construction of this composite is discussed in the ‘Tonian-Cryogenian Chemostratigraphic Composite’ section. The paleogeographic reconstructions are included to illustrate the approximate geometry of Rodinia (assembled vs. dispersed) through the Tonian.

792 **TONIAN-CRYOGENIAN CHEMOSTRATIGRAPHIC
793 COMPOSITE**

794 Combined with U-Pb ID-TIMS dates on zircons from Swanson-Hysell et al. (2015) (815.29 ± 0.32 ,
795 788.72 ± 0.24 , and 787.38 ± 0.14 Ma), MacLennan et al. (2018) (735.25 ± 0.25 , 719.58 ± 0.56 , and
796 719.68 ± 0.46 Ma), and this study (Table 1), $\delta^{13}\text{C}$ and $^{87}\text{Sr}/^{86}\text{Sr}$ data from the Tambien Group
797 (Miller et al., 2009; Swanson-Hysell et al., 2015; this study) now comprise the most temporally
798 well-constrained pre-Sturtian chemostratigraphic dataset to date. These data are combined with
799 other chemostratigraphic and geochronologic datasets from Neoproterozoic sedimentary rocks in
800 other localities around the world to generate a composite Tonian chemostratigraphy (Fig. 12).
801 We use the Tambien Group $\delta^{13}\text{C}$ curve as the backbone for making correlations with other
802 datasets. Tonian $\delta^{13}\text{C}$ and $^{87}\text{Sr}/^{86}\text{Sr}$ data within the composite come from the Akademikerbreen
803 Group of Svalbard (Halverson et al., 2007a,b), the Eleanore Bay Supergroup of East Greenland
804 (Cox et al., 2016), the Bitter Springs Group of Australia (Swanson-Hysell et al., 2010; Cox et al.,
805 2016), the Fifteenmile Group of Canada (Macdonald et al., 2010; Cox et al., 2016), the Little Dal
806 Group of Canada (Halverson, 2006; Halverson et al., 2007a), the Coates Lake Group of Canada
807 (Halverson, 2006; Halverson et al., 2007a; Rooney et al., 2014), the Shaler Supergroup of Canada
808 (Asmerom et al., 1991; Jones et al., 2010), the Dalradian Supergroup of Scotland (Sawaki et al.,
809 2010), Proterozoic carbonates of the UchurMaya and Turukhansk regions of Siberia (Bartley
810 et al., 2001; Cox et al., 2016), and the Karatau Group of the Urals (Kuznetsov et al., 2006; Cox
811 et al., 2016). Cryogenian $\delta^{13}\text{C}$ and $^{87}\text{Sr}/^{86}\text{Sr}$ data within the composite come from the
812 Tsagaan-Olam Group of Mongolia (Brasier et al., 1996; Bold et al., 2016), the Hay Creek Group
813 of Canada (Rooney et al., 2014), the Adelaide Rift Complex of Australia (Swanson-Hysell et al.,
814 2010; Rose et al., 2012), and the Otavi Group of Namibia (Halverson et al., 2005, 2007a).

815 Correlations between datasets are made using absolute age constraints where possible -
816 otherwise, the characteristic negative $\delta^{13}\text{C}$ anomalies of the ca. 800 Ma Bitter Springs Stage and
817 the ca. 735 Ma Islay Anomaly are used to align datasets. The same criteria for assessing altered

818 $^{87}\text{Sr}/^{86}\text{Sr}$ values that were used in the original publications are applied here, unless our analysis of
819 $^{87}\text{Sr}/^{86}\text{Sr}$ vs. [Sr] and $^{87}\text{Sr}/^{86}\text{Sr}$ vs. Mn/Sr suggested a different criteria for alteration. However,
820 even when different criteria are applied for a particular dataset, the resulting $^{87}\text{Sr}/^{86}\text{Sr}$ curve was
821 similar to that presented in the original study with little difference for the large-scale $^{87}\text{Sr}/^{86}\text{Sr}$
822 trends through the Tonian. The details of the methodology, details regarding the compiled data,
823 and a link to the Python code used to develop the Tonian-Cryogenian chemostratigraphic
824 composite are included in the data repository.

825 **DISCUSSION**

826 **$\delta^{13}\text{C}$ Excursions**

827 The mechanism behind the exceptionally large negative $\delta^{13}\text{C}$ excursions in the Neoproterozoic,
828 such as the Islay and Trezona anomalies, remains a mystery. Proposed mechanisms for the
829 excursions include: a decrease in the ratio of organic to inorganic carbon burial resulting from
830 colder conditions suppressing organic productivity (Kaufman et al., 1997; Hoffman et al., 1998),
831 oxidation of a large dissolved organic carbon pool (Rothman et al., 2003), enhanced export of
832 organic matter from the upper ocean into anoxic deep water where dissolved and particulate
833 organic carbon is remineralized (Tziperman et al., 2011), precipitation of authigenic carbonate
834 during early diagenesis (Schrag et al., 2013), interactions of hydrocarbon-influenced fluids with
835 carbonates during diagenesis (Derry, 2010), and meteoric diagenesis in response to sea level fall
836 (Swart and Kennedy, 2012). Some of these proposed mechanisms for large negative $\delta^{13}\text{C}$
837 excursions imply that the excursions are global in nature, and therefore synchronous between
838 basins, while others imply local processes that would not necessarily lead to the excursions being
839 recorded in the same age rocks between basins (but see Swart, 2008). Furthermore, some of these
840 proposed mechanisms draw connections between large negative $\delta^{13}\text{C}$ excursions and the onset of
841 glaciation.

842 Data from the Tambien Group add new constraints to this debate. A volcanic tuff (sample
843 T46-102.2Z) adjacent to carbonates with $\delta^{13}\text{C} = \sim 0\text{\textperthousand}$ was identified ~ 4 m above the $\sim -12\text{\textperthousand}$
844 nadir of the large negative $\delta^{13}\text{C}$ excursion near the Didikama-Matheos formation boundary (Fig.
845 8). Zircons from this tuff yield a weighted mean age of 735.25 ± 0.88 Ma (including all external
846 uncertainties) using U-Pb ID-TIMS (MacLennan et al., 2018). This age is consistent with
847 geochronological constraints from within the Islay Anomaly in the Windermere Supergroup of
848 northwest Canada: Rooney et al. (2014) obtained a Re-Os age of 732.2 ± 3.9 Ma (including all
849 external uncertainties) from black shales adjacent to carbonates with $\delta^{13}\text{C} = \sim 0\text{\textperthousand}$ and ~ 200 m
850 above the nadir of the excursion, and Strauss et al. (2014) obtained a Re-Os age of 739.9 ± 6.1 Ma
851 (including all external uncertainties) from black shales adjacent to carbonates with $\delta^{13}\text{C} = \sim -4\text{\textperthousand}$
852 and ~ 5 m below the nadir of the excursion. Together, these three dates suggest that this
853 excursion within the Tambien Group is indeed the same anomaly as that in the Windermere
854 Supergroup. Furthermore, although no direct reliable age constraints have been developed, sharp
855 negative $\delta^{13}\text{C}$ excursions interpreted to be the Islay Anomaly also have been observed in the
856 Dalradian Supergroup of Scotland (Sawaki et al., 2010), the Akademikerbreen Group of northeast
857 Svalbard (Halverson et al., 2007b; Hoffman et al., 2012), and the Windermere Supergroup (Coates
858 Lake Group) of northwest Canada (Halverson, 2006). Together, these data suggest that the Islay
859 Anomaly is synchronous in at least two separate basins, likely is synchronous globally, and
860 precedes the Sturtian Glaciation by ~ 18 Myr (MacLennan et al., 2018).

861 Tonian stratigraphic sequences typically either do not host carbonates in the interval
862 immediately preceding the onset of the Sturtian Glaciation, or have missing time associated with
863 an unconformity. Carbonate stratigraphy from northwest Canada (Halverson, 2006; Macdonald
864 et al., 2010; Rooney et al., 2014), Scotland (Sawaki et al., 2010), and northeast Svalbard
865 (Halverson et al., 2007b) all end at or soon after the ca. 735 Ma Islay Anomaly (Fig. 12). The
866 Coppercap Formation of the Coates Lake Group of northwest Canada is the only succession
867 reported in the literature that preserves carbonate stratigraphy with a record after the nadir of
868 the Islay Anomaly to $\delta^{13}\text{C}$ values $> 5\text{\textperthousand}$ (Halverson, 2006; Rooney et al., 2014). If the duration of

869 the Islay Anomaly (from the initiation of the downturn in $\delta^{13}\text{C}$ values through to the full
870 recovery) is ~ 1 Myr (MacLennan et al., 2018) and sediment accumulation rates in the Coates
871 Lake Group are constant, the top of this succession would have an age > 730 Ma. In contrast, the
872 Tambien Group has a more complete stratigraphic record in the lead-up to Sturtian glacial
873 deposits. Zircons in volcanic tuffs 73.6 and 85.3 m below the base of the Negash Formation yield
874 U-Pb ID-TIMS ages of 719.68 ± 0.46 and 719.58 ± 0.56 Ma respectively (Fig. 7) leading to an age
875 estimate between 718.0 and 716.4 Ma for the onset of the diamictite (MacLennan et al., 2018).
876 These geochronological constraints demonstrate that carbonate stratigraphy from the Tambien
877 Group continues well past the ca. 735 Ma Islay Anomaly until at least ca. 719.6 Ma - at most
878 only a few million years before the onset of Sturtian Glaciation. Therefore, the Tambien Group
879 preserves the most complete pre-Sturtian carbonate stratigraphy studied to date, and shows that
880 $\delta^{13}\text{C}$ values are sustained at $\sim 5\text{\textperthousand}$ following the recovery from the Islay Anomaly, then remain at
881 positive values with a progressive decrease to values of $\sim 2\text{\textperthousand}$ throughout the
882 carbonate-dominated sections of the Mariam Bohkahko Formation up to the contact with the
883 Negash Formation (Fig. 7). These data indicate that no large negative $\delta^{13}\text{C}$ excursion was
884 associated with the onset of the Sturtian Glaciation.

885 Other sharp high-amplitude Neoproterozoic $\delta^{13}\text{C}$ excursions also have been interpreted to be
886 global signals that are temporally disconnected from low-latitude glaciation, such as the
887 Cryogenian inter-glacial Taishir Excursion (Fig. 12; Bold et al., 2016) and the Ediacaran
888 Shuram-Wonoka Excursion (Husson et al., 2015). Together, these conclusions imply that
889 proposed mechanisms to explain at least some of these sharp high-amplitude $\delta^{13}\text{C}$ excursions: 1)
890 do not have to be consistent with low pCO₂ and the onset of low-latitude glaciation; and 2)
891 should have the capacity to explain synchronicity in at least a number of basins around the world.

892 Onset of the Sturtian Snowball

893 Energy balance models of Snowball Earth initiation propose that, once ice sheets reach $\sim 30^\circ$
894 latitude, the ice-albedo positive feedback overwhelms negative feedbacks on temperature, causing
895 Earth's surface temperature to plummet and ice to advance to the equator on the timescale of less
896 than a few thousand years (Baum and Crowley, 2001; Hoffman and Schrag, 2002; Pollard and
897 Kasting, 2005). In other words, energy balance models predict that, at the resolution of U-Pb
898 ID-TIMS dating, all low-latitude areas were covered by ice at the same time. While this
899 hypothesis is consistent with climate models of varying complexity, a direct field test for the
900 synchronous onset of any of the Snowball Earths has not been made. In order to perform such a
901 test, a study would require high precision ages from as close as possible to the onset of glacigenic
902 deposits in as many different basins as possible. However, despite the fact that glacigenic deposits
903 associated with the Sturtian Snowball Earth have been identified in numerous basins around the
904 world (Hoffman and Li, 2009), very few of these basins have direct geochronological data that
905 precisely constrains the onset of the glacigenic deposits in their respective basins.

906 Prior to data from the Tambien Group, the best age constraints on the start of the Sturtian
907 Glaciation came from northwest Canada where U-Pb ID-TIMS on zircon from a volcanic tuff
908 within glacial diamictite and from a rhyolite underlying this diamictite yielded weighted mean
909 ages of 716.47 ± 0.24 and 717.43 ± 0.14 Ma respectively (Macdonald et al., 2010). Given that thick
910 volcanic units have the potential to obscure sedimentary evidence of glaciation, the
911 717.43 ± 0.14 Ma age from rhyolite cannot be interpreted to be pre-glacial in this basin without
912 ambiguity. Age constraints for the onset of Sturtian glacigenic deposits also come from other
913 basins around the world, but provide looser constraints than the dates from northwest Canada.
914 U-Pb ID-TIMS on detrital zircons from a volcaniclastic unit underlying Sturtian diamictite in
915 Arctic Alaska yielded a maximum depositional age of 719.47 ± 0.29 Ma (Cox et al., 2015). These
916 data cannot rule out that the onset of continental ice in Arctic Alaska significantly post-dated
917 719.47 ± 0.29 Ma, especially since an unconformity separates the volcaniclastic unit from the

918 diamictite. U-Pb ID-TIMS on zircons from a tuffaceous graywacke within a Sturtian diamictite in
919 Oman yielded an age of 711.52 ± 0.31 Ma (Brasier et al., 2000; Bowring et al., 2007). This
920 minimum age constraint on the onset of continental ice in Oman is consistent with the data from
921 northwest Canada, but is too young to reliably test the rapid onset of low-latitude glaciation.
922 U-Pb SIMS dates on zircons from tuffaceous slates underlying Sturtian diamictite in south China
923 yielded ages of 715.9 ± 2.8 and 716.1 ± 3.4 Ma, also consistent with dates from northwest Canada.
924 However, zircons from these tuffaceous slates range in age from 705 to 827 Ma (Lan et al., 2014)
925 with large uncertainty on individual dates, and the *in situ* methods used on these samples do not
926 chemically abrade the zircon prior to analysis, which combined with lower precision makes it
927 difficult to identify Pb-loss compared to dates developed using ID-TIMS.

928 The estimated age of the base of the glacial deposits in the Tambien Group (between 718.0
929 and 716.4 Ma at the 95% confidence level; MacLennan et al., 2018) is too imprecise to conclude
930 that low-latitude glaciation was as globally synchronous as energy balance models predict.
931 Nevertheless, this result is consistent with synchronous onset of deposition of the Negash
932 Formation and the glacigenic deposits in northwest Canada. Furthermore, in the Samre
933 Fold-Thrust Belt, carbonates of the Mariam Bohkahko Formation often are found adjacent to
934 diamictite of the Negash Formation. West of the Zamra Fault in the Samre Fold-Thrust Belt
935 (Fig. 2), a 60 cm thick grainstone bed was identified 40 cm below the base of the diamictite.
936 Below this bed, grainstone and oolite beds are interbedded with siltstone at the meter scale. East
937 of the fault, stromatolites atop hundreds of metres of carbonates are found directly in contact
938 with the Negash Formation (Fig. 7). Given that marine carbonates, especially stromatolites,
939 typically form in warm tropical conditions, this juxtaposition of lithofacies lends further support
940 to the hypothesis of rapid cooling immediately prior to the glaciation and sudden advance of ice
941 toward the equator.

942 Pre-Sturtian $^{87}\text{Sr}/^{86}\text{Sr}$ and the Drivers of Planetary Cooling

943 One of the most prominent proposed mechanisms for the initiation of the Sturtian Snowball
944 Earth argues that the emplacement of large igneous provinces (LIPs) at low latitudes contributed
945 to the onset of the snowball climate state by enhancing planetary weatherability, leading to a
946 lower atmospheric CO₂ concentration (the ‘Fire and Ice’ hypothesis, first articulated in Goddériss
947 et al., 2003). This hypothesis continues to be seen as viable (e.g. Cox et al., 2016) given the high
948 weathering rates of basalt as well as the high concentrations of Ca and Mg in mafic lithologies
949 that are liberated through chemical weathering and ultimately sequester carbon through
950 carbonate precipitation (Dessert et al., 2001). Proponents of the hypothesis point to an apparent
951 increase in the area and frequency of continental flood basalts from ca. 860 Ma onward (Cox
952 et al., 2016), culminating in the eruption of the $2.225 \times 10^6 \text{ km}^2$ Franklin LIP (Ernst et al., 2008)
953 around the time of Sturtian Glaciation initiation. At this time, paleogeographic reconstructions
954 (e.g. Li et al., 2008) place the Franklin LIP at low latitudes where chemical weathering rates are
955 expected to be highest due to relatively high temperatures and runoff rates. We assess these
956 arguments below through the lens of the temporally calibrated composite $^{87}\text{Sr}/^{86}\text{Sr}$ curve.

957 The strontium isotopic composition of the oceans is sensitive to the relative weathering flux
958 from different lithologies, and thus provides a record that could give insight into the ‘Fire and Ice’
959 hypothesis. Sr enters the ocean from a number of distinct sources: weathering of continental
960 lithologies, hydrothermal interaction with mid-ocean ridges, and weathering of island arcs and
961 oceanic island basalts (Richter et al., 1992). Continental lithologies can be divided into the broad
962 categories of limestones, juvenile igneous rocks (such as basalt), and older cratonic rocks (such as
963 gneiss and granite). Importantly, each of these lithologies have different weatherabilities, Sr
964 concentrations, and Sr isotopic compositions (Allègre et al., 2010). In particular, juvenile volcanic
965 lithologies have relatively low $^{87}\text{Sr}/^{86}\text{Sr}$ and are readily weathered, whereas older cratonic
966 lithologies have relatively high $^{87}\text{Sr}/^{86}\text{Sr}$ and are less readily weathered (Dessert et al., 2003). The
967 higher $^{87}\text{Sr}/^{86}\text{Sr}$ in cratonic lithologies arises as a result of higher concentrations of Rb in

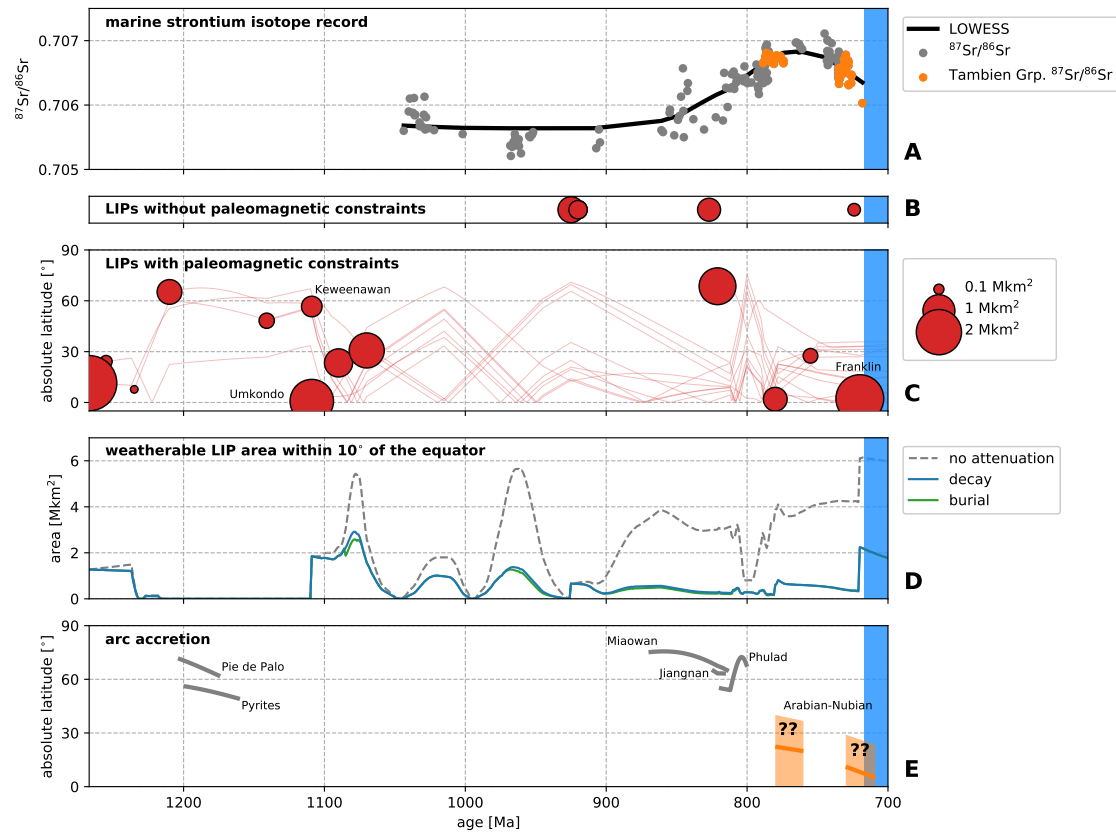


Figure 13. (A) Composite $87\text{Sr}/86\text{Sr}$ (as developed in the ‘Tonian-Cryogenian Chemostratigraphic Composite’ section). The black line is a locally weighted scatterplot smoothing (LOWESS) line - using 45% of the data when estimating each y-value resulted in a line that neither over- nor under-represented major trends in the $87\text{Sr}/86\text{Sr}$ data. (B) Emplacement timing and area of LIPs (adapted from Ernst and Youbi, 2017) without paleomagnetic constraints. (C) Emplacement timing, area, and latitude of LIPs (adapted from Ernst and Youbi, 2017) with paleomagnetic constraints (see data repository). The lines represent the tracks of the centroids of each LIP after emplacement, obtained from a paleogeographic model (Swanson-Hysell et al., 2018) which incorporates a pair of true polar wander events ca. 810 and 790 Ma (Maloof et al., 2010; Swanson-Hysell et al., 2012). (D) Weatherable LIP area within 10° of the equator. The three lines represent three different treatments of LIPs after emplacement (see text for further details). (E) Centroids of arc accretion events. The paleolatitude of the Arabian-Nubian accretion events are poorly constrained. The shaded orange region represents the approximate range of latitudes that Arabian-Nubian arc accretion could have occurred at, based on the paleolatitude of India and the African cratons. The orange line represents a single model position for Arabian-Nubian arc accretion that is consistent with existing constraints (see text for further details). In all panels, the blue bar represents the Sturtian Glaciation.

differentiated crust where ^{87}Rb decays to ^{87}Sr . ^{87}Sr also is able to accumulate for a long time in ancient cratonic rocks. Sr leaves the ocean primarily through the formation of carbonate minerals (aragonite/calcite/dolomite), which record the $^{87}\text{Sr}/^{86}\text{Sr}$ of ocean water at the time of formation (Brand, 2004). The Sr isotopic composition of the ocean is effectively homogenous at any given time, since the residence time of strontium in the oceans ($\sim 3\text{-}5$ Myr) is much longer than the mixing time of the ocean (~ 1000 yr) (Broecker and Peng, 1982). Thus, the $^{87}\text{Sr}/^{86}\text{Sr}$ of the oceans, and therefore unaltered marine carbonates, commonly is interpreted as a proxy for the relative globally averaged fluxes coming from each of the four sources (subaerial weathering of continental limestone, subaerial weathering of continental radiogenic lithologies, subaerial weathering of continental and oceanic juvenile lithologies, and hydrothermal interaction with mid-ocean ridges) at any given point in time. Therefore, if there was a large increase in the weathering of juvenile material associated with low-latitude LIP emplacement immediately prior to the Sturtian Snowball Earth as the ‘Fire and Ice’ hypothesis argues, the $^{87}\text{Sr}/^{86}\text{Sr}$ of the oceans is expected to respond by significantly decreasing.

The global composite Tonian $^{87}\text{Sr}/^{86}\text{Sr}$ curve is flat at low values of ~ 0.7055 until ca. 860 Ma when there is an increase up to $^{87}\text{Sr}/^{86}\text{Sr}$ values of ~ 0.7070 by ca. 770 Ma (Figs. 12 and 13). There is a subsequent decrease back down to values of ~ 0.7060 leading up to the initiation of the Sturtian Glaciation ca. 717 Ma. This decrease in $^{87}\text{Sr}/^{86}\text{Sr}$ interrupts the otherwise increasing $^{87}\text{Sr}/^{86}\text{Sr}$ values from ca. 880 Ma onwards that culminated in values ~ 0.7090 by 600 Ma (Halverson et al., 2007b). In Figure 13, this $^{87}\text{Sr}/^{86}\text{Sr}$ curve is plotted along with the emplacement timing, area, and latitude of LIPs in order to evaluate proposed connections between the two. Estimates of original emplacement extents are adapted from Ernst and Youbi (2017), which were drawn to include the full surface extent of all dykes, sills, and volcanics interpreted to be associated with each LIP. The movements of LIPs after emplacement are determined using a paleogeographic model that incorporates available paleomagnetic constraints (Swanson-Hysell et al., 2018). In addition to paleolatitude, the post-emplacement tectonic and erosional history of each LIP is important for considering the effect that a LIP will have on

995 planetary weatherability. For example, without active uplift, soil shielding from regolith
996 development on low-relief LIPs could significantly decrease the local weatherability of a LIP
997 (Gabet and Mudd, 2009; Hartmann et al., 2014; Goddéris et al., 2017a). Furthermore, the
998 thickness of this regolith is dependent on the local climate (Norton et al., 2014). Ultimately, all
999 LIPs will cease weathering at some point, either through burial or complete erosion. We construct
1000 simplified post-emplacement models for LIPs and plot how these scenarios impact the total
1001 weatherable area of LIPs within the tropics in Figure 13D. We define the tropics to be within 10°
1002 of the equator based on the modern zonal-average distributions of temperature and precipitation,
1003 which appear to have been stable through time (Evans, 2006). In the ‘no attenuation’ model,
1004 weatherable LIP areas are held constant from the time of emplacement (i.e. no post-emplacement
1005 processes are accounted for). This model is intended as an end-member reference as LIPs do not
1006 persist indefinitely for the reasons described above. In the ‘decay’ model, the weatherable area of
1007 each LIP undergoes exponential decay from the time of emplacement, with a half-life of 100 Myr.
1008 This model follows the approach of Goddéris et al. (2017b) and the implemented half-life is within
1009 the range of observed values for younger, better-constrained LIPs. The ‘burial’ model is identical
1010 to the ‘decay’ model, except that we account for burial of the ca. 1109 Ma Keweenawan LIP at
1011 ca. 1085 Ma by removing it from the model at that time, given that this region thermally
1012 subsided and the volcanics were buried by sediment at that time (White, 1997; Ojakangas et al.,
1013 2001; Swanson-Hysell et al., 2018). We note that accounting for the burial of the Keweenawan
1014 LIP in the ‘burial’ model does not significantly affect the area of weatherable LIPs in the tropics
1015 in our post-emplacement models since the LIP has a relatively small area confined to a
1016 continental rift. It is important to note that, while broadly representative, these three models are
1017 an oversimplification of the true post-emplacement histories for several reasons. For instance, all
1018 LIPs (with the exception of the Keweenawan LIP) are treated identically, when instead they may
1019 have experienced very different tectonic histories that could result in very different weathering
1020 histories. Furthermore, global and local climate would have been sensitive to the paleogeography
1021 and paleotopography at any given time step, which together may have created different

1022 temperature and runoff conditions at each LIP. For example, the topography of the
1023 Himalaya-Tibetan plateau is linked to the Asian monsoons, which introduces significantly higher
1024 precipitation in affected areas compared to the zonal average for that latitude (Zhisheng et al.,
1025 2001). Nevertheless, the ‘decay’ and ‘burial’ models are likely much closer to the true
1026 post-emplacement histories and associated LIP area in the tropics than the ‘no attenuation’
1027 model.

1028 Between ca. 1270 and 1110 Ma, LIP emplacement is relatively frequent (Fig. 13C). However,
1029 these LIPs are either emplaced at mid- to high latitudes, or drift there soon after emplacement,
1030 resulting in a minimal area within the tropics (Fig. 13D). At ca. 1110 Ma, the Umkondo LIP
1031 (Kalahari craton) is emplaced at low latitudes, followed closely by the Keweenawan (Laurentia
1032 craton), SW Laurentia, and Warakurna (Australia craton) LIPs at mid-latitudes, leading to a
1033 significant increase in LIP area within the tropics (Fig. 13D). After the emplacement of these four
1034 LIPs, there are no identified LIP emplacement events over the next ~150 Myr until ca. 920 Ma,
1035 but several Mesoproterozoic LIPs drift through the tropics during this time. As described above,
1036 it is unclear whether each of these LIPs were still exposed well enough to contribute to global
1037 weatherability by the time they drifted through the tropics, but, if the post-emplacement models
1038 (Fig. 13D) reasonably approximate the effect of the true post-emplacement histories, then
1039 relatively large areas of weatherable LIPs pass through the tropics between ca. 1100 and 920 Ma.
1040 The weathering of these LIPs in the tropics could lead to a relatively high contribution to the
1041 global weathering flux coming from juvenile rocks passing through the warm and wet tropics and
1042 provide an explanation for the low $^{87}\text{Sr}/^{86}\text{Sr}$ values observed throughout this period (Fig. 13A).
1043 The Dashigou (North China craton) and Gangil-Mayumbia (Congo craton) LIPs are next
1044 emplaced ca. 920 Ma (Fig. 13B). However, no direct paleomagnetic constraints exist for these two
1045 LIPs, and their paleolatitudes at the time of emplacement are uncertain. In the paleogeographic
1046 model, the Gangil-Mayumbia LIP is at low latitudes at the time of emplacement, but this
1047 position is poorly constrained. Nevertheless, given its relatively small area, its contribution to
1048 global weatherability is likely to be small, even if emplaced within the tropics. Between ca. 880

and 780 Ma, Mesoproterozoic LIPs continue to transit through the tropics. However, our post-emplacement models predict that the weatherable area of these $>\sim 200$ Myr old LIPs has decayed to small values by this time, which would make them ineffective at contributing to the global weathering flux despite being in the tropics. These models therefore are consistent with a decreasing relative contribution of juvenile rocks to the global weathering flux, driving $^{87}\text{Sr}/^{86}\text{Sr}$ to higher values as is observed over this period. Notably, the large SWCUC LIP (South China craton) is emplaced at high, rather than low, latitudes at ca. 820 Ma during this interval of increasing $^{87}\text{Sr}/^{86}\text{Sr}$ ca. 880-770 Ma. The Willouran-Gairdner LIP (Australia craton) also is emplaced ca. 830 Ma, and although robust paleomagnetic constraints do not exist for this LIP, our paleogeographic model places it at mid-latitudes. The emplacement of both of these LIPs, which were potentially associated with the break-up of the supercontinent Rodinia (Ernst et al., 2008), do not appear to have any significant impact on the trend of increasing $^{87}\text{Sr}/^{86}\text{Sr}$, which is consistent with the climate at the latitudes of their emplacement not being conducive to a high weathering rate. At ca. 780 Ma, the Gunbarrel LIP is emplaced in the tropics, which roughly coincides with the inflection in $^{87}\text{Sr}/^{86}\text{Sr}$ ca. 770 Ma, when $^{87}\text{Sr}/^{86}\text{Sr}$ begins decreasing leading into the ca. 717 Ma Sturtian Glaciation. Notably, however, none of the three post-emplacement models in Figure 13D predict any significant difference in the contribution of juvenile rocks to the global weathering flux between ca. 880-770 Ma when $^{87}\text{Sr}/^{86}\text{Sr}$ is observed to be increasing and ca. 770-717 Ma when $^{87}\text{Sr}/^{86}\text{Sr}$ is observed to be decreasing. In other words, all three models place a roughly stable area of weatherable LIPs in the tropics between ca. 880 and 717 Ma, with the notable exception of the Franklin LIP causing an increase ca. 720 Ma (Denyszyn et al., 2009).

The lack of a clear correlation between the LIP record and the ca. 770-717 Ma descent in $^{87}\text{Sr}/^{86}\text{Sr}$ suggests that there are other factors that are driving at least some of the major trends observed in the Tonian $^{87}\text{Sr}/^{86}\text{Sr}$ record. In order to explore these factors, we constructed a simple global weathering model that tracks calcium, magnesium, and strontium fluxes into and out of the ocean. This model is modified from Maloof et al. (2010) and the Python code that implements it

1075 is available in the data repository. The core of the model is based around three equations:

$$\frac{dCa}{dt} = W_{Ca-carb} + W_{Ca-rad} + W_{Ca-juv} + H_{Ca-basalt} - P_{Ca-carb} \quad (1)$$

$$\frac{dMg}{dt} = W_{Mg-carb} + W_{Mg-rad} + W_{Mg-juv} - H_{Mg-clays} - P_{Mg-carb} \quad (2)$$

$$\frac{dSr}{dt} = W_{nSr-carb} + W_{nSr-rad} + W_{nSr-juv} + H_{nSr-basalt} - P_{nSr-carb} \quad (3)$$

1076 W_{X-carb} , W_{X-rad} , and W_{X-juv} are the inputs of Ca, Mg, and Sr coming from subaerial
 1077 weathering of carbonate (*carb*), radiogenic (*rad*) lithologies, and juvenile (*juv*) lithologies
 1078 respectively. Each of these terms can be broken down into:

$$W_{X-lithology} = W_{lithology} \times [X]_{lithology} \quad (4)$$

1079 $W_{lithology}$ is the total (all elements) weathering flux coming from the given lithology, and
 1080 $[X]_{lithology}$ is the average concentration of Ca, Mg, and Sr in the given lithology. $H_{Mg-clays}$ is the
 1081 loss of Mg in seawater due to the precipitation of clay minerals, $H_{X-basalt}$ is the input of Ca and
 1082 Sr associated with the weathering of ocean crust during hydrothermal circulation on or near
 1083 mid-ocean ridges, and P_{X-carb} is the Mg, Ca, and Sr sink associated with the formation of
 1084 carbonate minerals. n refers to each isotope of Sr (^{88}Sr , ^{87}Sr , ^{86}Sr). The values of variables used
 1085 in our model are listed in the data repository. We note that the simple global weathering model
 1086 used here does not account for changes in seawater chemistry due to dolomitization, which may
 1087 have acted as a quantitatively significant input/output flux for Mg, Ca, and Sr (Fantle and
 1088 Higgins, 2014).

1089 We first spin up the model to steady state over 500 Myr, choosing total Mg, total Ca, k , W_{carb} ,

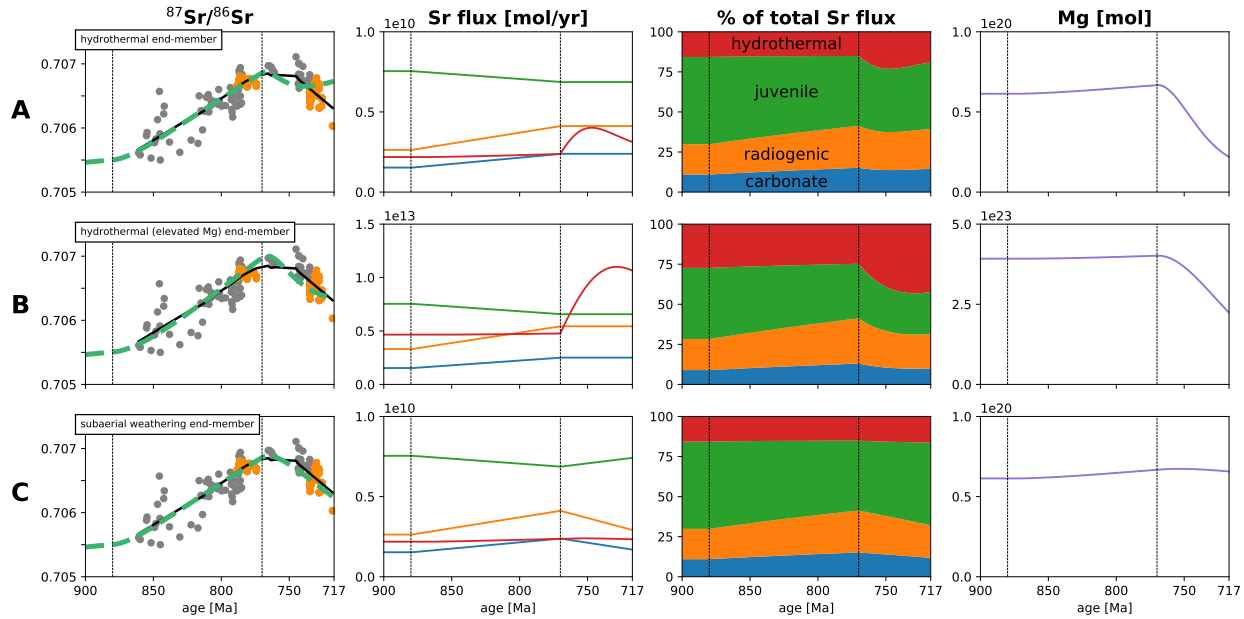


Figure 14. Global weathering model results. Each row represents a different weathering flux scenario. In the first column, the black curves are the LOWESS fits from Figure 13, and the dashed green curves are the model outputs. Vertical black lines represent times when changes in weathering flux are forced in the model. Each model run has the same weathering flux trajectories from 880 to 770 Ma with varying scenarios between 770 Ma and the onset of Sturtian Glaciation. **(A)** Change in hydrothermal flux only end-member scenario. **(B)** Change in hydrothermal flux only with elevated ocean [Mg] end-member scenario. **(C)** Change in subaerial weathering fluxes only end-member scenario. Note that in the second and fourth columns, scenario B uses different y-axis scales than that used in scenarios A and B. See text for further details.

1090 W_{rad} , and W_{juv} such that, at the model start age of 880 Ma, Mg/Ca = 10 (based on fluid
 1091 inclusion data from Spear et al., 2014) and $^{87}\text{Sr}/^{86}\text{Sr} = 0.7055$ (to match the $^{87}\text{Sr}/^{86}\text{Sr}$ of the time;
 1092 Fig. 12). As a percentage of the total Sr input into the ocean, this model yields hydrothermal =
 1093 ~15%, carbonate = ~10%, radiogenic lithologies = ~20%, and juvenile lithologies = ~55% (Fig.
 1094 14A and B). Although not a unique solution, it is reasonable and expected that our initial
 1095 steady-state Sr fluxes have a higher contribution from juvenile sources (both subaerial weathering
 1096 of juvenile lithologies and hydrothermal exchange) than is estimated for the present, considering
 1097 that modern seawater has a much higher $^{87}\text{Sr}/^{86}\text{Sr}$ of ~0.7091 (hydrothermal = ~10%, carbonate
 1098 = ~35%, radiogenic lithologies = ~25%, and juvenile lithologies = ~30%, from Allègre et al.,

1099 2010). After initial spin up to steady state, total silicate Mg + Ca weathering is held constant
1100 throughout the model runs to avoid untenable variations in pCO₂ over million-year time scales
1101 (Berner and Caldeira, 1997). We also make the simplifying assumption that carbonate lithologies
1102 are distributed homogenously over the globe wherever radiogenic lithologies exist, and thus also
1103 hold the ratio of W_{rad} to W_{carb} constant throughout the model runs.

1104 From these initial conditions, we sought to explore scenarios that would result in the observed
1105 pre-Sturtian Glaciation $^{87}\text{Sr}/^{86}\text{Sr}$ curve. We find that forcing a linear increase in the proportion
1106 of the subaerial weathering flux from both the radiogenic lithologies and carbonates (W_{rad} and
1107 W_{carb}) from ~20% and ~10% respectively at 880 Ma to ~25% and ~15% respectively at 770 Ma,
1108 while decreasing the proportion of the subaerial weathering flux from juvenile lithologies (W_{juv})
1109 from ~55% to ~45%, produces the increase in $^{87}\text{Sr}/^{86}\text{Sr}$ from ca. 880 Ma (Fig. 14A and C). This
1110 solution represents a feasible tectonic scenario for this time interval - Rodinia had begun to rift
1111 apart at low latitudes during this time (Li et al., 2008), which would have brought ocean basins in
1112 proximity to previously landlocked continental interiors, resulting in as much as an order of
1113 magnitude increase in runoff in these areas (Goddéris et al., 2017b). The increased runoff in
1114 previously arid continental interiors, combined with the generally high runoff and temperature at
1115 low latitudes, could have increased the relative weathering flux from radiogenic continental
1116 interiors and driven up marine $^{87}\text{Sr}/^{86}\text{Sr}$ between ca. 880-770 Ma, as proposed by Halverson et al.
1117 (2007a). In addition, as discussed above, the ‘decay’ and ‘weathering’ models both predict a small
1118 weatherable area of LIPs in the tropics ca. 880-770 Ma relative to the preceding ~230 Myr (Fig.
1119 13D). This tectonic scenario also could have contributed to driving $^{87}\text{Sr}/^{86}\text{Sr}$ to higher values by
1120 decreasing the weathering flux from juvenile sources. Since increases or decreases in W_{rad} must be
1121 matched by decreases or increases in W_{juv} in order to keep total silicate Mg + Ca weathering
1122 constant, the combination of Rodinia rifting apart at low latitudes and a decreasing weatherable
1123 area of LIPs within the tropics could have driven $^{87}\text{Sr}/^{86}\text{Sr}$ to higher values. However, significant
1124 uncertainty associated with these Tonian paleogeographic reconstructions remain, and this
1125 modeled solution is non-unique. Nevertheless, there needs to be an increase in the Sr flux from

1126 radiogenic sources relative to juvenile ones to produce the observed increase in $^{87}\text{Sr}/^{86}\text{Sr}$ ca.
1127 880-770 Ma. We note that the rifting of a supercontinent may be associated with an increase in
1128 the length of mid-ocean ridges, and therefore an increase in the low $^{87}\text{Sr}/^{86}\text{Sr}$ flux coming from
1129 hydrothermal systems (as has been proposed for the opening of the Iapetus Ocean in the Early
1130 Cambrian; Maloof et al., 2010). However, since the majority of oceanic crust preserved today is
1131 younger than the beginning of the break up of the most recent supercontinent Pangea (Müller
1132 et al., 2008), the effect of supercontinent break up on total mid-ocean ridge length is poorly
1133 constrained. Nevertheless, even if the low $^{87}\text{Sr}/^{86}\text{Sr}$ flux coming from hydrothermal systems
1134 increased during Rodinia break up, it must have been overwhelmed by the increase in the Sr flux
1135 from radiogenic sources in order to drive $^{87}\text{Sr}/^{86}\text{Sr}$ to higher values during this time.

1136 To explain the fall in $^{87}\text{Sr}/^{86}\text{Sr}$ leading into the Sturtian Glaciation, we consider two
1137 end-member scenarios. In the first scenario, the absolute flux of H_2O in hydrothermal systems (k)
1138 increases, which could represent an increasing length of mid-ocean ridges. In the second scenario,
1139 the relative flux coming from the subaerial weathering of juvenile vs. radiogenic lithologies
1140 increases, which could represent either an increase in the weatherable area of subaerially exposed
1141 LIPs and arcs, a movement/emplacement of LIPs and arcs into higher runoff areas, a movement
1142 of radiogenic continental crust into lower runoff areas, or a combination of these forcings.

1143 To replicate the first end-member scenario, we try forcing a 4-fold linear increase in the
1144 absolute flux of H_2O in hydrothermal systems from 770 to 717 Ma (Fig. 14A). While this forcing
1145 produces a $^{87}\text{Sr}/^{86}\text{Sr}$ curve that matches the initial observed downturn starting at 770 Ma, it later
1146 deviates from the observed $^{87}\text{Sr}/^{86}\text{Sr}$ curve and begins rising at ca. 740 Ma. This change in the
1147 modeled $^{87}\text{Sr}/^{86}\text{Sr}$ trajectory is a result of depleting seawater of Mg due to the increasing flux of
1148 H_2O in hydrothermal systems. This Mg-depletion reduces hydrothermal Mg-Ca exchange, which
1149 in turn reduces the Sr flux coming from hydrothermal alteration (Berndt et al., 1988). However,
1150 since the absolute concentration of ions in seawater is poorly constrained during the
1151 Neoproterozoic, we tried to circumvent the problem of depleting [Mg] by changing the initial

1152 steady-state conditions such that [Mg] was ~3 orders of magnitude higher than that used in the
1153 first model (Fig. 14B). Even with this unrealistically large increase in [Mg] (which requires
1154 increasing the initial steady-state subaerial weathering flux from juvenile, radiogenic, and
1155 carbonate lithologies by 3 orders of magnitude relative to the initial steady-state conditions used
1156 in the first model in order to maintain initial Mg/Ca = 10), a ~4-fold increase in the absolute
1157 flux of H₂O in hydrothermal systems from 770 to 717 Ma is still required to match the observed
1158 ⁸⁷Sr/⁸⁶Sr curve. As discussed above, it is unclear how supercontinent break up effects the total
1159 length of mid-ocean ridges, but a 4-fold increase in this length should be unrealistically large,
1160 especially when we consider that mid-ocean ridges outside of Rodinia existed independent of the
1161 break-up of the supercontinent. The Arabian-Nubian Shield itself is comprised of ~10
1162 tectonostratigraphic island arc terranes that accreted onto the periphery of Rodinia (Johnson,
1163 2014) resulting from active seafloor spreading. Furthermore, if the hypothesis that rifting played
1164 an important role in increasing the Sr flux coming from radiogenic lithologies ca. 880-770 Ma is
1165 correct, the associated possible increase in the length of mid-ocean ridges would have preceded
1166 the decline in ⁸⁷Sr/⁸⁶Sr going into the glaciation.

1167 To replicate the second end-member scenario, we found that forcing a linear increase in the
1168 subaerial weathering flux from juvenile lithologies from ~45% at 770 Ma to ~55% at 717 Ma
1169 (while keeping total silicate Mg + Ca weathering constant) produces the decrease in ⁸⁷Sr/⁸⁶Sr
1170 from ca. 770 Ma leading into the Sturtian Glaciation (Fig. 14C). This forcing is approximately
1171 equivalent to a return to pre-880 Ma steady-state conditions.

1172 Together, these three global weathering model scenarios (Fig. 14) suggest that the primary
1173 driver of decreasing ⁸⁷Sr/⁸⁶Sr leading into the Sturtian Glaciation was the second end-member
1174 scenario – an increasing relative flux coming from the subaerial weathering of juvenile, rather
1175 than radiogenic, lithologies. However, as discussed above, all three post-emplacement models in
1176 Figure 13D place a roughly stable area of weatherable LIPs in the tropics ca. 880-720 Ma.
1177 Therefore, an increase in the weathering flux from LIPs is likely not the primary driver for

1178 increasing the relative flux coming from the weathering of juvenile lithologies starting ca. 770 Ma.
1179 Furthermore, current paleogeographic reconstructions overall suggest that Rodinia continued to
1180 rift apart at low latitudes ca. 770-717 Ma (e.g. Li et al., 2008) in a manner similar to that
1181 described above for ca. 880-770 Ma. Such plate motions would not lead to any significant increase
1182 of ‘continentality’ or movement of continental crust into higher latitudes ca. 770-717 Ma, and
1183 therefore an associated decrease in the weathering flux from radiogenic continental crust as a
1184 result of these processes is not expected.

1185 A potential driver of the ca. 770 Ma inflection in the $^{87}\text{Sr}/^{86}\text{Sr}$ record is the first episode of
1186 Arabian-Nubian arc accretion along the Bi'r Umq-Nakasib Suture – estimated to have occurred
1187 ca. 780-760 Ma based on the ages of terrane protoliths and of syn- and post-tectonic intrusions
1188 (Pallister et al., 1988; Johnson et al., 2003; Johnson and Woldehaimanot, 2003; Johnson, 2014;
1189 Fig. 13E). This accretion event represents a difference between ca. 880-770 Ma and ca.
1190 770-720 Ma, and was followed by accretion along the Allaqi-Heiani-Yanbu Suture – estimated to
1191 have occurred ca. 730-710 Ma based on the ages of terrane protoliths and post-tectonic intrusions
1192 (Ali et al., 2010; Johnson, 2014; Kozdrój et al., 2017). The paleolatitude of this accretion and
1193 associated exhumation is poorly constrained. However, the record of Arabian-Nubian arc
1194 accretion during the late Neoproterozoic assembly of Gondwana suggests that the
1195 Arabian-Nubian arc terranes were situated between India and the Congo + Saharan cratons (Li
1196 et al., 2008; Hoffman and Li, 2009). This position leads to a low to mid-latitude position at the
1197 time of the ca. 780-760 Ma accretion event within paleogeographic models (e.g. Li et al., 2008;
1198 Swanson-Hysell et al., 2018; Fig. 13E). A tropical position of proto-Arabian-Nubian Shield arc
1199 terranes is consistent with the interpreted depositional environment of the Tambien Group, given
1200 the abundance of carbonate lithofacies such as oolite which are indicative of warm waters that are
1201 supersaturated with respect to calcium carbonate (Fig. 3). Exhumation associated with arc
1202 terrane collision would have increased physical erosion through the development of steep
1203 topography, preventing regolith development and associated attenuation of the chemical
1204 weathering of the island arc rocks (Gabet and Mudd, 2009). The exhumation also would generate

a constant supply of fresh rocks that would allow chemical weathering rates to remain high for the duration of the event. The development of topography also generates a physical barrier that forces air masses to rise and cool, which should result in an increase in the local precipitation, supplementing the already high precipitation in the tropics. Together, these factors could have substantially increased the weathering flux coming from these juvenile island arcs. Given that the LIP analysis (Fig. 13D) suggests that an increase in the weathering flux from LIPs ca. 880-720 Ma is unlikely, this episode of Arabian-Nubian arc accretion stands as a strong candidate for the primary driver for falling $^{87}\text{Sr}/^{86}\text{Sr}$ starting ca. 770 Ma. Similarly, arc-continent collision in the tropics also has been invoked to explain the fall in $^{87}\text{Sr}/^{86}\text{Sr}$ in the Ordovician (Swanson-Hysell and Macdonald, 2017).

Other major ca. 1300-700 Ma arc accretion events that can be identified in the geological record (Fig. 13E) include: the ca. 1204-1174 Ma accretion of the Pie de Palo Complex (Vujovich and Kay, 1998; Vujovich et al., 2004) and the ca. 1200-1160 Ma accretion of the Pyrites Ophiolite Complex (McLellan et al., 2013) onto Laurentia during the Shawinigan Orogeny, the ca. 870-813 Ma accretion of the Miaowan Ophiolite onto the northern margin of the Yangtze block of South China (Peng et al., 2012), the ca. 825-815 Ma Jiangnan Orogen associated with the closure of the ocean basin between the terranes of the Yangtze and Cathaysia blocks that make up South China (Zhao, 2015), and the ca. 820-800 Ma closure of the ocean basin between the Greater India landmass and the Marwar craton (Volpe and Douglas Macdougall, 1990; Chatterjee et al., 2017). However, paleomagnetic poles place Laurentia (Palmer et al., 1977; Buchan et al., 2000), South China (Li et al., 2004; Niu et al., 2016), and India (Meert et al., 2013) outside of the tropics at or near the time of these accretion events, indicating that exhumation of associated mafic lithologies would have occurred at mid- to high latitudes with a correspondingly muted influence on global weathering and $^{87}\text{Sr}/^{86}\text{Sr}$ values compared to the Arabian-Nubian events (Fig. 13). We note, however, that this compilation of ca. 1300-700 Ma arc accretion events (Fig. 13E) is limited to the current literature on ophiolite-bearing sutures. Additional arc accretion events associated with the late Mesoproterozoic-early Neoproterozoic assembly of Rodinia (Cawood et al., 2016),

1232 may not be preserved due to exhumation and erosion. Therefore, while it is possible that
1233 Arabian-Nubian arc accretion is unique in terms of a low-latitude position in this time interval,
1234 such a conclusion would be premature.

1235 By appreciating that arc accretion, especially in the tropics, has the potential to contribute
1236 sufficient solutes to the global weathering flux to alter global marine $^{87}\text{Sr}/^{86}\text{Sr}$ for tens of millions
1237 of years, we can examine the factors that contributed to the ca. 717 Ma initiation of the Sturtian
1238 Glaciation from a fresh perspective. Age constraints on the emplacement of the Franklin LIP into
1239 the tropics (Fig. 13C and D) cluster at ca. 720 Ma, but range from ca. 723 Ma to ca. 712 Ma
1240 (Heaman et al., 1992; Pehrsson and Buchan, 1999; Denyszyn et al., 2009). Without tighter age
1241 constraints on the timing of this emplacement, interpreting its precise relationship to the ca.
1242 717 Ma initiation of the Sturtian Glaciation is difficult. If the emplacement precisely coincided
1243 with the initiation of the Sturtian Glaciation, then its primary contribution to initiating Snowball
1244 Earth could have been through cooling associated with the injection of sulfur aerosols into the
1245 stratosphere (Macdonald and Wordsworth, 2017). On the other hand, if the emplacement
1246 preceded the initiation by several million years, then its contribution to it would have been to
1247 enhance planetary weatherability (Goddéris et al., 2003; Rooney et al., 2014; Cox et al., 2016),
1248 since the residence time of sulfur aerosols in the stratosphere is less than a few years (McCormick
1249 et al., 1995). Regardless of the precise nature of this relationship, our LIP area analysis (Fig. 13C
1250 and D) indicates that the Franklin LIP does not correspond to a uniquely large LIP area in the
1251 tropics. While it is one of the two highest peaks of tropical LIP area in the 1300-700 Ma interval,
1252 a larger area of weatherable LIP is reconstructed to have existed both globally and within the
1253 tropics at ca. 1100 Ma due to the Umkondo LIP, comparable in size to the Franklin LIP, being
1254 emplaced in the tropics ca. 1110 Ma, as well as the migration of the SW Laurentia LIP into the
1255 tropics at this time. Given that there was no Snowball Earth glaciation ca. 1100 Ma despite there
1256 being a larger area of weatherable LIPs emplaced within the tropics than ca. 717 Ma, it is
1257 difficult to explain the initiation of the Sturtian Glaciation with the Franklin LIP alone.

1258 However, what may differentiate the interval preceding the Sturtian Glaciation and ca.
1259 1100 Ma are the pair of Arabian-Nubian arc accretion events that potentially occurred in the
1260 tropics (Fig. 13E). Within this context, the Franklin LIP was not solely responsible for cooling
1261 Earth to the threshold required to initiate global glaciation. Rather, as suggested by the
1262 $^{87}\text{Sr}/^{86}\text{Sr}$ record, we propose that Arabian-Nubian arc accretion in the tropics enhanced planetary
1263 weatherability and lowered atmospheric CO₂ concentration over the ~50 Myr prior to the
1264 initiation of the Sturtian Glaciation. The Franklin LIP then was emplaced in the tropics into an
1265 already cool planet, and its additional cooling effect, either through CO₂ consumption via silicate
1266 weathering and/or cooling associated with the injection of sulfur aerosols, may have tipped the
1267 climate over the threshold required for the ice-albedo positive feedback to overwhelm negative
1268 feedbacks on cooling and initiate global glaciation. Therefore, Arabian-Nubian arc accretion may
1269 have worked together with LIP emplacement to allow global glaciation to occur, and that without
1270 this arc exhumation, the Sturtian Glaciation may not have occurred. Subsequent arc accretion
1271 events within the Arabian Shield in the Cryogenian (Johnson, 2014) may have played a role in
1272 elevating planetary weatherability and contributing to the onset of the Marinoan Glaciation as
1273 well. Other studies also have argued that tropical arc accretion events contributed to global
1274 cooling in the Eocene, Cretaceous (Jagoutz et al., 2016), and Ordovician (Swanson-Hysell and
1275 Macdonald, 2017). Crucially, this hypothesis hinges on the paleogeographic position of these
1276 Arabian-Nubian arc accretion events to sufficiently increase planetary weatherability. Direct
1277 paleomagnetic data that provides such constraints should be a priority for future research.
1278 Furthermore, the LIP and arc accretion analysis presented here is limited to ca. 1300–700 Ma,
1279 and extending this analysis to the rest of Earth history is necessary to further evaluate the
1280 uniqueness of the combination of tropical LIPs, tropical arc accretion events, and global cooling.

1281 CONCLUSIONS

1282 The Tambien Group was deposited for over 100 million years of Tonian Earth history leading into
1283 the Sturtian Glaciation. The presence of carbonates and tuffs throughout the strata enable the
1284 generation of temporally well-constrained chemostratigraphic data leading into the first of the
1285 Cryogenian glaciations. We have used new $\delta^{13}\text{C}$ and $^{87}\text{Sr}/^{86}\text{Sr}$ data and U-Pb ages from the
1286 Tambien Group to construct the most temporally well-constrained Tonian composite
1287 chemostratigraphic dataset to date, and used it to show: 1) that the Islay Anomaly is
1288 synchronous in at least two separate basins, precedes the Sturtian Glaciation by \sim 18 Myr, and is
1289 followed by a prolonged interval of positive $\delta^{13}\text{C}$ values; 2) low-latitude glaciation was likely rapid
1290 leading into the Sturtian Glaciation, as predicted by energy balance models; and 3) enhanced
1291 subaerial weathering of juvenile lithologies, and thus enhanced consumption of CO₂, began
1292 \sim 50 Myr prior to the initiation of the Sturtian Glaciation. The accretion of Arabian-Nubian
1293 Shield volcanic arcs in the tropics during this time likely played an important role in increasing
1294 global weatherability, contributing to the initiation of the first Neoproterozoic Snowball Earth.

1295 ACKNOWLEDGEMENTS

1296 Research funding came from the U.S. National Science Foundation grants EAR-1325230 (Swanson-Hysell) and
1297 EAR-1323158 (Maloof). Tremblay was supported by an U.S. National Science Foundation Graduate Research
1298 Fellowship. Sr isotope data were collected in the Center for Isotope Geochemistry at UC Berkeley directed by Don
1299 DePaolo, which is supported by the Director, Office of Science, Office of Basic Energy Sciences, of the U.S.
1300 Department of Energy under contract number DE-AC02-05CH11231. Acknowledgement and thanks go to Shaun
1301 Brown and Thomas Owens for assisting with the development of Sr isotope data, to Wenbo Yang for assisting with
1302 the development of element concentration data, Samantha Gwizd, Sergey Oleynik, and Disha Okhai for assisting
1303 with the development of C and O isotope data, and Sara Beroff for assisting with the development of the molar
1304 tooth structure petrographic data with support from the Cal NERDS program. Gawen Jenkin helped introduce
1305 Swanson-Hysell and Maloof to the Tambien Group. Daniel Condon was instrumental in generating previous U-Pb
1306 dates on the Tambien Group that was built-upon in the current work.

1307 References

- 1308 Alene, M., 1998, Tectonomagmatic evolution of the Neoproterozoic rocks of the Mai Kenetal-Negash area, Tigrai,
1309 northern Ethiopia: Ph.D. thesis, University of Turin.
- 1310 Alene, M., Jenkin, G. R. T., Leng, M. J., and Darbyshire, D. P. F., 2006, The Tambien Group, Ethiopia: an early
1311 Cryogenian (ca. 800–735 Ma) Neoproterozoic sequence in the Arabian-Nubian Shield: *Precambrian Research*, vol.
1312 147, pp. 79–99, doi:10.1016/j.precamres.2006.02.002.
- 1313 Ali, K. A., Azer, M. K., Gahlan, H. A., Wilde, S. A., Samuel, M. D., and Stern, R. J., 2010, Age constraints on the
1314 formation and emplacement of Neoproterozoic ophiolites along the Allaqi-Heiani Suture, south eastern desert of
1315 Egypt: *Gondwana Research*, vol. 18, pp. 583–595, doi:10.1016/j.gr.2010.03.002.
- 1316 Allègre, C. J., Louvat, P., Gaillardet, J., Meynadier, L., Rad, S., and Capmas, F., 2010, The fundamental role of
1317 island arc weathering in the oceanic Sr isotope budget: *Earth and Planetary Science Letters*, vol. 292, pp. 51–56,
1318 doi:10.1016/j.epsl.2010.01.019.
- 1319 Arkin, Y., Beyth, M., Dow, D. B., Levitte, D., Haile, T., and Hailu, T., 1971, Geological map of Mekele Sheet area
1320 ND37-11 Tigre Province: Imperial Ethiopian Government, Ministry of Mines. Geological Survey of Ethiopia.
- 1321 Asmerom, Y., Jacobsen, S. B., Knoll, A. H., Butterfield, N. J., and Swett, K., 1991, Strontium isotopic variations of
1322 Neoproterozoic seawater: implications for crustal evolution: *Geochimica et Cosmochimica Acta*, vol. 55, pp.
1323 2883–2894, doi:10.1016/0016-7037(91)90453-C.
- 1324 Avigad, D., Stern, R. J., Beyth, M., Miller, N., and McWilliams, M. O., 2007, Detrital zircon U-Pb geochronology
1325 of Cryogenian diamictites and Lower Paleozoic sandstone in Ethiopia (Tigrai): age constraints on Neoproterozoic
1326 glaciation and crustal evolution of the southern Arabian-Nubian Shield: *Precambrian Research*, vol. 154, pp.
1327 88–106, doi:10.1016/j.precamres.2006.12.004.
- 1328 Banner, J. L. and Hanson, G. N., 1990, Calculation of simultaneous isotopic and trace element variations during
1329 water-rock interaction with applications to carbonate diagenesis: *Geochimica et Cosmochimica Acta*, vol. 54, pp.
1330 3123–3137, doi:10.1016/0016-7037(90)90128-8.
- 1331 Bartley, J. K., Semikhatov, M. A., Kaufman, A. J., Knoll, A. H., Pope, M. C., and Jacobsen, S. B., 2001, Global
1332 events across the Mesoproterozoic–Neoproterozoic boundary: C and Sr isotopic evidence from Siberia:
1333 *Precambrian Research*, vol. 111, pp. 165–202, doi:10.1016/S0301-9268(01)00160-7.
- 1334 Bauerman, H., 1884, Report on the geology of the country near the forty-ninth parallel of north latitude west of the
1335 Rocky Mountains: from observations made 1859–1861: Dawson.
- 1336 Baum, S. K. and Crowley, T. J., 2001, GCM response to Late Precambrian (~590 Ma) ice-covered continents:
1337 *Geophysical Research Letters*, vol. 28, pp. 583–586, doi:10.1029/2000GL011557.
- 1338 Berhe, S. M., 1990, Ophiolites in northeast and east Africa: implications for Proterozoic crustal growth: *Journal of*
1339 *the Geological Society*, vol. 147, pp. 41–57, doi:10.1144/gsjgs.147.1.0041.
- 1340 Berndt, M. E., Seyfried, W. E., and Beck, J. W., 1988, Hydrothermal alteration processes at midocean ridges:
1341 experimental and theoretical constraints from Ca and Sr exchange reactions and Sr isotopic ratios: *Journal of*
1342 *Geophysical Research: Solid Earth*, vol. 93, pp. 4573–4583, doi:10.1029/JB093iB05p04573.
- 1343 Berner, R. A. and Caldeira, K., 1997, The need for mass balance and feedback in the geochemical carbon cycle:
1344 *Geology*, vol. 25, pp. 955–956, doi:10.1130/0091-7613(1997)025<0955:TNFMBA>2.3.CO;2.
- 1345 Beyth, M., 1972, To the geology of central-western Tigre: *Rheinisch Friedrich-Wilhelms-Universitaet*.
- 1346 Beyth, M., Avigad, D., Wetzel, H.-U., Matthews, A., and Berhe, S. M., 2003, Crustal exhumation and indications
1347 for Snowball Earth in the East African Orogen: north Ethiopia and east Eritrea: *Precambrian Research*, vol.
1348 123, pp. 187–201, doi:10.1016/S0301-9268(03)00067-6.

- 1349 Bishop, J. W. and Sumner, D. Y., 2006, Molar tooth structures of the Neoarchean Monteville Formation, Transvaal
1350 Supergroup, South Africa. I: Constraints on microcrystalline CaCO₃ precipitation: *Sedimentology*, vol. 53, pp.
1351 1049–1068, doi:10.1111/j.1365-3091.2006.00801.x.
- 1352 Bold, U., Smith, E. F., Rooney, A. D., Bowring, S. A., Buchwaldt, R., Dudás, F. Ő., Ramezani, J., Crowley, J. L.,
1353 Schrag, D. P., and Macdonald, F. A., 2016, Neoproterozoic stratigraphy of the Zavkhan terrane of Mongolia: the
1354 backbone for Cryogenian and early Ediacaran chemostratigraphic records: *American Journal of Science*, vol. 316,
1355 pp. 1–63, doi:10.2475/01.2016.01.
- 1356 Bowring, S. A., Grotzinger, J. P., Condon, D. J., Ramezani, J., Newall, M. J., and Allen, P. A., 2007,
1357 Geochronologic constraints on the chronostratigraphic framework of the Neoproterozoic Huqf Supergroup,
1358 Sultanate of Oman: *American Journal of Science*, vol. 307, pp. 1097–1145, doi:10.2475/10.2007.01.
- 1359 Brand, U., 2004, Carbon, oxygen and strontium isotopes in Paleozoic carbonate components: an evaluation of
1360 original seawater-chemistry proxies: *Chemical Geology*, vol. 204, pp. 23–44, doi:10.1016/j.chemgeo.2003.10.013.
- 1361 Brand, U. and Veizer, J., 1980, Chemical diagenesis of a multicomponent carbonate system-1: Trace elements:
1362 *Journal of Sedimentary Research*, vol. 50, pp. 1219–1236, doi:10.1306/212F7BB7-2B24-11D7-8648000102C1865D.
- 1363 Brasier, M., McCarron, G., Tucker, R., Leather, J., Allen, P., and Shields, G., 2000, New U-Pb zircon dates for the
1364 Neoproterozoic Ghubrah glaciation and for the top of the Huqf Supergroup, Oman: *Geology*, vol. 28, pp.
1365 175–178, doi:10.1130/0091-7613(2000)28<175:NUZDFT>2.0.CO;2.
- 1366 Brasier, M. D., Shields, G., Kuleshov, V. N., and Zhegallo, E. A., 1996, Integrated chemo- and biostratigraphic
1367 calibration of early animal evolution: Neoproterozoic-early Cambrian of southwest Mongolia: *Geological
1368 Magazine*, vol. 133, pp. 445–485, doi:10.1017/S0016756800007603.
- 1369 Broecker, W. S. and Peng, T.-H., 1982, *Tracers in the Sea*: Cambridge University Press,
1370 doi:10.1017/S0033822200005221.
- 1371 Buchan, K. L., Mertanen, S., Park, R. G., Pesonen, L. J., Elming, S.-Å., Abrahamsen, N., and Bylund, G., 2000,
1372 Comparing the drift of Laurentia and Baltica in the Proterozoic: the importance of key palaeomagnetic poles:
1373 *Tectonophysics*, vol. 319, pp. 167–198, doi:10.1016/S0040-1951(00)00032-9.
- 1374 Bussert, R., 2010, Exhumed erosional landforms of the Late Palaeozoic glaciation in northern Ethiopia: Indicators
1375 of ice-flow direction, palaeolandscape and regional ice dynamics: *Gondwana Research*, vol. 18, pp. 356–369,
1376 doi:10.1016/j.gr.2009.10.009.
- 1377 Butterfield, N. J., 2015, Proterozoic photosynthesis – a critical review: *Palaeontology*, vol. 58, pp. 953–972,
1378 doi:10.1111/pala.12211.
- 1379 Cawood, P. A., Strachan, R. A., Pisarevsky, S. A., Gladkochub, D. P., and Murphy, J. B., 2016, Linking collisional
1380 and accretionary orogens during Rodinia assembly and breakup: Implications for models of supercontinent
1381 cycles: *Earth and Planetary Science Letters*, vol. 449, pp. 118–126, doi:10.1016/j.epsl.2016.05.049.
- 1382 Chatterjee, S. M., Roy Choudhury, M., Das, S., and Roy, A., 2017, Significance and dynamics of the Neoproterozoic
1383 (810 Ma) Phulad Shear Zone, Rajasthan, NW India: *Tectonics*, vol. 36, pp. 1432–1454, doi:10.1002/2017tc004554.
- 1384 Collins, A. S. and Windley, B. F., 2002, The tectonic evolution of central and northern Madagascar and its place in
1385 the final assembly of Gondwana: *The Journal of Geology*, vol. 110, pp. 325–339, doi:10.1086/339535.
- 1386 Condon, D. J., Schoene, B., McLean, N. M., Bowring, S. A., and Parrish, R. R., 2015, Metrology and traceability of
1387 U-Pb isotope dilution geochronology (EARTHTIME tracer calibration part I): *Geochimica et Cosmochimica
1388 Acta*, vol. 164, pp. 464–480, doi:10.1016/j.gca.2015.05.026.
- 1389 Cox, G. M., Foden, J., and Collins, A. S., 2018, Late Neoproterozoic adakitic magmatism of the eastern Arabian
1390 Nubian Shield: *Geoscience Frontiers*, doi:10.1016/j.gsf.2017.12.006.

- 1391 Cox, G. M., Halverson, G. P., Stevenson, R. K., Vokaty, M., Poirier, A., Kunzmann, M., Li, Z.-X., Denyszyn, S. W.,
1392 Strauss, J. V., and Macdonald, F. A., 2016, Continental flood basalt weathering as a trigger for Neoproterozoic
1393 Snowball Earth: *Earth and Planetary Science Letters*, vol. 446, pp. 89–99, doi:10.1016/j.epsl.2016.04.016.
- 1394 Cox, G. M., Lewis, C. J., Collins, A. S., Halverson, G. P., Jourdan, F., Foden, J., Nettle, D., and Kattan, F., 2012,
1395 Ediacaran terrane accretion within the Arabian-Nubian Shield: *Gondwana Research*, vol. 21, pp. 341–352,
1396 doi:10.1016/j.gr.2011.02.011.
- 1397 Cox, G. M., Strauss, J. V., Halverson, G. P., Schmitz, M. D., McClelland, W. C., Stevenson, R. S., and Macdonald,
1398 F. A., 2015, Kikiktat volcanics of Arctic Alaska—melting of harzburgitic mantle associated with the Franklin large
1399 igneous province: *Lithosphere*, vol. 7, pp. 275–295, doi:10.1130/L435.1.
- 1400 Daly, R. A., 1912, Geology of the North American Cordillera at the forty-ninth parallel: US Government Printing
1401 Office.
- 1402 Denyszyn, S. W., Halls, H. C., Davis, D. W., and Evans, D. A., 2009, Paleomagnetism and U-Pb geochronology of
1403 Franklin dykes in High Arctic Canada and Greenland: a revised age and paleomagnetic pole constraining block
1404 rotations in the Nares Strait region: *Canadian Journal of Earth Sciences*, vol. 46, pp. 689–705,
1405 doi:10.1139/E09-042.
- 1406 Derry, L. A., 2010, A burial diagenesis origin for the Ediacaran Shuram-Wonoka carbon isotope anomaly: *Earth*
1407 and *Planetary Science Letters*, vol. 294, pp. 152–162, doi:10.1016/j.epsl.2010.03.022.
- 1408 Dessert, C., Dupré, B., François, L. M., Schott, J., Gaillardet, J., Chakrapani, G., and Bajpai, S., 2001, Erosion of
1409 Deccan Traps determined by river geochemistry: impact on the global climate and the $^{87}\text{Sr}/^{86}\text{Sr}$ ratio of
1410 seawater: *Earth and Planetary Science Letters*, vol. 188, pp. 459–474, doi:10.1016/S0012-821X(01)00317-X.
- 1411 Dessert, C., Dupré, B., Gaillardet, J., François, L. M., and Allègre, C. J., 2003, Basalt weathering laws and the
1412 impact of basalt weathering on the global carbon cycle: *Chemical Geology*, vol. 202, pp. 257–273,
1413 doi:10.1016/j.chemgeo.2002.10.001.
- 1414 Ernst, R. E., Wingate, M. T. D., Buchan, K. L., and Li, Z. X., 2008, Global record of 1600–700 ma Large Igneous
1415 Provinces (LIPs): implications for the reconstruction of the proposed Nuna (Columbia) and Rodinia
1416 supercontinents: *Precambrian Research*, vol. 160, pp. 159–178, doi:10.1016/j.precamres.2007.04.019.
- 1417 Ernst, R. E. and Youbi, N., 2017, How large igneous provinces affect global climate, sometimes cause mass
1418 extinctions, and represent natural markers in the geological record: *Palaeogeography, Palaeoclimatology,*
1419 *Palaeoecology*, vol. 478, pp. 30–52, doi:10.1016/j.palaeo.2017.03.014.
- 1420 Evans, D. A. D., 2006, Proterozoic low orbital obliquity and axial-dipolar geomagnetic field from evaporite
1421 palaeolatitudes: *Nature*, vol. 444, pp. 51–55, doi:10.1038/nature05203.
- 1422 Evans, D. A. D., Beukes, N. J., and Kirschvink, J. L., 1997, Low-latitude glaciation in the Palaeoproterozoic era:
1423 *Nature*, vol. 386, pp. 262–266, doi:10.1038/386262a0.
- 1424 Fairchild, I. J., Einsel, G., and Song, T., 1997, Possible seismic origin of molar tooth structures in Neoproterozoic
1425 carbonate ramp deposits, north China: *Sedimentology*, vol. 44, pp. 611–636,
1426 doi:10.1046/j.1365-3091.1997.d01-40.x.
- 1427 Fantle, M. S. and Higgins, J., 2014, The effects of diagenesis and dolomitization on Ca and Mg isotopes in marine
1428 platform carbonates: Implications for the geochemical cycles of Ca and Mg: *Geochimica et Cosmochimica Acta*,
1429 vol. 142, pp. 458 – 481, doi:https://doi.org/10.1016/j.gca.2014.07.025.
- 1430 Fritz, H., Abdelsalam, M., Ali, K. A., Bingen, B., Collins, A. S., Fowler, A. R., Ghebreab, W., Hauzenberger, C. A.,
1431 Johnson, P. R., Kusky, T. M., Macey, P., Muhongo, S., Stern, R. J., and Viola, G., 2013, Orogen styles in the
1432 East African Orogen: A review of the Neoproterozoic to Cambrian tectonic evolution: *Journal of African Earth*
1433 *Sciences*, vol. 86, pp. 65–106, doi:10.1016/j.jafrearsci.2013.06.004.

- 1434 Gabet, E. J. and Mudd, S. M., 2009, A theoretical model coupling chemical weathering rates with denudation rates:
1435 *Geology*, vol. 37, pp. 151–154, doi:10.1130/G25270A.1.
- 1436 Garland, C. R., 1980, Geology of the Adigrat area: *In* Ministry of Mines Memoir No. 1, p. 51.
- 1437 Goddériss, Y., Donnadieu, Y., Carretier, S., Aretz, M., Dera, G., Macouin, M., and Regard, V., 2017a, Onset and
1438 ending of the late Palaeozoic ice age triggered by tectonically paced rock weathering: *Nature Geoscience*, vol. 10,
1439 pp. 382–386, doi:10.1038/ngeo2931.
- 1440 Goddériss, Y., Donnadieu, Y., Nédélec, A., Dupré, B., Dessert, C., Grard, A., Ramstein, G., and François, L. M.,
1441 2003, The Sturtian ‘snowball’ glaciation: fire and ice: *Earth and Planetary Science Letters*, vol. 211, pp. 1–12,
1442 doi:10.1016/S0012-821X(03)00197-3.
- 1443 Goddériss, Y., Hir, G. L., Macouin, M., Donnadieu, Y., Hubert-Théou, L., Dera, G., Aretz, M., Fluteau, F., Li,
1444 Z. X., and Halverson, G. P., 2017b, Paleogeographic forcing of the strontium isotopic cycle in the Neoproterozoic:
1445 *Gondwana Research*, vol. 42, pp. 151–162, doi:10.1016/j.gr.2016.09.013.
- 1446 Hailu, T., 1975, Geological map of Adi Arkay: Addis Ababa: Tech. rep., Geological Survey of Ethiopia.
- 1447 Halverson, G. P., 2006, A Neoproterozoic Chronology, Springer Netherlands, Dordrecht, pp. 231–271:
1448 doi:10.1007/1-4020-5202-28.
- 1449 Halverson, G. P., Dudás, F. Ö., Maloof, A. C., and Bowring, S. A., 2007a, Evolution of the $^{87}\text{Sr}/^{86}\text{Sr}$ composition of
1450 Neoproterozoic seawater: *Palaeogeography, Palaeoclimatology, Palaeoecology*, vol. 256, pp. 103–129,
1451 doi:10.1016/j.palaeo.2007.02.028.
- 1452 Halverson, G. P., Hoffman, P. F., Schrag, D. P., Maloof, A. C., and Rice, A. H. N., 2005, Toward a Neoproterozoic
1453 composite carbon-isotope record: *GSA Bulletin*, vol. 117, pp. 1181–1207, doi:10.1130/B25630.1.
- 1454 Halverson, G. P., Maloof, A. C., Schrag, D. P., Dudás, F. Ö., and Hurtgen, M., 2007b, Stratigraphy and
1455 geochemistry of a ca 800 Ma negative carbon isotope interval in northeastern Svalbard: *Chemical Geology*, vol.
1456 237, pp. 5–27, doi:10.1016/j.chemgeo.2006.06.013.
- 1457 Hartmann, J., Moosdorf, N., Lauerwald, R., Hinderer, M., and West, A. J., 2014, Global chemical weathering and
1458 associated P-release - the role of lithology, temperature and soil properties: *Chemical Geology*, vol. 363, pp.
1459 145–163, doi:10.1016/j.chemgeo.2013.10.025.
- 1460 Heaman, L. M., LeCheminant, A. N., and Rainbird, R. H., 1992, Nature and timing of Franklin igneous events,
1461 Canada: implications for a Late Proterozoic mantle plume and the break-up of Laurentia: *Earth and Planetary
1462 Science Letters*, vol. 109, pp. 117–131, doi:10.1016/0012-821X(92)90078-A.
- 1463 Hodgskiss, M. S. W., Kunzmann, M., Poirier, A., and Halverson, G. P., 2018, The role of microbial iron reduction
1464 in the formation of Proterozoic molar tooth structures: *Earth and Planetary Science Letters*, vol. 482, pp. 1–11,
1465 doi:10.1016/j.epsl.2017.10.037.
- 1466 Hoffman, P. F., Halverson, G. P., Domack, E. W., Maloof, A. C., Swanson-Hysell, N. L., and Cox, G. M., 2012,
1467 Cryogenian glaciations on the southern tropical paleomargin of Laurentia (NE Svalbard and East Greenland),
1468 and a primary origin for the upper Russoya (Islay) carbon isotope excursion: *Precambrian Research*, vol.
1469 206–207, pp. 137–158, doi:10.1016/j.precamres.2012.02.018.
- 1470 Hoffman, P. F., Kaufman, A. J., Halverson, G. P., and Schrag, D. P., 1998, A Neoproterozoic Snowball Earth:
1471 *Science*, vol. 281, pp. 1342–1346, doi:10.1126/science.281.5381.1342.
- 1472 Hoffman, P. F. and Li, Z.-X., 2009, A palaeogeographic context for Neoproterozoic glaciation: *Palaeogeography,
1473 Palaeoclimatology, Palaeoecology*, vol. 277, pp. 158–172, doi:10.1016/j.palaeo.2009.03.013.

- 1474 Hoffman, P. F., Macdonald, F. A., and Halverson, G. P., 2011, Chemical sediments associated with Neoproterozoic
1475 glaciation: iron formation, cap carbonate, barite and phosphorite: In Arnaud, E., Halverson, G. P., and
1476 Shields-Zhou, G. A., eds., The Geological Record of Neoproterozoic Glaciations, Geological Society of London,
1477 vol. 36, chap. 5, pp. 67–80, doi:10.1144/M36.5.
- 1478 Hoffman, P. F. and Schrag, D. P., 2002, The snowball Earth hypothesis: testing the limits of global change: Terra
1479 Nova, vol. 14, pp. 129–155, doi:10.1046/j.1365-3121.2002.00408.x.
- 1480 Husson, J. M., Maloof, A. C., and Schoene, B., 2012, A syn-depositional age for Earth's deepest $\delta^{13}\text{C}$ excursion
1481 required by isotope conglomerate tests: Terra Nova, vol. 24, pp. 318–325, doi:10.1111/j.1365-3121.2012.01067.x.
- 1482 Husson, J. M., Maloof, A. C., Schoene, B., Chen, C. Y., and Higgins, J. A., 2015, Stratigraphic expression of
1483 Earth's deepest $\delta^{13}\text{C}$ excursion in the Wonoka Formation of South Australia: American Journal of Science, vol.
1484 315, pp. 1–45, doi:10.2475/01.2015.01.
- 1485 Jacobsen, S. B. and Kaufman, A. J., 1999, The Sr, C and O isotopic evolution of Neoproterozoic seawater:
1486 Chemical Geology, vol. 161, pp. 37–57, doi:10.1016/S0009-2541(99)00080-7.
- 1487 Jagoutz, O., Macdonald, F. A., and Royden, L., 2016, Low-latitude arc-continent collision as a driver for global
1488 cooling: Proceedings of the National Academy of Sciences, vol. 113, pp. 4935–4940, doi:10.1073/pnas.1523667113.
- 1489 Johnson, P. R., 2014, An expanding Arabian-Nubian Shield geochronologic and isotopic dataset: defining limits and
1490 confirming the tectonic setting of a Neoproterozoic accretionary orogen: The Open Geology Journal, vol. 8, pp.
1491 3–33, doi:10.2174/1874262901408010003.
- 1492 Johnson, P. R., Abdelsalam, M. G., and Stern, R. J., 2003, The Bi'r Umq-Nakasib Suture Zone in the
1493 Arabian-Nubian Shield: a key to understanding crustal growth in the East African Orogen: Gondwana Research,
1494 vol. 6, pp. 523–530, doi:10.1016/S1342-937X(05)71003-0.
- 1495 Johnson, P. R., Andresen, A., Collins, A. S., Fowler, A. R., Fritz, H., Ghebreab, W., Kusky, T., and Stern, R. J.,
1496 2011, Late Cryogenian-Ediacaran history of the Arabian-Nubian Shield: A review of depositional, plutonic,
1497 structural, and tectonic events in the closing stages of the northern East African Orogen: Journal of African
1498 Earth Sciences, vol. 61, pp. 167–232, doi:10.1016/j.jafrearsci.2011.07.003.
- 1499 Johnson, P. R. and Woldehaimanot, B., 2003, Development of the Arabian-Nubian Shield: perspectives on accretion
1500 and deformation in the northern East African Orogen and the assembly of Gondwana: Geological Society,
1501 London, Special Publications, vol. 206, pp. 289–325, doi:10.1144/GSL.SP.2003.206.01.15.
- 1502 Jones, D. S., Maloof, A. C., Hurtgen, M. T., Rainbird, R. H., and Schrag, D. P., 2010, Regional and global
1503 chemostratigraphic correlation of the early Neoproterozoic Shaler Supergroup, Victoria Island, Northwestern
1504 Canada: Precambrian Research, vol. 181, pp. 43–63, doi:10.1016/j.precamres.2010.05.012.
- 1505 Kastens, K., Mascle, J., Auroux, C., Bonatti, E., Broglia, C., Channell, J., Curzi, P., Emeis, K.-C., Glaçon, G.,
1506 Hasegawa, S., Hieke, W., Mascle, G., McCoy, F., McKenzie, J., Mendelson, J., Müller, C., Réhault, J.-P.,
1507 Robertson, A., Sartori, R., Sprovieri, R., and Torii, M., 1988, ODP Leg 107 in the Tyrrhenian Sea: insights into
1508 passive margin and back-arc basin evolution: Geological Society of America Bulletin, vol. 100, pp. 1140–1156,
1509 doi:10.1130/0016-7606(1988)100<1140:OLITTS>2.3.CO;2.
- 1510 Kaufman, A. J., Knoll, A. H., and Narbonne, G. M., 1997, Isotopes, ice ages, and terminal Proterozoic earth
1511 history: Proceedings of the National Academy of Sciences, vol. 94, pp. 6600–6605, doi:10.1073/pnas.94.13.6600.
- 1512 Kennedy, M. J., Runnegar, B., Prave, A. R., Hoffmann, K.-H., and Arthur, M. A., 1998, Two or four Neoproterozoic
1513 glaciations?: Geology, vol. 26, pp. 1059–1063, doi:10.1130/0091-7613(1998)026<1059:TOFNG>2.3.CO;2.
- 1514 Knoll, A. H., Javaux, E. J., Hewitt, D., and Cohen, P., 2006, Eukaryotic organisms in Proterozoic oceans:
1515 Philosophical Transactions of the Royal Society of London B: Biological Sciences, vol. 361, pp. 1023–1038,
1516 doi:10.1098/rstb.2006.1843.

- 1517 Kozdrój, W., Kennedy, A. K., Johnson, P. R., Ziolkowska-Kozdrój, M., and Kadi, K., 2017, Geochronology in the
1518 southern Midyan terrane: a review of constraints on the timing of magmatic pulses and tectonic evolution in a
1519 northwestern part of the Arabian Shield: *International Geology Review*, vol. 60, pp. 1290–1319,
1520 doi:10.1080/00206814.2017.1385425.
- 1521 Küster, D., Liégeois, J.-P., Matukov, D., Sergeev, S., and Lucassen, F., 2008, Zircon geochronology and Sr, Nd, Pb
1522 isotope geochemistry of granitoids from Bayuda Desert and Sabaloka (Sudan): evidence for a Bayudian event
1523 (920–900 Ma) preceding the Pan-African orogenic cycle (860–590 Ma) at the eastern boundary of the Saharan
1524 Metacraton: *Precambrian Research*, vol. 164, pp. 16–39, doi:10.1016/j.precamres.2008.03.003.
- 1525 Kuznetsov, A. B., Semikhatov, M. A., Maslov, A. V., Gorokhov, I. M., Prasolov, E. M., Krupenin, M. T., and
1526 Kislova, I. V., 2006, New data on Sr-and C-isotopic chemostratigraphy of the Upper Riphean type section
1527 (Southern Urals): *Stratigraphy and Geological Correlation*, vol. 14, pp. 602–628, doi:10.1134/S0869593806060025.
- 1528 Lan, Z., Li, X., Zhu, M., Chen, Z.-Q., Zhang, Q., Li, Q., Lu, D., Liu, Y., and Tang, G., 2014, A rapid and
1529 synchronous initiation of the wide spread Cryogenian glaciations: *Precambrian Research*, vol. 255, pp. 401–411.
- 1530 Li, Z. X., Bogdanova, S. V., Collins, A. S., Davidson, A., Waele, B. D., Ernst, R. E., Fitzsimons, I. C. W., Fuck,
1531 R. A., Gladkochub, D. P., Jacobs, J., Karlstrom, K. E., Lu, S., Natapov, L. M., Pease, V., Pisarevsky, S. A.,
1532 Thrane, K., and Vernikovsky, V., 2008, Assembly, configuration, and break-up history of Rodinia: a synthesis:
1533 *Precambrian Research*, vol. 160, pp. 179–210, doi:10.1016/j.precamres.2007.04.021.
- 1534 Li, Z.-X., Evans, D. A., and Halverson, G. P., 2013, Neoproterozoic glaciations in a revised global palaeogeography
1535 from the breakup of Rodinia to the assembly of Gondwanaland: *Sedimentary Geology*, vol. 294, pp. 219–232,
1536 doi:10.1016/j.sedgeo.2013.05.016.
- 1537 Li, Z. X., Evans, D. A. D., and Zhang, S., 2004, A 90° spin on Rodinia: possible causal links between the
1538 Neoproterozoic supercontinent, superplume, true polar wander and low-latitude glaciation: *Earth and Planetary
1539 Science Letters*, vol. 220, pp. 409–421, doi:10.1016/S0012-821X(04)00064-0.
- 1540 Macdonald, F. A., Schmitz, M. D., Crowley, J. L., Roots, C. F., Jones, D. S., Maloof, A. C., Strauss, J. V., Cohen,
1541 P. A., Johnston, D. T., and Schrag, D. P., 2010, Calibrating the Cryogenian: *Science*, vol. 327, pp. 1241–1243,
1542 doi:10.1126/science.1183325.
- 1543 Macdonald, F. A. and Wordsworth, R., 2017, Initiation of Snowball Earth with volcanic sulfur aerosol emissions:
1544 *Geophysical Research Letters*, vol. 44, pp. 1938–1946, doi:10.1002/2016GL072335.
- 1545 MacLennan, S. A., Park, Y., Swanson-Hysell, N. L., Maloof, A. C., Schoene, B., Gebreslassie, M., Antilla, E.,
1546 Tesema, T., Alene, M., and Haileab, B., 2018, The arc of the Snowball: U-Pb dates constrain the Islay anomaly
1547 and the initiation of the Sturtian glaciation: *Geology*, vol. 46, pp. 539–542, doi:10.1130/G40171.1.
- 1548 Maloof, A. C., Halverson, G. P., Kirschvink, J. L., Schrag, D. P., Weiss, B. P., and Hoffman, P. F., 2006, Combined
1549 paleomagnetic, isotopic, and stratigraphic evidence for true polar wander from the Neoproterozoic
1550 Akademikerbreen Group, Svalbard, Norway: *GSA Bulletin*, vol. 118, pp. 1099–1124, doi:10.1130/B25892.1.
- 1551 Maloof, A. C., Porter, S. M., Moore, J. L., Dudás, F. Ö., Bowring, S. A., Higgins, J. A., Fike, D. A., and Eddy,
1552 M. P., 2010, The earliest Cambrian record of animals and ocean geochemical change: *Geological Society of
1553 America Bulletin*, vol. 122, pp. 1731–1774, doi:10.1130/B30346.1.
- 1554 McArthur, J. M., Rio, D., Massari, F., Castradori, D., Bailey, T. R., Thirlwall, M., and Houghton, S., 2006, A
1555 revised Pliocene record for marine $^{87}\text{Sr}/^{86}\text{Sr}$ used to date an interglacial event recorded in the Cockburn Island
1556 Formation, Antarctic Peninsula: *Palaeogeography, Palaeoclimatology, Palaeoecology*, vol. 242, pp. 126–136,
1557 doi:10.1016/j.palaeo.2006.06.004.
- 1558 McCormick, M. P., Thomason, L. W., and Trepte, C. R., 1995, Atmospheric effects of the Mt Pinatubo eruption:
1559 *Nature*, vol. 373, pp. 399–404, doi:10.1038/373399a0.

- 1560 McLean, N. M., Condon, D. J., Schoene, B., and Bowring, S. A., 2015, Evaluating uncertainties in the calibration of
1561 isotopic reference materials and multi-element isotopic tracers (EARTHTIME tracer calibration part II):
1562 *Geochimica et Cosmochimica Acta*, vol. 164, pp. 481–501, doi:10.1016/j.gca.2015.02.040.
- 1563 McLelland, J. M., Selleck, B. W., and Bickford, M. E., 2013, Tectonic evolution of the Adirondack mountains and
1564 Grenville orogen inliers within the USA: *Geoscience Canada*, vol. 40, pp. 318–352,
1565 doi:10.12789/geocanj.2013.40.022.
- 1566 Meert, J. G., Pandit, M. K., and Kamenov, G. D., 2013, Further geochronological and paleomagnetic constraints on
1567 Malani (and pre-Malani) magmatism in NW India: *Tectonophysics*, vol. 608, pp. 1254–1267,
1568 doi:10.1016/j.tecto.2013.06.019.
- 1569 Miller, N. R., Alene, M., Sacchi, R., Stern, R. J., Conti, A., Kröner, A., and Zuppi, G., 2003, Significance of the
1570 Tambien Group (Tigray, N. Ethiopia) for Snowball Earth events in the Arabian-Nubian Shield: *Precambrian*
1571 *Research*, vol. 121, pp. 263–283, doi:10.1016/S0301-9268(03)00014-7.
- 1572 Miller, N. R., Stern, R. J., Avigad, D., Beyth, M., and Schilman, B., 2009, Cryogenian slate-carbonate sequences of
1573 the Tambien Group, Northern Ethiopia (I): Pre-“Sturtian” chemostratigraphy and regional correlations:
1574 *Precambrian Research*, vol. 170, pp. 129–156, doi:10.1016/j.precamres.2008.12.004.
- 1575 Müller, R. D., Sdrolias, M., Gaina, C., and Roest, W. R., 2008, Age, spreading rates, and spreading asymmetry of
1576 the world’s ocean crust: *Geochemistry, Geophysics, Geosystems*, vol. 9, pp. 1–19, doi:10.1029/2007GC001743.
- 1577 Niu, J., Li, Z.-X., and Zhu, W., 2016, Palaeomagnetism and geochronology of mid-Neoproterozoic Yanbian dykes,
1578 South China: implications for a c. 820–800 Ma true polar wander event and the reconstruction of Rodinia:
1579 *Geological Society, London, Special Publications*, vol. 424, pp. 191–211, doi:10.1144/SP424.11.
- 1580 Norton, K. P., Molnar, P., and Schlunegger, F., 2014, The role of climate-driven chemical weathering on soil
1581 production: *Geomorphology*, vol. 204, pp. 510–517, doi:10.1016/j.geomorph.2013.08.030.
- 1582 Ojakangas, R. W., Morey, G. B., and Green, J. C., 2001, The Mesoproterozoic Midcontinent Rift System, Lake
1583 Superior Region, USA: *Sedimentary Geology*, vol. 141–142, pp. 421–442, doi:10.1016/S0037-0738(01)00085-9.
- 1584 Pallister, J. S., Stacey, J. S., Fischer, L. B., and Premo, W. R., 1988, Precambrian ophiolites of Arabia: geologic
1585 settings, U-Pb geochronology, Pb-isotope characteristics, and implications for continental accretion: *Precambrian*
1586 *Research*, vol. 38, pp. 1–54, doi:10.1016/0301-9268(88)90092-7.
- 1587 Palmer, H. C., Merz, B. A., and Hayatsu, A., 1977, The Sudbury dikes of the Grenville Front region:
1588 paleomagnetism, petrochemistry, and K-Ar age studies: *Canadian Journal of Earth Sciences*, vol. 14, pp.
1589 1867–1887, doi:10.1139/e77-158.
- 1590 Pepresson, S. J. and Buchan, K. L., 1999, Borden dykes of Baffin Island, Northwest Territories: a Franklin U-Pb
1591 baddeleyite age and a paleomagnetic reinterpretation: *Canadian Journal of Earth Sciences*, vol. 36, pp. 65–73,
1592 doi:10.1139/e98-091.
- 1593 Peng, S., Kusky, T. M., Jiang, X. F., Wang, L., Wang, J. P., and Deng, H., 2012, Geology, geochemistry, and
1594 geochronology of the Miaowan ophiolite, Yangtze craton: Implications for South China’s amalgamation history
1595 with the Rodinian supercontinent: *Gondwana Research*, vol. 21, pp. 577–594, doi:10.1016/j.gr.2011.07.010,
1596 special Issue: Western Gondwana.
- 1597 Pollard, D. and Kasting, J. F., 2005, Snowball Earth: A thin-ice solution with flowing sea glaciers: *Journal of*
1598 *Geophysical Research: Oceans*, vol. 110, pp. 1–16, doi:10.1029/2004JC002525.
- 1599 Pollock, M. D., Kah, L. C., and Bartley, J. K., 2006, Morphology of molar-tooth structures in Precambrian
1600 carbonates: influence of substrate rheology and implications for genesis: *Journal of Sedimentary Research*,
1601 vol. 76, pp. 310–323, doi:10.2110/jsr.2006.021.

- 1602 Pratt, B. R., 1998, Molar-tooth structure in Proterozoic carbonate rocks: origin from synsedimentary earthquakes,
1603 and implications for the nature and evolution of basins and marine sediment: Geological Society of America
1604 Bulletin, vol. 110, pp. 1028–1045, doi:10.1130/0016-7606(1998)110<1028:MTSIPC>2.3.CO;2.
- 1605 Richter, F. M., Rowley, D. B., and DePaolo, D. J., 1992, Sr isotope evolution of seawater: the role of tectonics:
1606 Earth and Planetary Science Letters, vol. 109, pp. 11–23, doi:10.1016/0012-821X(92)90070-C.
- 1607 Rooney, A. D., Macdonald, F. A., Strauss, J. V., Dudás, F. Ö., Hallmann, C., and Selby, D., 2014, Re-Os
1608 geochronology and coupled Os-Sr isotope constraints on the Sturtian snowball Earth: Proceedings of the
1609 National Academy of Sciences, vol. 111, pp. 51–56, doi:10.1073/pnas.1317266110.
- 1610 Rose, C. V., Swanson-Hysell, N. L., Husson, J. M., Poppick, L. N., Cottle, J. M., Schoene, B., and Maloof, A. C.,
1611 2012, Constraints on the origin and relative timing of the Trezona $\delta^{13}\text{C}$ anomaly below the end-Cryogenian
1612 glaciation: Earth and Planetary Science Letters, vol. 319–320, pp. 241–250, doi:10.1016/j.epsl.2011.12.027.
- 1613 Rothman, D. H., Hayes, J. M., and Summons, R. E., 2003, Dynamics of the Neoproterozoic carbon cycle:
1614 Proceedings of the National Academy of Sciences, vol. 100, pp. 8124–8129, doi:10.1073/pnas.0832439100.
- 1615 Sawaki, Y., Kawai, T., Shibuya, T., Tahata, M., Omori, S., Komiya, T., Yoshida, N., Hirata, T., Ohno, T.,
1616 Windley, B. F., and Maruyama, S., 2010, $^{87}\text{Sr}/^{86}\text{Sr}$ chemostratigraphy of Neoproterozoic Dalradian carbonates
1617 below the Port Askaig Glaciogenic Formation, Scotland: Precambrian Research, vol. 179, pp. 150–164,
1618 doi:10.1016/j.precamres.2010.02.021.
- 1619 Schellart, W. P., Lister, G. S., and Toy, V. G., 2006, A Late Cretaceous and Cenozoic reconstruction of the
1620 Southwest Pacific region: tectonics controlled by subduction and slab rollback processes: Earth-Science Reviews,
1621 vol. 76, pp. 191–233, doi:10.1016/j.earscirev.2006.01.002.
- 1622 Schrag, D. P., Higgins, J. A., Macdonald, F. A., and Johnston, D. T., 2013, Authigenic carbonate and the history of
1623 the global carbon cycle: Science, vol. 339, pp. 540–543, doi:10.1126/science.1229578.
- 1624 Smith, A. G., 1968, The origin and deformation of some ‘molar-tooth’ structures in the Precambrian Belt-Purcell
1625 Supergroup: The Journal of Geology, vol. 76, pp. 426–443.
- 1626 Spear, N., Holland, H. D., Garcia-Veigas, J., Lowenstein, T. K., Giegengack, R., and Peters, H., 2014, Analyses of
1627 fluid inclusions in Neoproterozoic marine halite provide oldest measurement of seawater chemistry: Geology,
1628 vol. 42, pp. 103–106, doi:10.1130/G34913.1.
- 1629 Stern, R. J., 1994, Arc-assembly and continental collision in the Neoproterozoic African Orogen: implications for
1630 the consolidation of Gondwanaland: Annual Review of Earth and Planetary Sciences, vol. 22, pp. 319–351,
1631 doi:10.1146/annurev.ea.22.050194.001535.
- 1632 Strauss, J. V., Rooney, A. D., Macdonald, F. A., Brandon, A. D., and Knoll, A. H., 2014, 740 Ma vase-shaped
1633 microfossils from Yukon, Canada: implications for Neoproterozoic chronology and biostratigraphy: Geology,
1634 vol. 42, pp. 659–662, doi:10.1130/G35736.1.
- 1635 Swanson-Hysell, N. L. and Macdonald, F. A., 2017, Tropical weathering of the Taconic orogeny as a driver for
1636 Ordovician cooling: Geology, vol. 45, pp. 719–722, doi:10.1130/G38985.1.
- 1637 Swanson-Hysell, N. L., Maloof, A. C., Condon, D. J., Jenkin, G. R., Alene, M., Tremblay, M. M., Tesema, T.,
1638 Rooney, A. D., and Haileab, B., 2015, Stratigraphy and geochronology of the Tambien Group, Ethiopia: evidence
1639 for globally synchronous carbon isotope change in the Neoproterozoic: Geology, vol. 43, pp. 323–326,
1640 doi:10.1130/G36347.1.
- 1641 Swanson-Hysell, N. L., Maloof, A. C., Kirschvink, J. L., Evans, D. A. D., Halverson, G. P., and Hurtgen, M. T.,
1642 2012, Constraints on Neoproterozoic paleogeography and Paleozoic orogenesis from paleomagnetic records of the
1643 Bitter Springs Formation, Amadeus Basin, central Australia: American Journal of Science, vol. 312, pp. 817–884,
1644 doi:10.2475/08.2012.01.

- 1645 Swanson-Hysell, N. L., Ramezani, J., Fairchild, L. M., and Rose, I., 2018, Failed rifting and fast drifting:
1646 Midcontinent Rift development, Laurentia's rapid motion and the driver of Grenvillian orogenesis: Geological
1647 Society of America Bulletin, doi:10.1130/B31944.1, in press.
- 1648 Swanson-Hysell, N. L., Rose, C. V., Calmet, C. C., Halverson, G. P., Hurtgen, M. T., and Maloof, A. C., 2010,
1649 Cryogenian glaciation and the onset of carbon-isotope decoupling: *Science*, vol. 328, pp. 608–611,
1650 doi:10.1126/science.1184508.
- 1651 Swart, P. K., 2008, Global synchronous changes in the carbon isotopic composition of carbonate sediments
1652 unrelated to changes in the global carbon cycle: *Proceedings of the National Academy of Sciences*, vol. 105, pp.
1653 13,741–13,745, doi:10.1073/pnas.0802841105.
- 1654 Swart, P. K. and Kennedy, M. J., 2012, Does the global stratigraphic reproducibility of $\delta^{13}\text{C}$ in Neoproterozoic
1655 carbonates require a marine origin? A Pliocene-Pleistocene comparison: *Geology*, vol. 40, pp. 87–90,
1656 doi:10.1130/G32538.1.
- 1657 Tadesse, T., Hoshino, M., and Sawada, Y., 1999, Geochemistry of low-grade metavolcanic rocks from the
1658 Pan-African of the Axum area, northern Ethiopia: *Precambrian Research*, vol. 96, pp. 101–124,
1659 doi:10.1016/S0301-9268(99)00008-X.
- 1660 Teklay, M., 1997, Petrology, geochemistry and geochronology of Neoproterozoic magmatic arc rocks from Eritrea:
1661 implications for crustal evolution in the southern Nubian Shield: Department of Mines-Ministry of Energy Mines
1662 and Water Resources-State of Eritrea.
- 1663 Teklay, M., 2006, Neoproterozoic arc-back-arc system analog to modern arc-back-arc systems: evidence from
1664 tholeiite-boninite association, serpentinite mudflows and across-arc geochemical trends in Eritrea, southern
1665 Arabian-Nubian shield: *Precambrian Research*, vol. 145, pp. 81–92, doi:10.1016/j.precamres.2005.11.015.
- 1666 Teklay, M., Haile, T., Kröner, A., Asmerom, Y., and Watson, J., 2003, A back-arc palaeotectonic setting for the
1667 Augaro Neoproterozoic magmatic rocks of western Eritrea: *Gondwana Research*, vol. 6, pp. 629–640,
1668 doi:10.1016/S1342-937X(05)71012-1.
- 1669 Tziperman, E., Halevy, I., Johnston, D. T., Knoll, A. H., and Schrag, D. P., 2011, Biologically induced initiation of
1670 Neoproterozoic snowball-Earth events: *Proceedings of the National Academy of Sciences*, vol. 108, pp.
1671 15,091–15,096, doi:10.1073/pnas.1016361108.
- 1672 Uyeda, S. and Kanamori, H., 1979, Back-arc opening and the mode of subduction: *Journal of Geophysical
1673 Research: Solid Earth*, vol. 84, pp. 1049–1061, doi:10.1029/JB084iB03p01049.
- 1674 Veizer, J., 1989, Strontium isotopes in seawater through time: *Annual Review of Earth and Planetary Sciences*,
1675 vol. 17, p. 141, doi:10.1146/annurev.ea.17.050189.001041.
- 1676 Volpe, A. M. and Douglas Macdougall, J., 1990, Geochemistry and isotopic characteristics of mafic (Phulad
1677 Ophiolite) and related rocks in the Delhi Supergroup, Rajasthan, India: implications for rifting in the
1678 Proterozoic: *Precambrian Research*, vol. 48, pp. 167–191, doi:10.1016/0301-9268(90)90061-t.
- 1679 Vujovich, G. I. and Kay, S. M., 1998, A Laurentian? Grenville-age oceanic arc/back-arc terrane in the Sierra de Pie
1680 de Palo, Western Sierras Pampeanas, Argentina: *Geological Society, London, Special Publications*, vol. 142, pp.
1681 159–179, doi:10.1144/gsl.sp.1998.142.01.09.
- 1682 Vujovich, G. I., van Staal, C. R., and Davis, W., 2004, Age constraints on the tectonic evolution and provenance of
1683 the Pie de Palo Complex, Cuyania Composite Terrane, and the Famatinian Orogeny in the Sierra de Pie de
1684 Palo, San Juan, Argentina: *Gondwana Research*, vol. 7, pp. 1041–1056, doi:10.1016/s1342-937x(05)71083-2.
- 1685 White, R. S., 1997, Mantle temperature and lithospheric thinning beneath the Midcontinent rift system: evidence
1686 from magmatism and subsidence: *Canadian Journal of Earth Sciences*, vol. 34, pp. 464–475, doi:10.1139/e17-038.

- 1687 Woodcock, N. H., 2004, Life span and fate of basins: *Geology*, vol. 32, pp. 685–688, doi:10.1130/G20598.1.
- 1688 Zhao, G., 2015, Jiangnan Orogen in South China: Developing from divergent double subduction: *Gondwana
1689 Research*, vol. 27, pp. 1173–1180, doi:10.1016/j.gr.2014.09.004.
- 1690 Zhisheng, A., Kutzbach, J. E., Prell, W. L., and Porter, S. C., 2001, Evolution of Asian monsoons and phased uplift
1691 of the Himalaya–Tibetan plateau since Late Miocene times: *Nature*, vol. 411, pp. 62–66, doi:10.1038/35075035.